ABSTRACT

Title of dissertation: HIGH-FORCE ELECTROSTATIC INCHWORM MOTORS FOR MILLIROBOTICS APPLICATIONS

Ivan Penskiy
Doctor of Philosophy, 2019

Dissertation directed by: Associate Professor Sarah Bergbreiter
Department of Mechanical Engineering

Due to scaling laws and ease of fabrication, electrostatic actuation offers a promising opportunity for actuation in small-scale robotics. This dissertation presents several novel actuator and motor designs as well as new techniques by which to characterize electrostatic gap closing actuators.

A new motor architecture that uses in-plane electrostatic gap-closing actuators along with a flexible driving arm mechanism to improve motor force density is introduced, optimized, manufactured, and tested. This motor operates similarly to other inchworm-based microactuators by accumulating small displacements from the actuators into much larger displacements in the motor. Using an analytical model of the inchworm motor based on the static force equilibrium condition, optimizations of a full motor design were performed to maximize motor force density. In addition, force losses from supporting flexures were included to calculate the theoretical motor efficiency for different motor designs. This force density optimization analysis of the gap-closing actuators and supporting motor structures

provided the basis for designing and manufacturing inchworm motors with flexible driving arms and gap-closing actuators. The motor required only a single-mask fabrication and demonstrated robust performance, a maximum speed of 4.8 mm/s , and a maximum force on the shuttle of 1.88 mN at 110 V which corresponds to area force density of 1.38 mN/mm^2. In addition, instead of estimating motor force based on drawn or measured dimensions which often overestimates force, the demonstrated maximum motor force was measured using calibrated springs. The efficiency of the manufactured motor was measured at 8.75% using capacitance measurements and useful work output.

To further increase force output from these motors, several new designs were proposed, analyzed, and tested. Thick film actuators that take advantage of a through-wafer etch offered a promising opportunity to increase force given the linear increase in force with actuator thickness. However, fabrication challenges made this particular approach inoperable with current manufacturing capabilities. New actuator designs with compliant and zipping electrodes did demonstrate significant increases in force, but not the order of magnitude increase promised by modeling and analysis. In order to study and understand this discrepancy, several new techniques were developed to electrically and electromechanically characterize the force output of these new actuator designs. The first technique identifies parameters in an equivalent circuit model of the actuator, including actuator capacitance. By monitoring change in capacitance along the travel range of the motor, electrostatic force in equilibrium can be estimated. Charge transferred to and from the actuator can also provide an estimate of actuator efficiency. The second technique uses a constant rate spike to more thoroughly

explore the rapid dynamics of actuator pull-in and zipping.

New characterization methods allowed for collecting large amounts of data describing performance of motors with zipping and compliant electrodes. The data was used to back up the main hypothesis of force output discrepancy between theory and practice. Also, it was used to highlight extreme sensitivity of proposed motors toward manufacturing process and its tolerances.

HIGH-FORCE ELECTROSTATIC INCHWORM MOTORS FOR MILLIROBOTICS APPLICATIONS

by

Ivan Penskiy

Dissertation submitted to the Faculty of the Graduate School of the
University of Maryland, College Park in partial fulfillment
of the requirements for the degree of
Doctor of Philosophy
2019

Advisory Committee:
Associate Professor Sarah Bergbreiter, Chair/Advisor
Professor Amr Baz
Professor Don DeVoe
Professor Reza Ghodssi
Professor Miao Yu

Table of Contents

List of Tables

List of Figures

Chapter 1

Introduction

1.1 Motivation and Applications

Isaac Asimov defined his Three Laws of Robotics in the beginning of 1940s. Since then, rapid development of technologies and sciences brought robots from the pages of his books into real life. It should be noted that in the context of this work the term "robot" is defined in the most general sense, as a mechanical structure that can be actuated to perform a certain task. A robot can be as simple as a spring-mass system actuated using external electromagnetic field or as complicated as a large industrial robot.

Robots developed in the second part of the 20th century were mostly electromechanical systems with actuators driving multiple degrees of freedom (DOFs) and very complicated mechanisms. Typical examples of these are industrial robots and modern humanoid robots such as ASIMO [2] or Robonaut [3].

In more recent years the exponential growth of the mobile personal devices market has driven the development and miniaturization of batteries and electronics components in addition to lowering their prices. This, in turn, has given a big incentive towards scaling down robots, and as a result remote control toys, quadcopters, and even home appliance robots are abundant and inexpensive nowadays.

As part of this trend of scaling devices down, development of microelectronic fabrication technologies gave birth to microelectromechanical systems (MEMS) in the 1980s. The largest commercial success from the MEMS technologies was in the sensor industry due to possibility of improving performance and miniaturizing a large variety of sensors. On the other hand, despite a lot of effort and research, MEMS actuators and mechanisms utilizing them are mostly limited to academia and have not found the same commercial success. It is important to note that small robots need both small sensors and small actuators.

All robots can be grouped into three sets based on their overall scale and the smallest feature size: large/meter scale robots that use the standard manufacturing and assembly, mesoscale robots that use high accuracy molding and other manufacturing methods that reduce assembly, and microscale robots that are made using MEMS fabrication with minimal or no assembly. Among these three groups there is a set of millirobots at the juncture between mesoscale and microscale robots which is nearly unpopulated. The reasons for that are mostly technological – the actuators used in mesoscale robots are too big and can not be scaled down further, and the MEMS actuators are not powerful enough to drive milliscale mechanisms.

Another big issue is the complicated integration of components since the manufacturing processes that are capable of building robots at this scale in one assembly free step are not mature yet. In the rest of this manuscript millirobots are defined with total length scales on the order of 1 mm to a couple centimeters but with some of their features of only several micrometers necessitating microfabrication.

The size of millirobots fits perfectly in the paradigm of network robotics where a large number of small and inexpensive robots are scattered around the area to perform various tasks such as search and rescue, establishing a sensor network, reconnaissance. Such robots can walk, hop, jump, or fly. This idea has been analyzed and attempted before with various levels of success [4–6]. Milliscale actuators can be also used in areas other than robotics since there are no alternative widely available, inexpensive, and robust actuators at this scale. For example in medicine for controlled needle insertion [7], actuated prosthesis [8], needle-free drug delivery [9], microsurgical tools [10, 11] and in optics for optical microswitches [12, 13].

1.2 Goals

The main components/challenges of an autonomous milliscale robot are mechanisms, integration, actuation, control, and power [14]. This work will focus on four of these components: mechanisms, actuation, their integration, and control.

The primary focus of the dissertation is on the design and manufacture of a MEMS actuator that satisfies the following requirements:

- provide high force output to drive mechanisms larger than the actuator. The power output is also important but in this work the main emphasis will be done on maximizing the force;
- provide high power efficiency to maximize the time available for autonomous work. In the scope of this work all tests will be done with an external power supply but the possibilities of autonomous operation with an on-board power supply will be discussed;

- provide mechanical robustness to ensure successful assembly with larger mechanisms and minimize the chance of failure during testing and operation;
- allow for easy integration with external mechanisms.

Provided success of the proposed actuator, the final portion of the dissertation will focus on the design and manufacture of an example millirobotic mechanism.

1.3 Related Work

This section covers previous work done in the millirobotics field and not just in actuation. Several reviews of actuators for small-scale robotics are available (e.g., [15, 16]). The efforts of making milliscale robots started in MEMS when the manufacturing technologies became mature enough to fabricate out-of-plane structures. The first successful attempt of making a walking millirobot was done by Ebefors [17]. He used polyimide to make flexible joints and actuated them by electrothermal heating. The robot could carry 30 times its own weight but required an external power supply and consumed 1.1 W. Due to such high power consumption, this take on millirobots did not receive any further development. Clearly more efficient actuators were needed.

Yeh used thin polysilicon sheets to fold into legs and mechanical couplings [18]. To minimize the power requirements he chose electrostatic gap-closing actuators to drive the robot. Despite successful demonstration of the majority of the robot's components separately, the full assembly was never shown. Hollar [19] used the same actuators as Yeh, but instead of folding the legs to make an out-of-plane structure, he added hinges to create pin joints and

achieve out-of-plane motion. The manufactured robot was assembled with solar cells and the basic digital logic to demonstrate completely autonomous motion. Despite successful tests, the manufacturing process was too complicated and unpredictable for reliable fabrication.

Bergbreiter [5] further improved architecture of electrostatic actuators to achieve higher force densities. She manually assembled soft elastomer with the fabricated actuator to successfully demonstrate mechanical energy storage in a strained micro rubber band and snap release. Similarly to Yeh, Bergbreiter showed all components of a jumping microrobot separately but the final assembly was never performed.

Electrostatic actuators designed based on those described in Chapter 2 of this work [20] have more recently been demonstrated in several further millirobotic demonstrations. Greenspun incorporated these electrostatic inchworm motors with a separate lever arm to increase force [21]. Steps were then accumulated to demonstrate short jumps. Contreras used the same inchworm motor design from [20] for a walking microrobot [22]. This robot was able to take some early steps.

Gerratt continued Bergbreiter's jumping work and in [23] introduced a new microfabrication process that enabled for embedding soft elastomers in-plane with silicon features in one fabrication step. He used that process to built an actuated mechanism capable of storing up to 0.45 µJ of potential energy in strained elastomer springs and quickly releasing it to kick small projectiles. The mechanism utilized electrothermal chevrons for actuators and was robust enough for repeatable strain-release cycle. Similarly to Eberfors' walking millirobot, however, the actuated jumping mechanism drew up to 10 W during operation,

which is unrealistic for autonomous applications.

A group of researchers at the Army Research Lab in Adelphi demonstrated some very impressive work with thin film piezoelectric actuators [24]. Their capabilities include integrating lateral piezoelectric actuators with high aspect ratio silicon flexures and fabricating bending PZT actuators with bio-inspired wings in one manufacturing process. Despite successful tests, the utilized fabrication process is very complicated and hard to replicate in the other fab facilities. Also, even though the researchers' goal was to enable millirobotics, they have not yet addressed the problem of a robot's robustness on that scale.

There are numerous other works that mainly focus on developing MEMS actuators for millirobot applications or can be used for that purpose: dielectric elastomer actuators [25], magnetic actuators [26], ionic polymer actuators [27], and more including their combinations. However, all of these works have yet various issues to resolve and they still have to demonstrate implementation of the actuators in milliscale mechanisms.

An alternative approach to manufacturing actuated mechanisms was introduced in the Berkeley Biomimetic Millisystems Lab [28]. The Smart Composite Microstructures (SCM) process combines laser machining and laminating of rigid (carbon fiber composite), flexible (polymer), and active (piezoelectric) layers to construct complex structures with integrated actuators. SCM was further progressed into pop-up book MEMS that expanded the library of available materials and allowed for pop-up self assembly [29]. This process can realize features as small as 65 µm and was used to make multiple robots at the milliscale [30, 31]. Bulk (versusu thin film) piezoelectric actuators used in these fabrication processes reach

maximum power output at resonance [32] which is not always desirable, and robots fabricated in this process are typically several centimeters in size or larger.

1.4 Organization of this Dissertation

This dissertation begins with a discussion of the optimization process, fabrication, and testing of an electrostatic inchworm motor fabricated in an SOI wafer. The next several chapters are focused on increasing and characterizing the force output of this actuator design. Chapter 3 describes efforts to make these motors using a through-wafer process. Chapter 4 describes novel characterization techniques to better understand why output force from these electrostatic motors was not matching theoretical predictions. Chapter 5 describes some modifications to the actuator design in Chapter 2 through the addition of compliant and sloped electrodes. The characterization techniques from Chapter 4 are used along with more traditional electromechanical testing to characterize the force output from these actuators. To capture the fast dynamics of pull-in and contact in these actuators, a new electrical characterization technique is proposed and tested in Chapter 6. The final chapter presents some conclusions, analysis of discrepancies between theoretical and measured results, and directions for future work.

Chapter 2

Optimization Process of Electrostatic Inchworm motor

This chapter was expanded from the following journal article: I.Penskiy, and S.Bergbreiter. "Optimized electrostatic inchworm motors using a flexible driving arm," Journal of Micromechanics and Microengineering, 23(1):015018, January 2013.

This chapter outlines the architecture of the electrostatic inchworm motor with flexible arms and describes the optimization process used to maximize its force density.

2.1 Types of Actuation

The main actuation methods at the small scale are piezoelectric, electromagnetic, electrostatic, electrothermal, shape memory alloy (SMA), and electroactive polymer. Several papers have evaluated the maximum performance of ideal microscale actuators [16,33]. Karpelson in [15] analyzed and chose piezoelectric as the best fit actuator for a cantimeter-scale flapping-wing microrobot. Some of the actuator types have issues that make them a poor choice for millirobotic applications. For instance, electrothermal and SMA actuators require being heated for operation which makes them energy inefficient and this is a problem for autonomous applications. Research on electroactive polymer actuators has demonstrated large progress [34], however they require further development and are not feasible at this stage for millirobotics applications.

Electromagnetic actuators do not scale well and require complex microfabrication processes for manufacturing. Piezoelectric actuators found the most financial success for small scale actuation [35, 36] due to high achievable forces (single Newtons) and low displacement resolution (nm scale). Despite such an impressive performance characteristics, implementation of piezoelectric actuators in millirobotics applications is not easy due to manufacturing and integration complexity. Electrostatic actuators have only moderate power density performance metrics due to limitation of the displacements to achieve high forces.

The other parameters that are important for actuators in the scope of this work are non-quantifiable – the manufacturing simplicity, ease of integration with mechanisms, and possibility of assembly free manufacturing. Piezoelectric actuators are capable of producing higher force at similar displacements compared to electrostatic actuators. However, the fabrication process of high quality piezoelectric actuators is a multistep complex procedure which makes any additional steps for integration/robustness improvement highly unlikely. Electrostatic actuators, on the other hand, can be manufactured using well developed MEMS processes in as little as one etch step. Taking into account all reasons above, electrostatic actuation was chosen for the proposed MEMS motor.

2.2 Electrostatic Inchworm Motor

2.2.1 Electrostatic Actuation

For clarity, in this work the term "motor" will refer to the entire driving mechanism, and the term "actuator" will be used to describe a part of the motor that actually generates

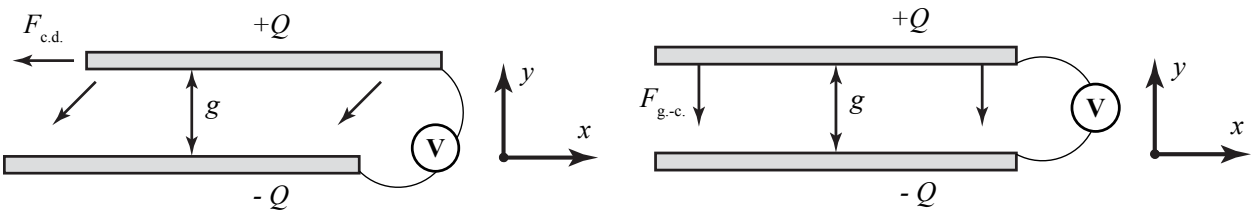

(a) Comb drive (b) Gap-closing

Figure 2.1: Electrostatic actuators

force when voltage is applied.

Electrostatic actuators operate due to Coulomb forces of attraction appearing between two electrodes when electric potential difference (voltage) is applied between them. There are two main types of electrostatic actuators: comb drive actuators in which movement occurs parallel to the electrodes so that the gap between electrodes stays constant and the overlap area increases (Figure 2.1a); and gap-closing actuators in which movement occurs perpendicular to the electrodes so that the gap between electrodes decreases and the overlap area remains constant (Figure 2.1b).

The electrostatic force between electrodes in a comb drive actuator can be calculated using the parallel plate assumption as

$$F_{\text{c.d.}} = \frac{1}{2}\frac{\varepsilon_r \varepsilon_0 A}{g} V^2, \tag{2.1}$$

where ε_r is the relative dielectric permittivity of the medium between electrodes, ε_0 is the dielectric permittivity of vacuum, A is the overlapping area of the electrodes, g is the gap between the electrodes, and V is the voltage difference between electrodes. The electrostatic

force in a gap-closing actuator has a very similar structure

$$F_{\text{g.-c.}} = \frac{1}{2}\frac{\varepsilon_r \varepsilon_0 A}{g^2} V^2. \tag{2.2}$$

From comparison of (2.1) and (2.2), it is clear that the gap-closing actuators can exert much higher forces than comb drives when the distance between electrodes is on the order of several microns. This, however, puts a severe limitation on the total displacement since it is limited by the maximum gap. A gap-closing configuration [37] of electrostatic actuation was selected over comb drives [38] due to much higher achievable forces.

2.2.2 Inchworm Principle

One of the methods to circumvent the motion constraint of the gap-closing actuators is to implement the inchworm driving principle in which large displacements are accumulated in small steps. This principle is accomplished by using two or more actuators that perform the same cyclic motion in which they engage with a shuttle, move it one step, disengage, and return to the initial position (Figure 2.3). The actuators operate out of phase so that at least one of the actuators is in contact with the shuttle at all times. Several different inchworm motor designs have been presented in [37, 39–46]. One disadvantage among previous designs is the inefficient actuation and use of space which leads to a decrease in force density and efficiency. The inefficiencies are caused either by extra actuators that do not contribute to the output force (e.g. clutch actuators), or by large and unoptimized mechanisms that transfer the driving actuator motion to the shuttle.

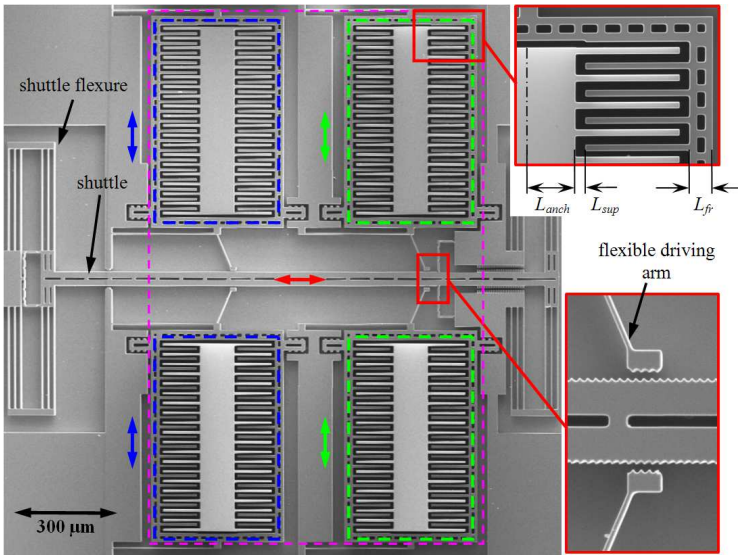

Figure 2.2: SEM image of the manufactured electrostatic inchworm motor with flexible arm. The dashed lines outline the gap-closing actuators: blue line denotes actuators A, green line denotes actuators B. The magenta line represents the total area of the motor

The inchworm motor introduced in [20] (Figure 2.2) implements an angled flexible drive arm that enables both grabbing and pulling the shuttle with one actuator. The symmetric design of the gap-closing actuators on each side of the shuttle balances out the reactions from the engaged drive arms and allows moving even untethered shuttles. This means that the displacements are limited only by the length of the shuttle. The flexible drive arm design offers several advantages over previous designs. First, it substantially reduces the footprint of the inchworm motor by eliminating the clutch actuator and minimizing the driving mechanism. Second, removal of the clutch actuator simplifies the control of the motor.

The introduced actuator requires only two independent voltage signals (Figure 2.3), unlike previous inchworm motors. Such a simplification can also be used to increase the

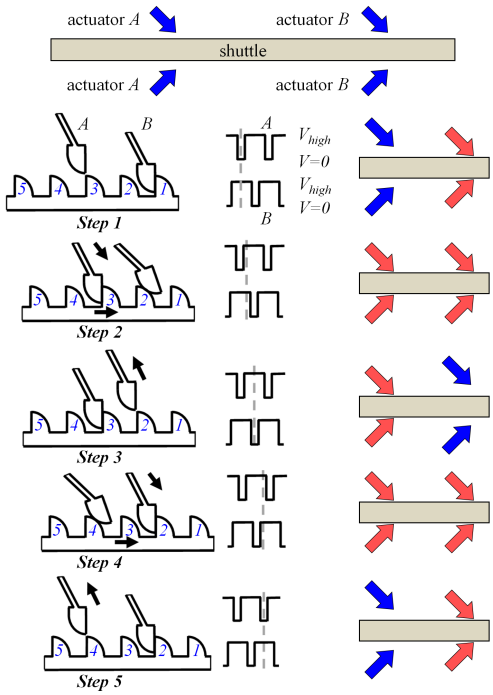

Figure 2.3: Operation cycle of the inchworm motor with flexible arm. The voltage on each actuator is switched between V_{high} and 0. The voltage is applied on actuators A and B out of phase.

motor speed as the time of one step cycle decreases. Finally, removal of the clutch actuators that do not contribute to the motor's output force decreases parasitic capacitance that in turn increases motor's efficiency.

The movement of gap-closing actuators (Figure 2.2) is perpendicular to the shuttle; however, the flexible driving arm attached to these actuators is angled with respect to the shuttle. Therefore, upon engagement with the shuttle, the driving arm applies force in both transverse and longitudinal directions. Since the electrostatic actuators on both sides of the shuttle are symmetrical, the transverse forces are equal and opposite in direction, thus their net is zero. The longitudinal forces are equal in magnitude and direction, thus the total

pushing force is their sum. Once the electrostatic force overcomes stiffness of the arm and the load force on the shuttle, the arm bends and pushes the shuttle. Thus, motion perpendicular to the actuator displacement is achieved. The operation principle and actuation cycle of the inchworm motor is represented in Figure 2.3. Initially, one pair of opposite gap-closing actuators engages with the shuttle, pushes it forward and holds it in place. After that, the second pair of actuators engages with the shuttle, pushes it and holds while the first pair is released and returns to its initial position. Repetition of these steps allows for large final displacements. The nature of this design allows driving the shuttle only in one direction. However, if the shuttle is supported by flexures, they will bring it back to its starting location when all actuators are turned off and the arms are disengaged.

2.2.3 Symmetric "Pull-in" Instability

The use of flexible driving arms architecture fixes the instability problem that arises when mirror symmetric gap-closing actuators push on a shuttle from two sides. Figure 2.4 demonstrates two ways of transferring force to the shuttle – with and without the flexible arm. In case of the rigid contact (no flexible arm), the total force exerted on the shuttle from both sides can be for practical purposes written as

$$F_{tot} = \frac{(A_t - A_b)\, V^2}{(g_0 - y)^2} - (B_t - B_b)\, y, \tag{2.3}$$

where the first term represents the difference of electrostatic forces from top (A_t) and bottom (A_b) actuators, and the second term similarly represents the impact of restoring springs.

Since the structure of (2.3) is identical to one describing a standard gap-closing actuator with a returning spring, it can be concluded that F_{tot} is unstable above some applied voltage V (due to "pull-in" instability [47]) unless both actuators are exactly the same ($A_t = A_b$) which is unrealistic. This instability results in one of the actuators "overpowering" the other and pushing the shuttle off the middle/symmetry position which can disrupt the motor's performance especially for the untethered shuttle.

In Figure 2.4b the forces are transferred to the shuttle through the flexible arm (described as a spring). In this case the resultant force on the shuttle is

$$F_{tot} = (k_t - k_b)\, y, \tag{2.4}$$

where k_t and k_b are spring constants of top and bottom flexible arms. This is a stable equation, and assuming $k_t = k$, $k_b = k + \Delta k$, $k \gg \Delta k$, the shuttle displacement away from the middle can be calculated as

$$\Delta = -\frac{\Delta k}{2k} y \ll y.$$

A similar solution is obtained when accounting for displacement differences between top and bottom actuators. This indicates that mirror symmetric gap-closing actuators with flexible arms do not significantly disturb the middle position of the shuttle and can be used for operation without shuttle tethers.

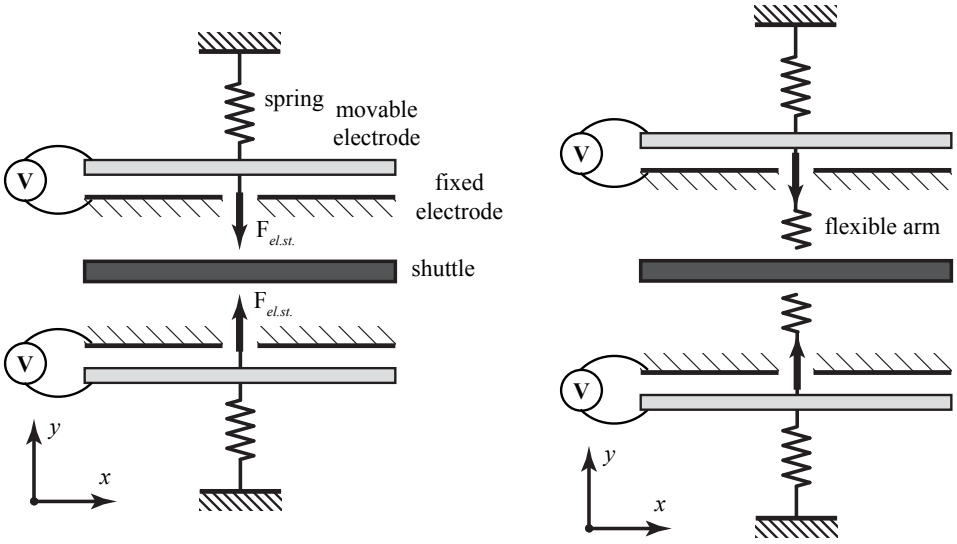

(a) Rigid contact (b) Flexible arm contact

Figure 2.4: Force transfer to the shuttle from mirror symmetric gap-closing actuators

2.2.4 Mechanism Analysis

The main goal of the flexible arm is to transfer force and displacement to the shuttle. To perform these functions, it has to be flexible enough to bend during operation and stiff enough not to buckle. Thus, the flexible driving arm was modeled as a rigid beam with a torsion spring (emulating the arm's bending stiffness) at the pivot point. A kinematic diagram of this mechanism is represented in Figure 2.6. Assuming small movements during one step ($\Delta x, \Delta y \ll L_{\text{arm}}$ - length of the driving arm), the displacements of the actuator and shuttle are related as $\Delta x \approx \Delta y \tan \alpha$, where α is the angle of the driving arm in relation to the shuttle. With the same assumptions, the small changes in the arm angle α during a step can be neglected, and the force transferred to the shuttle can be found using static

equilibrium conditions. The load force (F_{load}) in Figure 2.6 is

$$F_{\text{load}} = \frac{F_{\text{y}}}{\tan\alpha} - K_{\varphi}\frac{\Delta x}{L_{\text{arm}}^2 \sin^2\alpha}, \tag{2.5}$$

where F_{y} is the vertical force applied by the electrostatic actuators, and K_{φ} is the torsion spring constant of the flexible arm.

From classical beam theory, K_{φ} can be estimated as $K_{\varphi} = EI_{\text{arm}}/L_{\text{arm}}$, where I_{arm} is the area moment of inertia of the flexible arm's cross section. Since the cross section is a rectangle, $I_{\text{arm}} = tb^3/12$, where b and t are the width and the thickness of the flexible arm, correspondingly. The second term in (2.5) represents the force that is required to bend the flexible driving arm and can be considered as a loss. To minimize this term, the driving arm has to be very flexible (small K_{φ}). However, K_{φ} cannot be too small because the driving arm will be in danger of buckling. Thus, the lower boundary for K_{φ} (or upper boundary for L_{arm}) is the Euler beam buckling force:

$$F_{\text{buckle}} = \frac{\pi^2 E I_{\text{arm}}}{\left(K_{\text{b}} L_{\text{arm}}\right)^2} = K_{\varphi}\frac{\pi^2}{K_{\text{b}}^2 L_{\text{arm}}} > \frac{F_{\text{y}}}{\sin\alpha}, \tag{2.6}$$

where K_{b} is the beam effective length factor that depends on the conditions of the end support for the beam. In this design, the flexible arm is rigidly fixed to the frame of the gap-closing actuator, but the end that engages with the shuttle can pivot (pin end condition), therefore $K_{\text{b}} = 0.7$. To minimize the losses in the flexible arm, K_{φ} was set to withhold the

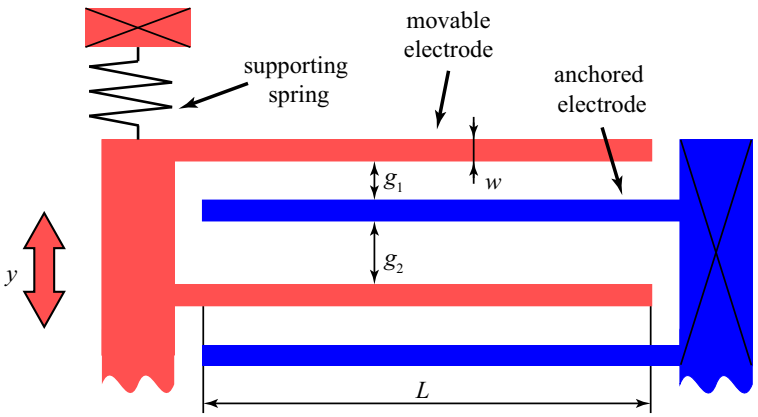

Figure 2.5: Layout of gap-closing actuator. Blue electrodes are rigidly fixed to an anchor. Red electrodes are supported by a spring and can move in the y direction. w is the width of electrodes, L is the overlapping length of electrodes, g_1 is the forward gap (movement toward the shuttle), g_2 is the backward gap.

applied forces without buckling with a safety factor of n:

$$K_\varphi = \frac{nF_\mathrm{y}K_\mathrm{b}^2 L_\mathrm{arm}}{\pi^2 \sin\alpha} = \frac{EI_\mathrm{arm}}{L_\mathrm{arm}} \Rightarrow L_\mathrm{arm} = \sqrt{\frac{EI_\mathrm{arm}\pi^2 \sin\alpha}{nF_\mathrm{y}K_\mathrm{b}^2}}. \tag{2.7}$$

Force transferred by the flexible arm is generated by the electrostatic attraction in the gap-closing actuators (Figure 2.5). From [37], this force is

$$F_\mathrm{el.st.}(y) = \frac{1}{2}\varepsilon_0 N V^2 L t \left(\frac{1}{(g_1 - y)^2} - \frac{1}{(g_2 + y)^2} \right), \tag{2.8}$$

where ε_0 is permittivity of free space, N is the number of electrode pairs in the actuator, V is the applied voltage, L is overlapping length of the electrodes, t is the thickness of the electrodes (thickness of the structural layer of the silicon wafer), g_1 and g_2 are the frontside and backside gaps between the electrodes, and y is the actuator displacement. Due

to the interdigitated layout of the gap-closing actuator, the movable electrodes experience electrostatic force from both front and back fixed electrodes.

Electrostatic force (2.8) is not entirely transferred to the shuttle as part of it is spent to deflect the flexures that support the movable set of electrodes (spring constant k_{spr}). Thus, the ultimate force transmitted from actuators to the shuttle through the flexible arm mechanism is

$$F_{\text{y}} = F_{\text{el.st.}} - k_{\text{spr}}\Delta y. \tag{2.9}$$

For area density calculations, area of the gap-closing actuator (Figure 2.5) is

$$A = N_{\text{act}} N (2w + g_1 + g_2) L, \tag{2.10}$$

where $N_{\text{act}} = 2$ is the number of actuators in the inchworm motor (A and B in Figure 2.3), and N is the number of electrode pairs in the actuator. This formula accounts only for the area occupied by the electrodes and dismisses the motor periphery, which includes bonding pads, actuator frame, anchors, etc. This simplified area allows for calculating absolute maximum characteristics of the motors, which can be compared to those of other devices. The periphery varies significantly from design to design, and it is difficult to estimate during the initial design stage.

2.2.5 Constraints and Limitations

The driving force can be transferred from an actuator to a shuttle through frictional contact [44] or through teeth contact [37]. The main advantage of the frictional contact is the ability to make nanosize steps, which is extremely important for precise positioning

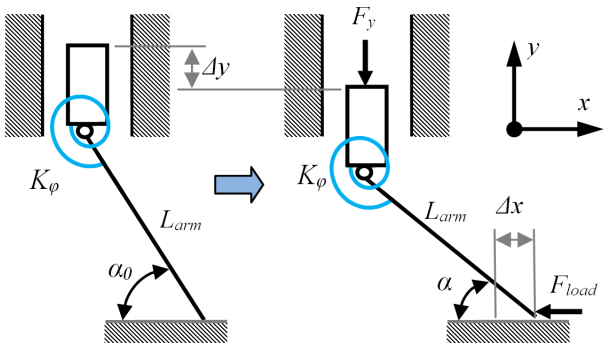

Figure 2.6: Kinematic diagram of the flexible driving arm where F_{y} is the force from electrostatic actuator, K_φ is the torsion stiffness of the flexible driving arm, L_{arm} is the length of the arm, Δy is the step displacement of the electrostatic actuator, and Δx is the step displacement of the shuttle.

applications. The drawbacks of frictional contact are shuttle slipping and the dependence of the step size on the load force [42]. In teeth contact, on the other hand, slipping of the shuttle occurs only at high applied forces, but the step size is limited to the minimal feature (MF) size available from the fabrication process. The teeth layout, shape, and their dimensions are represented in Figure 2.7. For an inchworm mechanism to work, the sum of shuttle displacements from all actuators has to be a multiple of teeth pitch ($2MF$). Since the number of actuators (N_{act}) was chosen to be 2 (A and B), and they are identical, the unit shuttle displacement from one actuator has to be $\Delta x = MF$.

The gaps in the actuator can be calculated based on the ratchet teeth requirements and the arm's angle. The front gap (movement towards the shuttle) consists of three parts. The first part is the distance between the flexible arm and the shuttle; from Figure 2.7 it is equal to $2MF$. The second part is the displacement of the actuator corresponding to movement of the shuttle by one step. From Figure 2.6 this displacement approximately

equals to $\Delta y = \Delta x / \tan\alpha$. The last part is the final gap (g_{f}) between electrodes that prevents them from shorting. This gap is necessary due to "pull-in" instability of the gap-closing actuator [47]. It is realized by introducing mechanical stops that limit the displacement of the movable electrodes. Overall, the front gap of the electrostatic actuator equals to

$$g_1 = 2MF + \Delta y + g_{\mathrm{f}}. \tag{2.11}$$

The back gap (movement away from the shuttle) has to be larger than the front gap, thus it was assumed that $g_2 = k_{\mathrm{back}} g_1$, where $k_{\mathrm{back}} > 1$. Based on these definitions, when the flexible arm engages with the shuttle, the front and back gaps are

$$\begin{aligned} g_1^{\mathrm{eng}} &= \Delta y + g_{\mathrm{f}} \\ g_2^{\mathrm{eng}} &= k_{\mathrm{back}} g_1 + 2MF, \end{aligned} \tag{2.12}$$

In this study, k_{back} was set at 1.5. This was done since calculations showed that the backward force is insignificant upon engagement with the shuttle, even with smaller values of k_{back}. However, the dynamics of the gap-closing actuator, which are not considered in this work, will prevent the motor from working properly at high speeds if $k_{\mathrm{back}} < 1.5$.

Electrostatic force and force density linearly increase with electrode thickness t (2.8), which is bounded by the limitations of the manufacturing process. Features in the silicon layer are patterned using a deep reactive ion etch (DRIE). The quality of this process is defined by the aspect ratio (depth over width) of the trenches it can etch. Although aspects ratios up to 130 are achievable with the DRIE process [48], in this work, aspect ratio (λ) was assumed to be 20 as it was limited by the available fabrication tools. The smallest features

in the designed motor are the ratchet teeth and the gap between the flexible arm and the shuttle (Figure 2.7). Thus, maximum thickness of the electrodes can be expressed as

$$t = \lambda MF,\ t \leq 500\,\mu\text{m}. \tag{2.13}$$

The inequality constraint comes from the maximum reasonable thickness of the silicon wafer. It should be noted that due to the single mask manufacturing process, the thickness t of all inchworm motor parts (electrodes, flexures, flexible arm, etc.) is assumed to be the same.

Electrostatic force greatly benefits from high actuation voltages since it increases proportionally with V^2 (2.8). However, "pull-in" instability of gap-closing actuators imposes constraints on the maximum applied voltage and on the stiffness of the electrode fingers. The final gap g_f prevents shorting only if the electrodes are absolutely rigid (short and thick). Osterberg in [49] derived an expression that relates the maximum voltage and the dimensions of the electrodes, which can be rewritten to define the maximum electrode length for a fixed maximum voltage

$$L_\text{max} = \sqrt[4]{\frac{0.28Ew^3g_\text{f}^3}{\varepsilon V^2\left(1+0.42\frac{g_\text{f}}{t}\right)}}, \tag{2.14}$$

where E is the Young's modulus of the electrode's material (silicon).

Gap-closing actuators take advantage of high electric fields (high voltages, narrow gaps) which create the possibility of breakdown of the insulator (air). This issue was investigated extensively in [50] and [51]. The results of studies showed that the breakdown does not occur at voltages below 300 V for any gap. In this work, all calculations and tests were done at much lower voltage of 110 V.

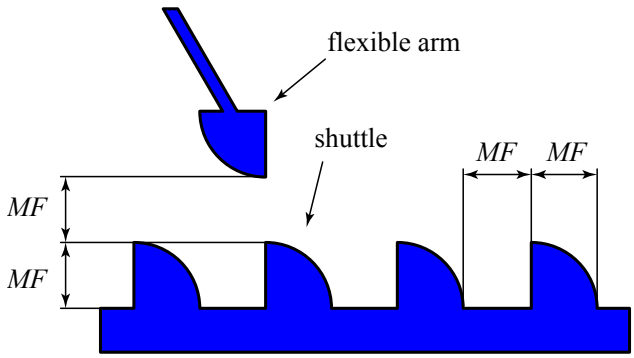

Figure 2.7: Ratchet teeth between the flexible arm and the shuttle. All teeth are designed to be the size of the minimum feature (MF) size.

The set of movable electrodes in the gap-closing actuator is supported by flexures (Figure 2.5). Besides support, the flexures act as spring elements that return electrodes to the initial position when voltages is removed. High stiffness (spring constant) of these flexures reduces the maximum force that the actuator can apply to the shuttle (2.9). However, the manufacturing process requires the flexures to be robust. Additionally, possible charge entrapment and stiction between the electrodes or friction in the ratchet mechanism require flexures to be reasonably stiff. The maximum spring constant that still allows for pull-in can be calculated as [47]

$$k_{\text{spr}}^{\max} = \frac{27}{8}\frac{\varepsilon t L N}{g_1^3}V^2. \tag{2.15}$$

2.2.6 Force Density Optimization

In this work, the force density is defined as the ratio of the actuator force transferred to the shuttle F_{load} to the area occupied by the electrodes (A). The constant parameters used in the study are shown in Table 2.1. The spring constant of the actuator flexures was

Table 2.1: Parameters and constants used for optimization procedure

Parameter	Value/range	Description/justification
MF	$1 \ldots 5$	Based on currently available technologies
α	$10° \ldots 85°$	Entire range, except extremes
g_f	$1\,\mu\mathrm{m}$	Final gap, based on previous testing experience
N	40	Number of pairs of electrodes in each actuator
V	$110\,\mathrm{V}$	Maximum applied voltage, based on previous testing experience
λ	20	DRIE aspect ratio, based on available equipment characteristics
n	2	Safety factor for flexible arm buckling constraint (2.6)
K_b	0.7	Beam effective length factor in (2.6)
E	$170 \cdot 10^9\,\mathrm{Pa}$	Averaged Young's modulus of silicon

calculated to maintain the resonant frequency of the actuator at 10 kHz. This number was chosen based on preliminary tests; higher frequencies are infeasible in this modeling due to unaccounted viscous damping, which becomes dominant as operating frequencies increase. The resonant frequency was calculated as

$$f_\mathrm{res} = \frac{1}{2\pi}\sqrt{\frac{k_\mathrm{spr}}{m}} = \frac{1}{2\pi}\sqrt{\frac{k_\mathrm{spr}}{\rho t L w N}}, \tag{2.16}$$

where ρ is the density of silicon. The optimization problem is defined as

$$\begin{aligned} \underset{MF,\alpha,w}{\text{maximize}} \quad & F_\mathrm{load}/A \\ \text{subject to} \quad & g_1 = 2MF + \Delta y + g_\mathrm{f} \\ & g_2 = k_\mathrm{back} g_1 \\ & t = \lambda MF \leq 500\,\mu\mathrm{m} \\ & L \leq L_\mathrm{max} \\ & k_\mathrm{spr} \leq k_\mathrm{spr}^\mathrm{max} \\ & f_\mathrm{res} = 10\,\mathrm{kHz} \end{aligned} \tag{2.17}$$

The optimization was performed in MATLAB. A regular 2-D mesh in the MF-α plane was generated, and the MATLAB native function `fmincon` was used to compute the maximum of the objective function (F_{load}/A) at the mesh points with the aforementioned constraints.

The calculated force density as a function of minimum feature and flexible arm angle is shown in Figure 2.8. The solid red line traces maximum of force density for different values of MF. The blue star marks the maximum force density for given constraints which was calculated to be $10.9\,\text{mN/mm}^2$ at $MF = 1\,\mu\text{m}$, $\alpha = 55°$, and $w = 1\,\mu\text{m}$.

Several conclusions can be drawn from the results of the optimization. Firstly, the objective function increases as minimum feature size decreases, even though the thickness of inchworm motor components changes linearly with MF (2.13). This happens since smaller values of MF simultaneously increase the numerator (F_{load}) and decrease the denominator (A) of the objective function. Secondly, the maximum of the objective function is achieved at the lowest boundary of the electrode width w. It can be shown that for the given constraints the force density changes as $1/w$.

2.2.7 Motor Efficiency

Maximum theoretical efficiency of an electrostatic gap-closing actuator can be calculated by making a few simple assumptions. Firstly, it is assumed that the total energy transferred to the actuator from a power supply is equal to the maximum energy stored in the capacitor formed by the interdigitated electrodes. Maximum energy implies that it is

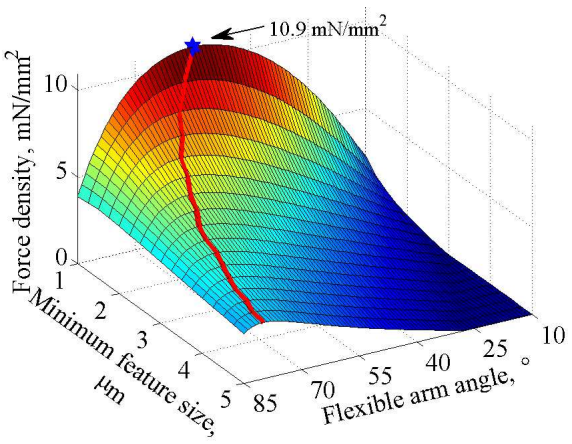

Figure 2.8: Theoretical force density of the new inchworm motor (at 110 V). The blue star indicates the maximum of force density ($MF = 1\,\mu\text{m}$, $\alpha = 55°$).

calculated for the largest possible capacitance which is achieved when the gap between the electrodes is the smallest possible. Then, the total energy input equals

$$E = \frac{1}{2}CV^2 = \frac{1}{2}\frac{\varepsilon NtL}{g_\text{f}}V^2. \tag{2.18}$$

Secondly, it is assumed that the actuator works against a constant load for each step. This is a valid assumption because the displacement of the actuator is small. The work performed by the actuator can be calculated as

$$W = F_\text{eng}\Delta y = \frac{1}{2}\frac{\varepsilon NtL}{g_\text{eng}^2}V^2\Delta y, \tag{2.19}$$

where F_eng and g_eng are the actuator force and gap between electrodes at the moment the angled arm engages with the shuttle. Even though actuator force will increase as the shuttle is pushed forward, it is assumed that useful work on a load is limited to this initial

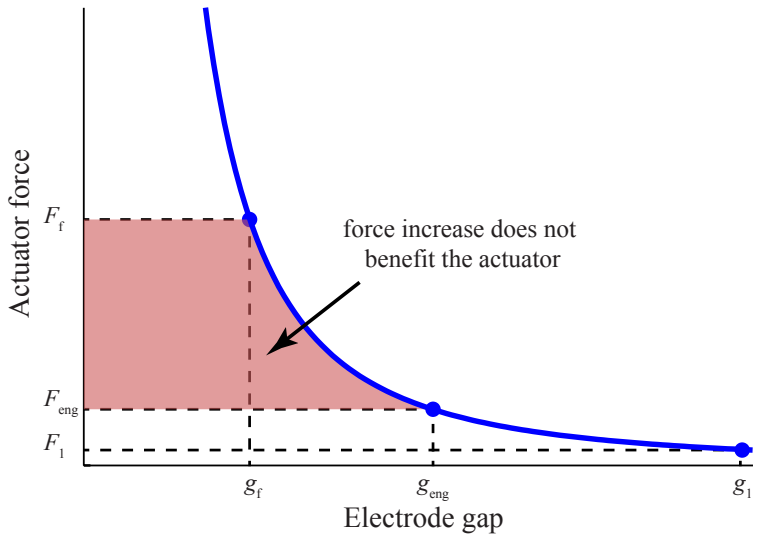

Figure 2.9: Plot of gap-closing actuator force changing with the gap between electrodes

engagement force. Efficiency of the actuator is defined as the ratio of work done to the transferred energy

$$\eta = \frac{W}{E} = \frac{g_f \Delta y}{g_{eng}^2}, \tag{2.20}$$

but $\Delta y = g_{eng} - g_f$, then (2.20) becomes

$$\eta = \frac{g_f(g_{eng} - g_f)}{g_{eng}^2} = \frac{g_f g_{eng} - g_f^2}{g_{eng}^2} = s - s^2,$$

where $s = g_f/g_{eng} < 1$. Simple calculation shows that the maximum of this expression is achieved at $s = 0.5$ and equals to $\eta = 0.25$ or 25 % for an inchworm gap-closing actuator that is voltage driven. This limit is much smaller than the theoretical efficiency for electrostatic actuators (90 %, [15]) due to inability to use forces higher than F_{eng} (Figure 2.9) since high load forces prevent the electrode gap from closing past g_{eng}.

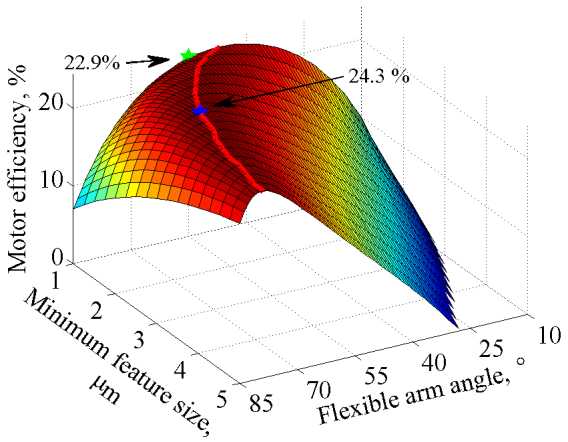

Figure 2.10: Motor efficiency in the force density optimization. The blue star indicates the maximum motor efficiency ($MF = 2.75\,\mu\text{m}$, $\alpha = 71°$). The green star indicates the motor efficiency at the maximum of force density ($MF = 1\,\mu\text{m}$, $\alpha = 55°$).

The designed inchworm motor contains four gap-closing actuators, thus its overall efficiency can not exceed individual efficiency of the actuators. In fact, efficiency in a full inchworm motor with a flexible arm is less than 25 % due to losses in the flexible arm and flexures. By accounting for these force losses, the inchworm motor efficiency was calculated in the force density optimization analysis. The maximum calculated efficiency of 24.3 % was achieved at $MF = 2.75\,\mu\text{m}$, $\alpha = 71°$ (Figure 2.10). Although locations of the efficiency maximum and force density maximum were different, the efficiency values at these two points varied only by 1.4 %.

2.3 SOI Electrostatic Inchworm Motor

The procedure for maximizing the force density described in Section 2.2.6 was used to compute the dimensions of electrostatic inchworm motor. The obtained characteristics are represented in Table 2.2.

2.3.1 Fabrication

The inchworm motors were fabricated on a silicon-on-insulator (SOI) wafer (40 µm structural layer, 5 µm oxide layer) using a standard SOI manufacturing process. The devices were transferred to the silicon layer in a single DRIE step with 2 µm minimum feature size. After the etch, the wafer was coated with photoresist to protect small gaps from particle contamination and diced. Then, the photoresist layer was ashed with oxygen plasma and devices were released by wet etching the buried oxide in 49 % hydrofluoric (HF) acid. No stiction of silicon features was observed during drying of devices due to thick structural and oxide layers. After drying, aluminum wires were bonded directly to the silicon pads. To prevent electrical shorting of the electrodes due to accidental contact during the tests, a 160 nm layer of aluminum oxide (Al_2O_3) was conformally deposited on the released structures using an atomic layer deposition (ALD) process [52]. Also, Mayer showed that Al_2O_3 layer decreases friction and is a good wear resistive coating [53] which is important for ratchet teeth operation. Overall, fabrication showed a high yield ($> 90\,\%$), where the largest source of defects was the photolithography step.

The tests of the manufactured motors showed that the mechanism as designed is insensitive to the final shape of the ratchet teeth which are often significantly affected by fabrication. Figure 2.11 demonstrates a comparison of the designed layout of the ratchet teeth and their shape in two fabricated devices (on different wafers and different MF size). The variations of shape in manufactured teeth are a result of different parameters during the DRIE step and smaller teeth size. Despite such drastic variations in teeth shape, both

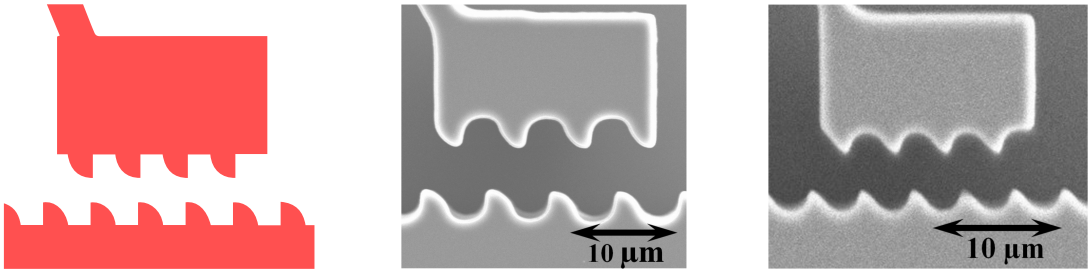

(a) (b) (c)

Figure 2.11: Teeth shape comparison. (a) Layout of ratchet teeth. (b) Manufactured teeth with 3 µm minimum feature (and teeth) size. (c) Manufactured teeth with 2 µm minimum feature (and teeth) size.

ratchet mechanisms performed properly and pushed the shuttle without slipping.

2.3.2 Testing Results

The optimization analysis above provided the basis for design and manufacture of the electrostatic inchworm motor. Dimensions of manufactured devices were chosen from the results of the force density optimization with periphery. The design was selected for the highest force density at $MF = 2\,\mu m$, which was the smallest feature size available for fabrication. The dimensions and the calculated characteristics are listed in Table 2.2. The motors were actuated using a square wave signal (Figure 2.3) with a maximum voltage of 110 V. The maximum voltage was determined based on preliminary tests of electrostatic actuators. At this voltage level the actuators showed repeatable performance, whereas at higher voltages charge entrapment in the deposited aluminum oxide caused opposite electrodes to stick even when the voltage was turned off.

The stiction of actuators during operation decreased dramatically in motors with Al_2O_3

Table 2.2: Calculated characteristics of the manufactured motors

MF	α	w	L	L_{arm}
2 µm	69°	7.28 µm	104 µm	124 µm
g_1	g_2	t	k_{spr}	F_{load}/A
5.77 µm	8.65 µm	40 µm	11.1 µN/µm	2.00 mN/mm^2

due to the frequent contact and welding of the fingers in the uncoated devices. The long term tests showed that after approximately 1 million engagements of the flexible arm and the shuttle, some debris started accumulating between the teeth and while the motor still worked, performance became unpredictable.

2.3.2.1 Force Measurement Approach

Direct force measurement in MEMS actuators is a difficult task due to the small actuator size and the lack of suitable sensors. The more common indirect measurement method calculates the force from the deflection of a spring mechanism (shuttle flexure) that is moved by the motor. Then, assuming that deformations are linear, the motor force is

$$F = k_{\text{flex}} \cdot \Delta x, \tag{2.21}$$

where k_{flex} is the spring constant of shuttle flexures, and Δx is its displacement.

In this research, displacement measurements were done using an optical microscope by monitoring movement of a regular pattern on the object of interest [54]. Spring constants were measured using simplified analysis techniques proposed by Clark [55]. Several comb drive resonators with three types of flexures were placed on each die. These flexures were

identical in design to the ones supporting the shuttle in the inchworm motors but with varying length and, therefore, spring constant. The obtained calibrated flexure spring constants were used for performance characterization of the manufactured inchworm motors (2.3.2.4). The measured calibration data and its comparison with analytical values is shown in Table 2.3. Analytical values were based on the designed dimensions accounting for the lateral etch from SEM measurements. The same dimensions were used to calculate the analytical resonant frequency from (2.16). The measurements of resonant frequency were performed by actuating the comb drives with a biased sinusoidal signal and visually observing the amplitude of vibrations.

The calibrated spring constants were approximately a half of the analytically predicted values. Reasons for such a dramatic difference include fluctuations in lateral etch, the footing effect in DRIE on SOI wafers, and imprecise values of the material properties. More detailed inspection of the manufactured features showed gradual widening of the DRIE trenches closer to the bottom which resulted in trapezoidal cross section of silicon features. Considering that bending stiffness of flexures varies with width cubed, even small change in lateral dimensions will result in significant change of spring constant.

The measured resonant frequency showed the same deviation from the analytical values as the capacitance measurements. Although the performed frequency measurements are more straightforward than the capacitance measurements, generally they do not provide the same level of accuracy since the resonant mass can only be estimated based on the known dimensions. However, the resonant frequency can be used to estimate the damping effects

Table 2.3: Comparison of analytical and measured characteristics of the supporting flexures

Flexure	Spring constant, N/m		Ratio	Resonant frequency, kHz		Ratio^2
length, µm	Analytical	Measured	an./m.	Analytical	Measured	(an./m.)^2
300	40.8	19.8	2.06	10.7	7.43	2.07
350	25.7	12.6	2.04	8.48	5.94	2.04
400	17.2	8.60	2.0	6.94	4.85	2.05

or the change in the resonant mass.

2.3.2.2 Maximum Load

Maximum load is the maximum force on the shuttle that can be held by the flexible arm mechanism. The measurements of the maximum load were done by applying voltage to one set of electrostatic actuators so that the flexible arms engaged with the shuttle and held it in place. Then, the shuttle was manually pushed with a probe in the direction that the motor pushes it. This was done until upon removing of the probe, the restoring force from the flexures became strong enough to force the shuttle to slip against the teeth contact. The results of the tests on three different motors are presented in Figure 2.12. During these tests, none of the flexible arms were broken or buckled. The slipping of the shuttle occurred when the load overcame the actuator force and pushed the engaged electrodes apart. These measurements were limited by the maximum displacement of the shuttle, thus only loads below 3.7 mN could be tested.

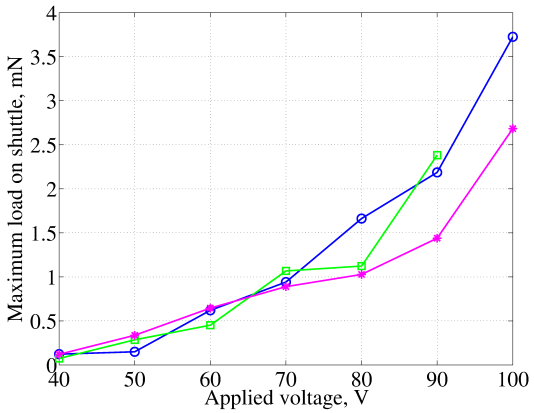

Figure 2.12: Plots of maximum load as a function of voltage

2.3.2.3 Maximum Speed

Maximum speed of the shuttle is a function of the driving voltage frequency. The maximum speed can be achieved if the gap-closing actuators are driven at resonance. This, however, is not a straightforward procedure, as the gap-closing actuators tend to move in a backward direction at the high driving frequencies (dynamic "pull-in" [56]).

Figure 2.13 illustrates the dependence of the shuttle velocity on driving frequency. As expected, this dependence is linear due to constant step sizes, and does not vary for different driving voltages. The shuttle velocity was calculated as an average speed over 15 actuation cycles. All of these tests were done at loads less than the maximum (Section 2.3.2.2) thus no shuttle slipping was observed. The maximum repeatable speed was achieved at 1.2 kHz actuation frequency, which corresponds to a shuttle velocity of 4.8 mm/s. The maximum speed was repeatedly observed only at 90 V and higher voltages.

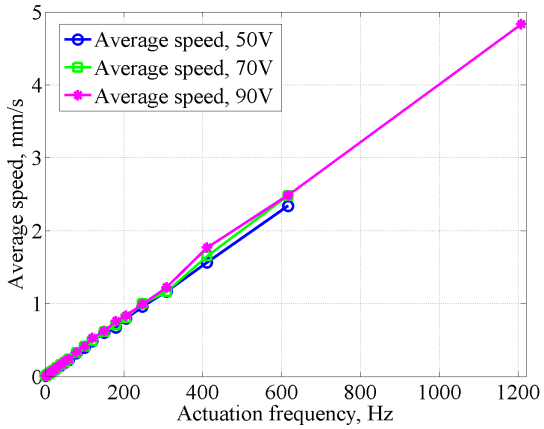

Figure 2.13: Plot of average shuttle speed at different driving frequencies and voltages

2.3.2.4 Maximum Force

The maximum force (stall force) that the actuators can transfer to the shuttle was measured based on the calibrated flexure stiffness. The motor was actuated until the shuttle stopped moving. Then, the total shuttle displacement was measured from a micrograph, and the stall force was calculated using the calibrated spring constant of the shuttle flexures as $F_{mot} = k_{\text{flex}} \cdot \Delta x$. The results of tests with different flexures are represented in Figure 2.14.

The maximum observed displacement was 124 µm in the test with the "softest" flexure (9.76 N/m) at 110 V. A maximum force of 2.23 mN at 120 V was achieved in the test with the "stiffest" flexure (79.3 N/m); however, to remain consistent with the optimization analysis the maximum value at 110 V (1.88 mN) will be considered in further analysis. This maximum force at 110 V is just 10.5 % smaller than the one calculated in the optimization analysis (2.10 mN), which demonstrates the reliability of the model. The area occupied by the motor is 1.36 mm^2 (including all of the peripheral structures), resulting in a realized force density of

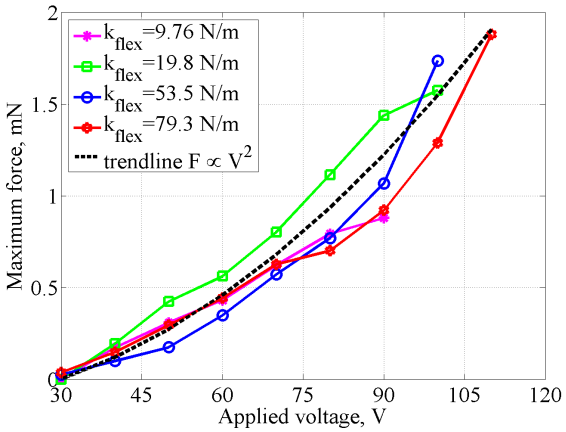

Figure 2.14: Measured maximum shuttle force as a function of applied voltage. The black dashed line is a trendline demonstrating proportionality of the maximum force to V^2

$1.38\,\mathrm{mN/mm^2}$. This measured force density is considerably less than the expected optimized value of $2.00\,\mathrm{mN/mm^2}$. The primary reason for this is an underestimation of the required motor periphery by the model.

The maximum force of the motor shows a quadratic dependence on voltage, as expected for the motor using gap-closing actuators (2.8). The trendline in Figure 2.14 ($F = 0.17\left(V^2 - V_{\mathrm{pull-in}}^2\right)$) demonstrates this proportionality. Zero of the actuator force is shifted due to counteraction of the actuator's supporting flexures.

2.3.2.5 Motor Efficiency

The motor efficiency was calculated as the maximum useful work that the motor can perform divided by the total energy stored in the capacitor formed by the gap-closing electrodes. The maximum work is achieved at maximum force since the step size is constant. Thus, $W_{\mathrm{max}} = F_{\mathrm{max}}\Delta x$, where $F_{\mathrm{max}} = 1.88\,\mathrm{mN}$ at $110\,\mathrm{V}$ (from Section 2.3.2.4) and

$\Delta x = 2\,\mu m$ was measured in shuttle force tests. The maximum energy stored in the gap-closing actuator can be calculated from $E = \frac{1}{2}CV^2$, and its maximum is achieved when the capacitance is the largest and the front gap is the smallest. Capacitance measurements showed that the capacitance of the gap-closing actuators when first engaging with the shuttle was 5.60 pF and increased to 7.10 pF when fully actuated to the final gap, which includes any parasitic capacitance due to packaging and wiring. Therefore, the manufactured motor efficiency is $\eta_{calc} = W_{max}/E_{max} = 8.75\,\%$.

2.3.3 Effects of Al_2O_3 Coating

2.3.3.1 Leakage Current

The highest forces in gap-closing actuators are achieved with electric fields reaching tens of MV/m at which point the field electron emission between interdigitated fingers rises exponentially. In addition to high electric fields, the electron emission is further increased by the sharp scallops which are the artifacts of DRIE step [57]. This emission is the main contributor to the leakage current which can reach hundreds of µA. Considering that the typical capacitance of gap-closing actuators is on the order of pF, the total consumed current at constant operation is on the order of single µA. Therefore, the leakage current can significantly increase the power consumption and drop the motor efficiency.

Originally, Al_2O_3 coating was deposited to prevent interdigitated electrodes from shorting upon accidental contact during operation. However, the tests showed that manufactured devices excellently preserve the charge and shuttle displacement in actuators when discon-

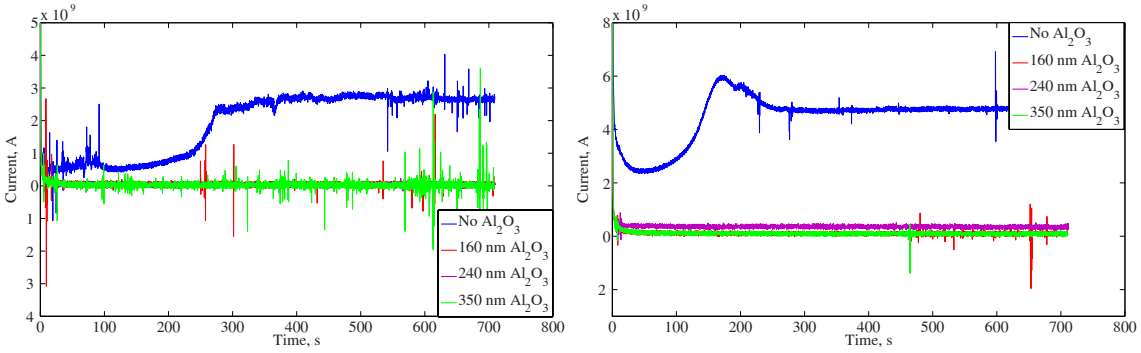

(a) Gap-closing at 70 V (b) Comb drive at 110 V

Figure 2.15: Leakage current as a function of time at constant voltage

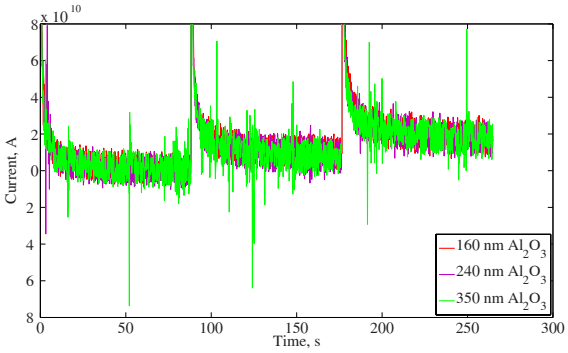

Figure 2.16: Leakage current in gap-closing actuators as a function of time at different voltages

nected from the power circuit. Further investigation demonstrated that 160 nm of aluminum oxide is enough to reduce the leakage current by several orders of magnitude in gap-closing and comb drive actuators (Figure 2.15 . The leakage current increased with applied voltage, however, stayed much lower than the amount required to drive the actuator (Figure 2.16). These measurements were done using Keithley 2410 High-Voltage SourceMeter in the regime of voltage source.

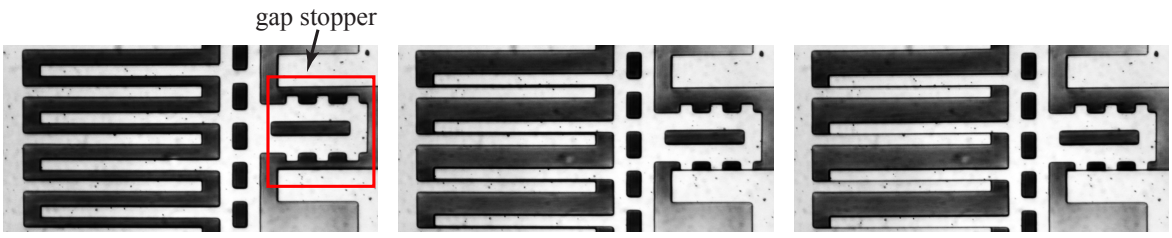

(a) Open (b) Closed (c) Zipped

Figure 2.17: Operation stages of gap-closing actuators

2.3.3.2 Zipping of Interdigitated Fingers

As described in Section 2.2.5, the gap-closing actuators were fabricated with gap stoppers to enforce the final gap $g_f = 1\,\mu m$ and prevent electrode shorting (Figure 2.17a). This design worked well at voltages less than $\simeq 2V_{pull-in}$ (Figure 2.17b). At the higher voltage levels, the rigidity of the actuator frame was not high enough to resist the electrostatic forces which resulted in electrodes coming in rigid contact with each other (Figure 2.17c). The transition to rigid contact starts from the free ends of electrodes and then spreads along the length in zipping fashion. Even though the actuators were not designed to operate with near zero final gaps, no consistent failures were observed in multiple tests with completely zipped electrodes; that is no charge entrapment and no Al_2O_3 film breakdown was noticed in 110 V to 120 V experiments discussed in Section 2.3.2.

2.4 Conclusion

The main focus of this chapter was on modeling and optimization of the electrostatic inchworm motor with a novel flexible arm architecture. This motor consists of two pairs

of gap-closing actuators that are operated out of phase. The force is transferred to the shuttle through angled flexible arms that also allow for achieving the shuttle displacement that is perpendicular to the actuator motion. The motor's model was used to optimize its architecture to maximize the force density.

The optimized inchworm motor was fabricated in a single mask SOI process and evaluated using calibrated flexures for a more accurate measure of force output. The motor demonstrated robust performance, speeds up to 4.8 mm/s, and a maximum shuttle force of 1.88 mN at 110 V. This measured force was within 10 % of the force predicted by the analytical model during the optimization. The resulting force density of 1.38 mN/mm^2 is several times higher than demonstrated by previous in-plane electrostatic inchworm motors. Efficiency of the inchworm motor, measured using capacitance-based measurement methods, was 8.75 % – much lower than the model predicted value of 23.6 %, primarily due to not accounting for the parasitic capacitance of the wiring and motor packaging in the model.

The chapter ends with the discussion of two potentially useful effects of ALD Al_2O_3 coating – dramatic decrease of the leakage current and prevention of the opposite electrodes from shorting when contacting.

Chapter 3

Thick Film Motors

3.1 Introduction

The SOI electrostatic motor (Chapter 2) demonstrated promising performance capabilities. Relatively close model predictions and a relatively high measured stall force offer cautious optimism for a further improved motor implementation. However, the exerted maximum force of 1.88 mN at 110 V is much less than the requirement for a realistic millirobotics application. In addition, the testing experience highlighted some aspects of the motors that (even though were not an issue during careful benchtop tests) could potentially escalate into more severe problems once assembled into a complex system and faced with the challenges of less a controlled environment. As an example, the motors occasionally suffered from broken flexures that rendered them inoperable due to broken symmetry or incapable of return motions. The flexures could break as the result of improper handling (e.g. dropping the die) or accidental collision during operation (e.g. probe slipping). Also, the flexible arm sometimes could not handle the dynamic loads and snapped during shuttle release in the maximum load tests (Figure 3.1). These observations were a reminder about importance of the motors' robustness and reliability especially as a part of a larger assembled structure.

The targeted force of the desired motors for millirobotic applications was on the order

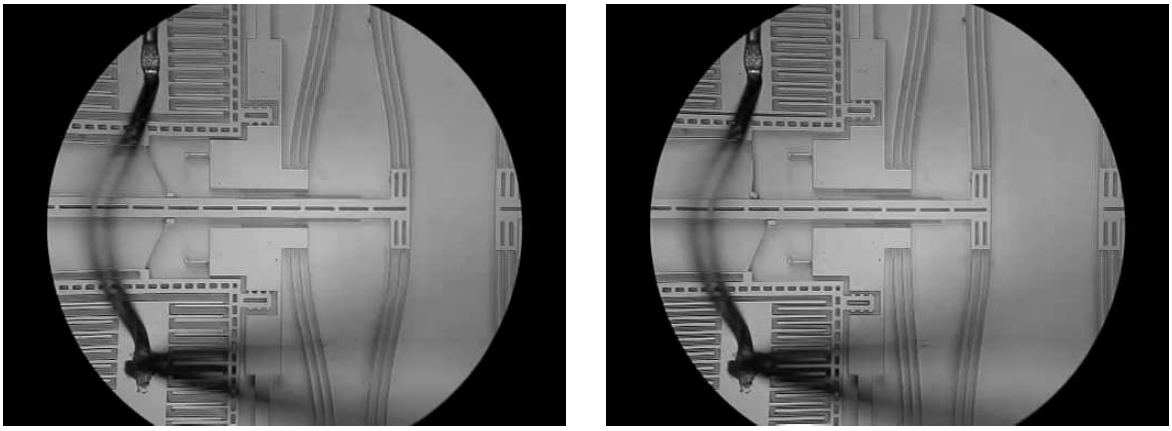

Figure 3.1: Flexible arm before and after snapping

of tens of mN which is ten times higher than the stall force measured in the SOI motors. Several methods were considered to increase the produced force:

1. increase the operating voltage;

2. increase the number of electrodes;

3. reduce the engagement gap (g_{eng}) of the actuators;

4. increase the overlapping area of the electrodes.

The first method can result in charge entrapment and breakdown of air or dielectric film which renders the motor inoperable. The second method increases the overall area of the motor and complicates its architecture due to a requirement for high structural rigidity to efficiently transfer the actuator force to the shuttle. The engagement gap is a design parameter that was optimized to maximize the force area density (2.17). It can be further reduced only by improving the minimal feature size of the fabrication process or by lifting the constraints on electrodes' rigidity to utilize the zipping phenomenon (Chapter 5). The

last approach can be accomplished by increasing length or height of the electrodes. Length is the design parameter that was optimized according to (2.17). Electrode height, set by the structural (silicon) layer thickness, linearly increases the produced force; however, it is constrained by the aspect ratio limitation of the fabrication process.

Considering the challenges described above, two methods were chosen as the next steps in further electrostatic motor development: scaling up by increasing thickness and total size of the motors as described in this chapter and implementing flexible electrodes that circumvent the engagement gap limitation as described in Chapter 5.

In addition to increasing force output, scaling up the motor can be beneficial for its robustness as indicated in [58]. Smith studied MEMS actuators and their performance after sudden accelerations (impacts) and concluded that larger flexures can withstand higher dynamic loads. Moreover, the goals discussed in the Introduction include a motor that is simple to assemble with other structures during mechanism assembly. A typical MEMS motor is too small and fragile for easy integration which made the larger motor scale even more desirable.

3.2 Thick Film Motor Design

Due to increased thickness being one of the major differences, these motors will be referred as "thick film motors" further in the text, in contrast to "SOI motors" in Chapter 2. Thick film motors were designed with the same actuation principle (inchworm movement, flexible arm) as motors in Chapter 2. The same optimization process was used to calculate the

Table 3.1: Calculated characteristics of the through-wafer motors

MF, µm	**7**	**10**	**15**
α, °	79	81	84
g_1, µm	16.4	22.4	32.6
g_2, µm	24.5	33.7	48.9
F_{load}, mN	$2 \cdot 9.49$	$2 \cdot 7.46$	$2 \cdot 5.52$
F_{load}/A, mN/mm^2, no bias	2.10	1.31	0.67

characteristics for $MF = 7$, 10, and 15 µm with the motors' targeted thickness $t = 300$ µm. The results are displayed in Table 3.1. This analysis was done for 40 pairs of interdigitated electrodes in each actuator, a final gap of 1 µm, and estimated resonance frequency of 1 kHz.

3.2.1 Aspect Ratio Limitation

Aspect ratio of achievable trenches (defined as the minimum width over the given depth) in the fabrication process had to be again considered as one of the main limitations in the motor design and optimization process. Since the trench depth is considerably larger in thick film motors compared to SOI, aspect ratio puts a severe constraint on the smallest gap between the electrodes of gap-closing actuators.

Thus, for 300 µm thick motors and $\lambda = 20$, the smallest achievable gap is $g_1 = 15$ µm; this is too large to produce the required level of force. However, g_1 is only the manufactured front gap, the force is transferred to the shuttle when the actuator frame moves and the gap is reduced to g_{eng}.

The difference between these gaps is the distance that the flexible arm needs to travel to engage with the shuttle. From (2.11) and (2.12) this difference equals to $2MF$. Before the

flexible arm engages with the shuttle, the only force counteracting the electrostatic attraction is the restoring force of the supporting flexures. For a properly designed gap-closing actuator, the flexural restoring force is insignificant compared to the actuator's electrostatic force even for large initial gaps.

As a result of this low ratio of spring force to electrostatic force, the effect of the aspect ratio constraint on the produced force is weakened. However, it still reduces the force density as the etched trenches include the distance of $2MF$ which needlessly increases the actuator's area.

3.3 Fabrication Process

To manufacture 300 µm thick electrostatic inchworm motors a through-wafer fabrication process was implemented (Figure 3.2). A similar process with some variations was used in [59–63]. The process started with a prime grade double side polished (DSP) 300 µm silicon wafer doped to a resistivity of at least 10 Ω-cm. Then, a 1.4 µm layer of photoresist was spun on the wafer and patterned using the standard photolithography procedure. The patterned photoresist layer was used as the physical mask in DRIE process of the wafer which was performed to etch shallow ($\approx$ 10 µm) trenches. In step 3, a thin layer (200 nm) of aluminum was deposited using electron beam evaporation. Next, in step 4, the photoresist layer was stripped along with metal on top of it resulting in aluminum left only in the bottom of the trenches ("lift-off" process). In step 5, the silicon wafer was flipped and anodically bonded to a 500 µm Borofloat (or Pyrex) glass wafer so that the etched trenches were sealed. The

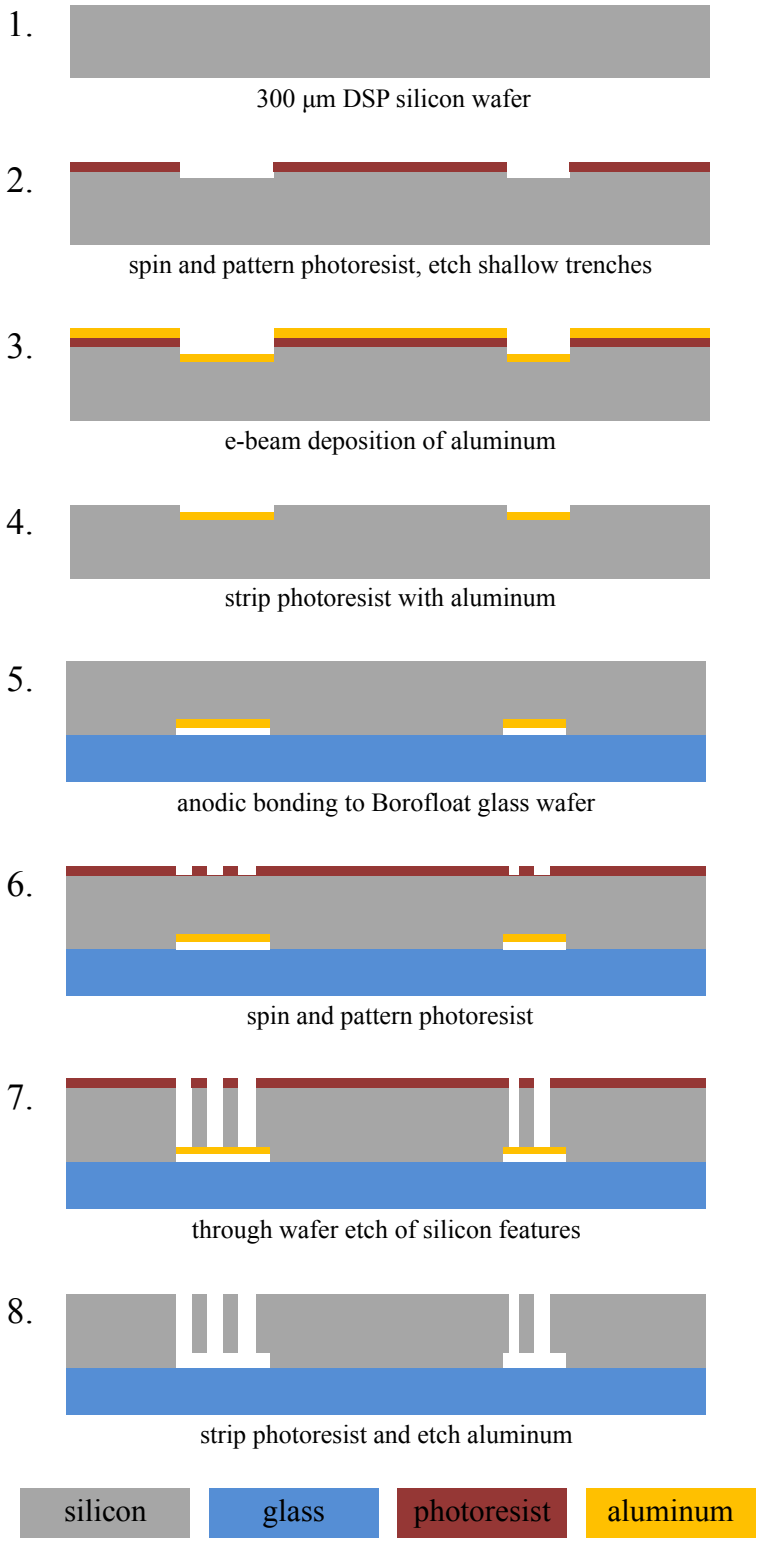

Figure 3.2: Cross section view of the through-wafer fabrication process

wafers had to be thoroughly cleaned from any contamination before bonding since it greatly impacts on the quality of the bond. In step 6, 200 nm thick silicon dioxide (SiO_2 not shown on Figure 3.2) was deposited on the silicon side of the wafer using plasma enhansed chemical vapor deposition.

A 12 µm layer of photoresist (SPR-7.0) was then spun and patterned using the sealed trenches for alignment. The SiO_2 layer was etched in an inductively coupled plasma etcher (with CHF_3 and He_2 reactive ion plasma) thus finishing the physical mask patterning steps. Next, the silicon wafer was etched all the way through until the metal layer. In the final steps (not shown on Figure 3.2), the aluminum layer was etched away using Aluminum etchant Type A from Transene, then the wire bonding was done directly to silicon, and a 160 nm conformal film of Al_2O_3 was deposited using ALD.

3.4 Fabrication Results

The described fabrication process was not the first choice. Initially, the layer of Al was intended as means to reduce substrate charging and prevent development of the "footing" or notching effect during the DRIE process. Due to variations in etch speed, some of the trenches are completed faster in the through-wafer etch. As a result, in completed areas without the metal film, the glass wafer gets charged and repels the accelerated ions which leads to the lateral etch of the sidewalls [61]. However, it was quickly recognized that suspended high aspect ratio features could not quickly draw off heat produced from both the high energy plasma and exothermic chemical reaction. As a result, those features heated

up and locally disturbed the normal flow of the DRIE etch. High temperatures are very detrimental to the quality of the etch as they accelerate the etch rate of masking materials (e.g. photoresist) and silicon (Figure 3.3), as well as throw off the etch selectivity. Normally, the helium cooling keeps the wafer from overheating; however, the glass substrate wafer does not transfer heat as well as silicon which makes cooling less efficient. On top of that, the features suspended by long and slender flexures can overheat locally due to very narrow pathways to release excess heat [63]. Some of the features that had consistent gaps and aspect ratios that were not too high came out relatively well (Figure 3.6).

The sealed shallow trenches were introduced to deposit the metal layer away from the silicon-glass interface where it could obstruct the proper anodic bond. In addition, the trenches allow for creating suspended features that do not require a post-manufacturing release (e.g. hydrofluoric acid wet etch). The local overheating of such features is alleviated by the metal film and a slower etching process. Even though this side effect is reported in the literature, its impact was underestimated initially, which resulted in practically completely destroyed features (Figure 3.3).

Many additional challenges existed in the fabrication process. Cleanliness of the processed wafers before anodic bonding was very important, and multiple cleaning steps were required. Several wafers did not end up bonding properly. In addition, the anodic bonding placed limitations on the previous process steps due to high temperatures; no photoresist or other organic materials could be present. The Al layer also presented multiple challenges. Small residual patches of Al ultimately shorted out the motors if not etched perfectly and

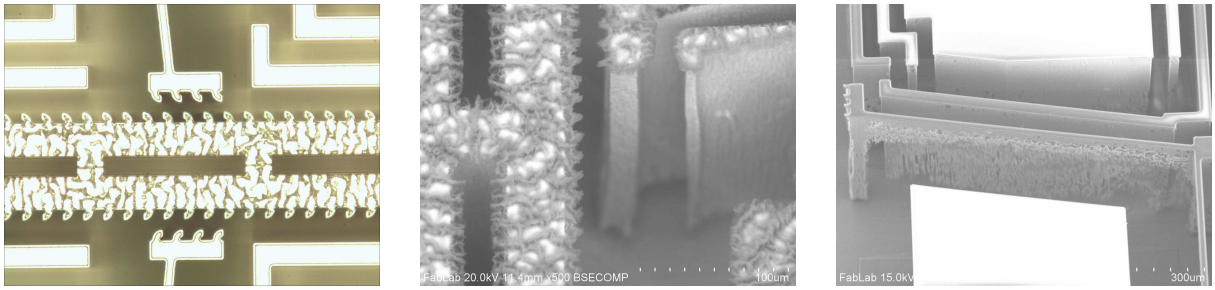

Figure 3.3: Results of overheating the suspended features during DRIE

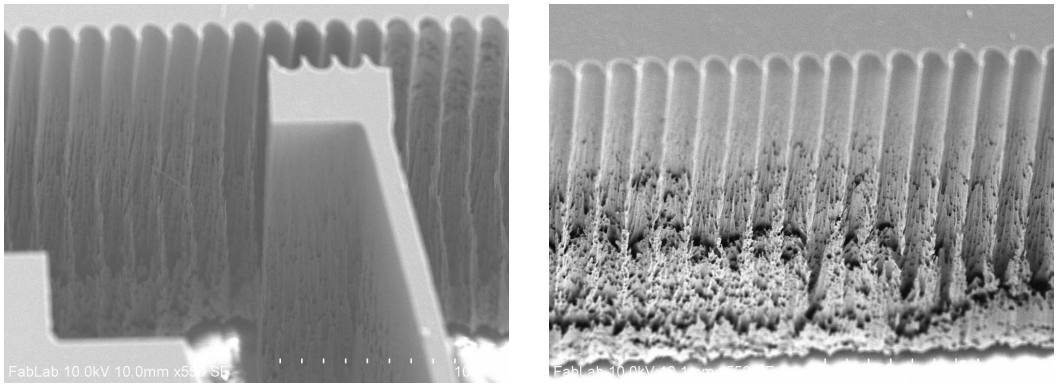

Figure 3.4: Peculiarities of the through wafer DRIE

oxidation of the Al surface ultimately resulted in very long etches or interchanging the Al etch with BHF.

A primary bottleneck in the design was the distance between the flexible arm and the shuttle (teeth contact). DRIE loading effects mean that the smallest gaps etch the slowest. Due to the long etch required by this small gap, considerable footing was found after the etch (Figure 3.5). Other odd effects of the long etch were found as shown in Figure 3.4. The cause of these peculiarities is still unclear.

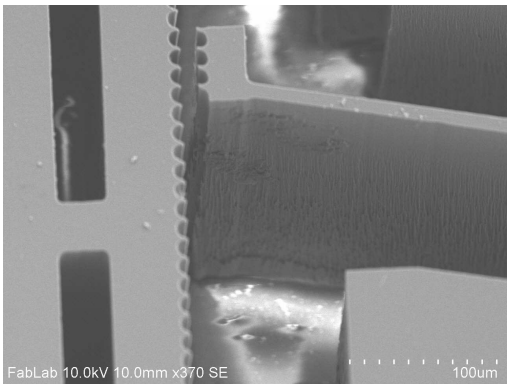

Figure 3.5: Bottleneck - gap between teeth

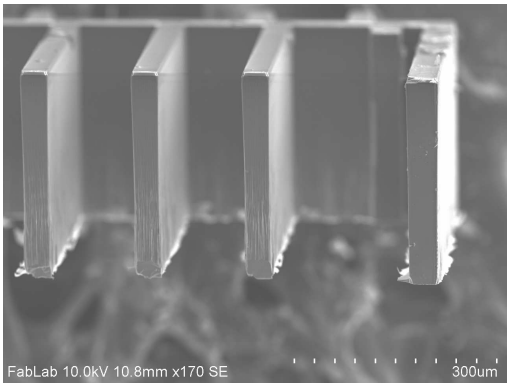

Figure 3.6: Better results of DRIE

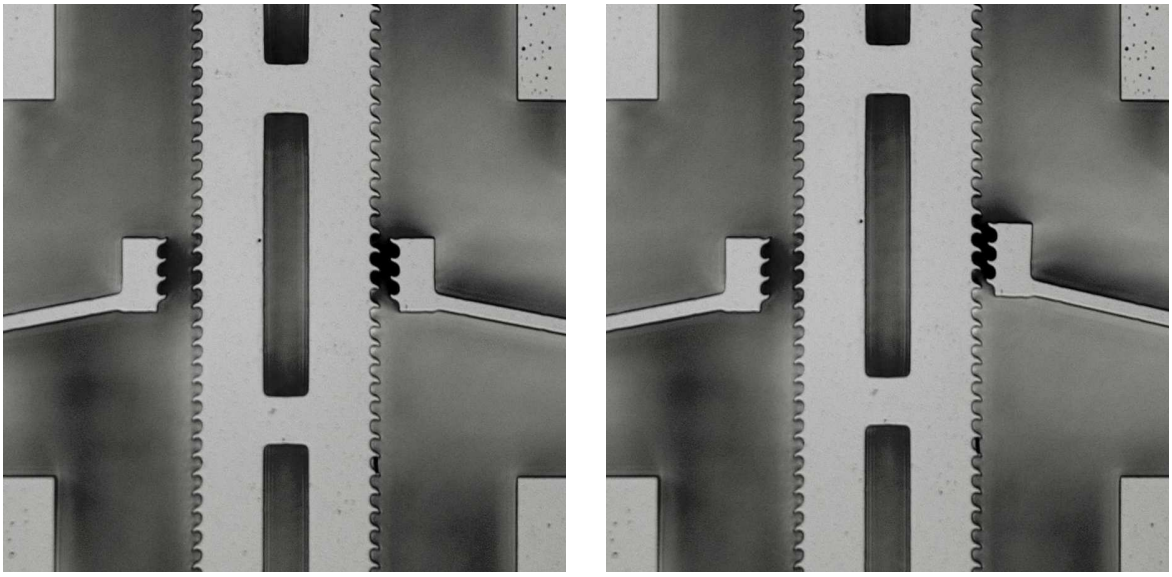

Figure 3.7: Through wafer motor shuttle movement without teeth engagement

3.5 Testing Results

In the end, several variations of the thick film motors were manufactured. Unfortunately, all of them suffered from issues with the manufacturing process. The actuators in the best variation (Figure 3.7) were able to move, but not push the shuttle due to footing between the teeth contact. Therefore, no force measurements were taken and the results provided in Table 3.1 were not confirmed.

3.6 Conclusions

Overall, it was clear that while it is attractive to simply increase the thickness of the film used to create the motor, this approach has numerous fabrication challenges. Further recipe iterations or improved tools could potentially alleviate some of these challenges, and

the approach has promise given the advantage of increased force and greater robustness. However, a decision was made to pursue the second approach toward increasing force – reducing the engagement gap by allowing compliance and zipping in the actuators. First, however, it was important to develop some new characterization methods to quantify force output in motor. This characterization method is described in Chapter 4.

Chapter 4

Characterizing electrostatic actuators with electrical measurements

4.1 Introduction

The characterization of the SOI motors in Chapter 2 was limited in the variety and accuracy of obtainable data. The only directly measured data from actuators was displacement as a function of voltage, whereas forces were calculated using the calibrated spring flexure values. The calibration was done using the capacitance measurements from several comb drives that were included on the wafer for that purpose. Furthermore, the majority of measurements were done only in the static equilibrium state.

In this work, we consider the actuator as more than a mechanical system with forces and displacements, and instead model it as an electrical device with two resistors (R_{ser} and R_{par}) and a variable capacitor $C_{\text{x}}(x)$ (Figure 4.1). Here, R_{ser} represents resistance of the connection wires and electrodes themselves, R_{par} represents the parasitic resistance (ionized air, substrate, etc) that allows for leakage current across the capacitor, and $C_{\text{x}}(x)$ symbolizes the inter-electrode capacitance of the actuator.

With this approach, numerous techniques that exist to characterize electrical devices can be used to evaluate electrostatic actuators. The primary goals of these methods were to allow for dynamic/transient measurements, improve measurement accuracy, and also offer

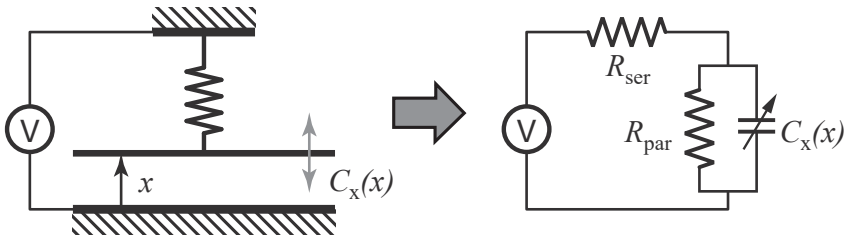

Figure 4.1: Electrical model of the electrostatic actuator . In this case, an electrostatic gap closing actuator is shown.

concomitant methods to verify results. All of the experiments can be divided into two major groups — electrical and electromechanical — depending on the utilized measurement techniques.

Electrical characterization In the first group of tests, the actuators were modeled as linear electrical systems with a known circuit (Figure 4.1) but unknown values. Actuators' electrodes were assumed to be fixed and therefore capacitance C_x was constant for the duration of each test. Motion between tests or displacements much slower (quasistatic) than electrical signals do not violate this assumption.

The electrical response of the described circuit depends only on magnitude and frequency of the input signal. The values of unknown circuit elements were identified from the measured frequency response of the actuators. The amplitude of voltage inputs during all *electrical* characterization tests was kept low to minimize mechanical motion, satisfy the assumption of fixed electrodes, and prevent nonlinear behavior. Voltage signals were measured and recorded in all *electrical* characterization tests. Some tests also included displacement measurements via optical microscope. The gathered data was then analyzed and used to validate the modeling and to calculate the actuators' me-

chanical properties. For example, force characteristics was calculated directly from the varying capacitance of electrostatic actuators.

Electromechanical characterization In the second set of experiments, the mechanical motion was unrestricted and occurred on a similar time scale as the input electrical signals. Considering coupling between mechanical and electrical domains (variable capacitance) and highly nonlinear motion of the actuator during tests, analytical analysis of the model becomes too complicated and inaccurate. *Electromechanical* characterization was mostly experimental and focused on transient and dynamic behavior of the actuators. The electric circuitry and corresponding measurements remained the same as in *electrical* characterization. In addition, several experiments included actuator force and displacement measurements.

The gathered data was used to compare with the estimated force characteristics from electrical tests, measure the approximate efficiency of the actuators, and verify actuators' electromechanical model. This method is used in Chapter 5.

4.2 Electrical model of electrostatic actuators and test setup

Measurement and identification of unknown electrical parameters is common practice but several factors complicate the use of these techniques in electrostatic actuators. Most importantly, the measurements have to be done during operation (*in situ*) with working voltages exceeding 150 V. To address this challenge and measure the parameters of interest for both *electrical* and *electromechanical* characterization, the actuators (or DUTs – devices

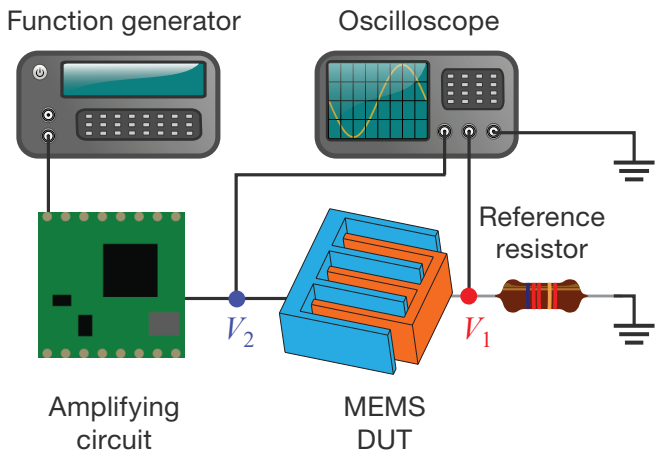

Figure 4.2: Electrical setup in electrostatic actuators characterization tests

under test) were connected into a measurement circuit (Figure 4.2) that also included a reference sensing resistor, a high voltage power source (or amplifying circuit), an oscilloscope (MDO4054-3 from Tektronix), and a function generator (AFG3022C from Tektronix).

Electrical measurements in all characterization tests followed the same pattern. Amplified signal from the function generator actuated the DUT. Oscilloscope recorded both amplified voltage (V_2 in Figure 4.2) and voltage across the reference resistor (V_1 in Figure 4.2). Analysis and comparison of the measured signals V_1 and V_2 allowed to obtain normalized DUT responses: normalized frequency response for *electrical* characterization tests and normalized magnitude transient response for *electromechanical* characterization tests.

To identify actuator model parameters (C_x and R_par) from the measured response, the entire system including both the actuator and the electrical test setup (Figure 4.2) was simplified and modeled as a linear electrical circuit with only a few relevant components

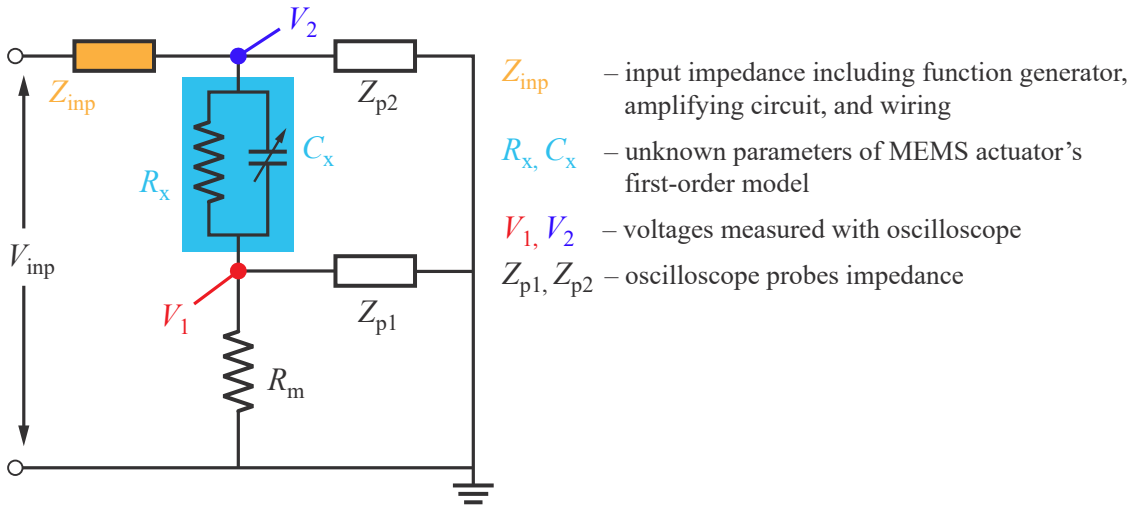

Figure 4.3: Electrical diagram of the electrical measurement setup

(Figure 4.3). Here, Z_{inp} represents the generalized input impedance of the amplifying circuit, function generator, and other circuit components (or effects) that occur before measurement point V_2 in Figure 4.3. V_{inp} symbolizes the expected output voltage from the amplifying circuit. Z_{p1} and Z_{p2} represent the oscilloscope probes that were used to measure voltages V_1 and V_2 respectively. Oscilloscope probes are designed with a compensation circuit for which the impedance is accurately known. The total impedance of the probes used in this work was a parallel RC circuit where $C_p = 4.7\,\text{pF}$ and $R_p = 10\,\text{M}\Omega$. R_m represents a reference passive resistor; the value of this resistor can be adjusted to maximize the measurement sensitivity as described in Section 4.3.3. Finally, the MEMS DUT was represented by the model in Figure 4.1 with the exception of R_{ser}. Preliminary tests showed that its impact was insignificant and the value was impossible to identify reliably due to its large magnitude and specifics of the actuator's frequency response. R_{ser} added an extra degree of freedom in the model identification which substantially increased uncertainty in the other parameters.

The model in Figure 4.3 assumes that input voltage during actuating and measurement uses frequencies that are low enough to neglect inductance effects. Also, some practical issues can not be represented in the model. For example, grounded objects near the DUT added parasitic capacitance to ground, which in turn decreased the measured voltage V_1. As an anecdotal example, the signal V_1 would change depending on the used magnification of the microscope; each objective lens had a different length thereby changing the objective's distance to the DUT along with the parasitic capacitance to ground. These un-modeled effects were minimized as much as possible by using the same test setup so that results between actuators can be effectively compared. However, there can still be an impact on the absolute values of the results.

One of the defining aspects of *electrical* characterization tests is decoupling between electrical and mechanical domains. This requirement places restriction on actuators' motion and assumes their capacitance C_{x} to be constant during the tests. Then, a closer look at the circuit model shows that in the case of sinusoidal excitation, the ratio of measured voltages V_1/V_2 in steady state is independent of the input voltage impedance Z_{inp}. The only components that affect the voltage ratio are the reference resistance (R_{m}) impedances of the

oscilloscope probes (Z_{p1}, Z_{p2}), and the DUT itself:

$$\begin{cases} Z_p = R_p \parallel C_p \\ Z_x = R_x \parallel C_x \\ Z_{eq} = Z_p \parallel R_m = R_p \parallel C_p \parallel R_m \\ Z_{tot} = Z_{eq} + Z_x = R_p \parallel C_p \parallel R_m + R_x \parallel C_x \end{cases} \tag{4.1}$$

$$H = \frac{V_1}{V_2} = \frac{Z_{eq}}{Z_{tot}} = \frac{Z_p R_m}{Z_x(Z_p + R_m) + Z_p R_m} \tag{4.2}$$

where H is the linear time-invariant transfer function, $Z_p = R_p/(1 + j\omega R_p C_p)$ is the impedance of the oscilloscope probes, $Z_x = R_x/(1 + j\omega R_x C_x)$ is the DUT's impedance, R_m is the *a priori* chosen reference resistor, and ω is the excitation voltage frequency.

After replacing impedance values with their expressions, the transfer function (4.2) becomes

$$H(j\omega) = \frac{R_m R_p(1 + j\omega R_x C_x)}{(R_x R_p + R_x R_m + R_p R_m) + j\omega R_m R_x R_p(C_x + C_p)}, \tag{4.3}$$

which is a linear first order system (1 pole and 1 zero). It can be represented in a traditional (zero-pole-gain) form

$$H(s) = K\frac{s + z_1}{s + p_1} \tag{4.4}$$

where gain $K = \dfrac{C_x}{C_x + C_p}$, zero $z_1 = -\dfrac{1}{R_x C_x}$, and pole $p_1 = -\dfrac{R_x R_p + R_x R_m + R_p R_m}{R_m R_x R_p(C_x + C_p)}$.

Table 4.1 lists an initial estimation of circuit model parameters based on use of an SOI wafer with a 40 µm and typical actuator dimensions from Table 5.2).

Several observations can be made about the expected frequency response from analysis

Table 4.1: Circuit parameters

Probe impedance (known)	DUT impedance (estimated)	Reference resistor (known)
$R_\mathrm{p} = 10\,\mathrm{M\Omega}$ $C_\mathrm{p} = 4.7\,\mathrm{pF}$	$R_\mathrm{x} > 5\,\mathrm{M\Omega}$ $C_\mathrm{x} \approx (1 \ldots 30)\,\mathrm{pF}$	$R_\mathrm{m} \approx (1 \ldots 100)\,\mathrm{k\Omega}$

of (4.4) and the values in Table 4.1:

1. the system performs as a passive first-order high-pass filter;

2. the low frequency (DC) response is $H(0) = \frac{R_\mathrm{m} R_\mathrm{p}}{R_\mathrm{x} R_\mathrm{p} + R_\mathrm{x} R_\mathrm{m} + R_\mathrm{p} R_\mathrm{m}}$, and with the estimated parameters above $H(0) \approx \frac{R_\mathrm{m}}{R_\mathrm{x}} \approx (1 \ldots 100) \cdot 10^{-3}$;

3. the high frequency response $H(\infty) = K = \frac{C_\mathrm{x}}{C_\mathrm{x} + C_\mathrm{p}}$, and with the estimated parameters above $H(\infty) = K = \frac{C_\mathrm{x}}{C_\mathrm{x} + C_\mathrm{p}} \lessapprox 0.8$;

4. the zero, $-z_1 \lessapprox 1000\,\mathrm{rad/s}$;

5. the pole, $-p_1 \approx \frac{1}{R_\mathrm{m}(C_\mathrm{x} + C_\mathrm{p})} \approx (0.4 \ldots 166) \cdot 10^6\,\mathrm{rad/s}$;

6. considering that the zero z_1 and pole p_1 are several orders of magnitude apart, their mutual interference is rather limited. z_1 depends only on the parameters of the DUT and not the circuit. R_x substantially influences the zero but not the pole (and its impact can be neglected if R_m is sufficiently small).

An expected frequency response of the modeled system (Figure 4.3) is represented in Figure 4.4. The response is exemplary of a passive, first-order, high-pass filter.

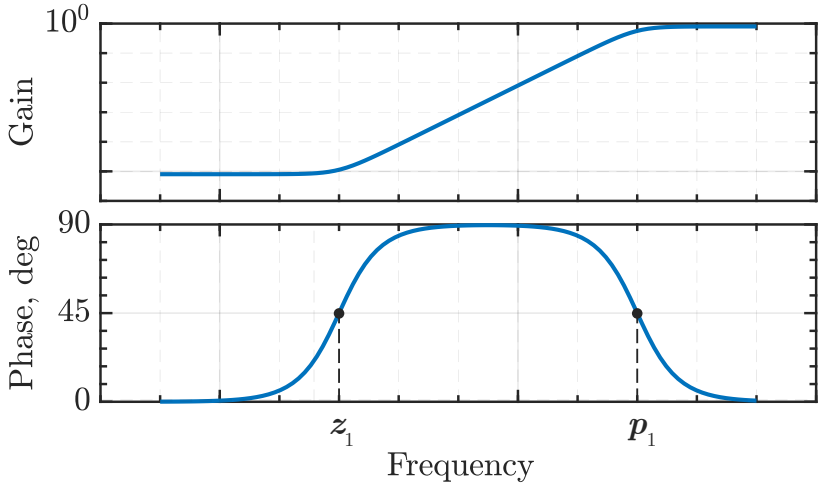

Figure 4.4: Expected frequency response of the modeled system assuming constant DUT capacitance (fixed actuator)

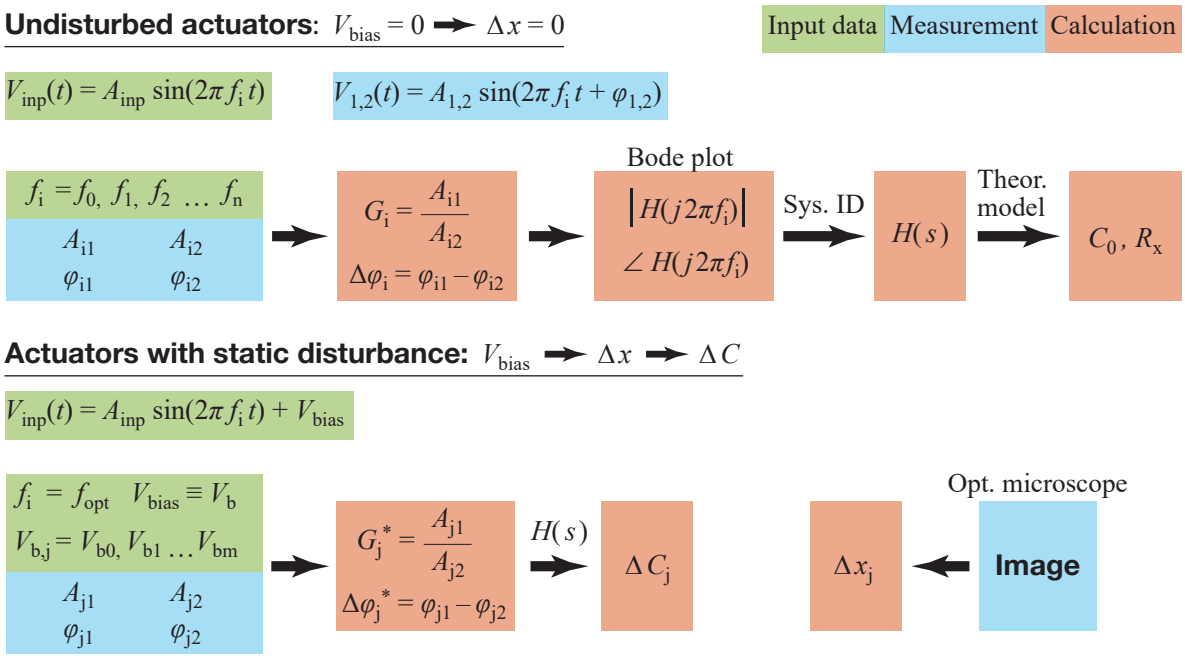

Figure 4.5: Sequence of steps for the *electrical* characterization with manual stepwise sweep

4.3 Electrical Characterization: Actuator Parameters Identification

The *electrical* characterization pursued several distinct goals:

1. verification of the theoretical model;
2. identification of the model parameters (C_{x} and R_{x}) for the undisturbed actuators;
3. measurement of the change in actuator capacitance throughout its range of motion (quasistatic displacement) along with corresponding movement distance.

The first two objectives were achieved by measuring frequency response of actuators at the initial state (undisturbed) and matching the result with the derived transfer function (4.4). For the third objective, a DC bias was applied to the actuators to quasistatically shift the interdigitated electrodes within their range of motion. All steps for this characterization procedure can be summarized as:

(i) obtain frequency response of an unactuated DUT in the expected bandwidth of interest;

(ii) verify DUT's electrical model and calculate R_{par} and $C_0 \equiv C_{\mathrm{x}=0}$ from the measured frequency response;

(iii) quasistatically actuate DUT by applying small DC bias;

(iv) measure DUT's response with the applied DC bias;

(v) measure displacement of the actuator using optical microscope;

(vi) Use DUT's electrical model to calculate change in capacitance considering that other parameters in the actuator model are independent of DC bias and electrode movement.

(vii) Further actuate DUT by increasing DC bias and obtain new capacitance value. Repeat these steps throughout DUT's range of motion.

These steps are schematically represented in Figure 4.5.

As part of the parameter identification process, there are several choices and optimizations that can be made to reduce noise, improve sensitivity, or speed up the data collection. For example, choice of actuator input (type of excitation signal) can reduce time to compute the frequency response whereas an appropriate choice for R_{m} can improve the measurements sensitivity.

4.3.1 Actuator Input

The actuator input during characterization tests was produced by the function generator and then passed through the amplifying circuit (Figure 4.2) to attain the required amplitude. The entire input circuitry and its signal are represented by Z_{inp} and V_{inp} in the electrical diagram (Figure 4.3). The function generator was controlled from a desktop PC using Matlab software. This allowed for easy and quick composition of different input signals to obtain various system responses, generally trading off speed of data collection for noise reduction.

A manual stepwise sweep was the first input used to measure the actuator's frequency response (Figure 4.6a). The measurements were done in 50 logarithmically spaced frequencies distributed in the bandwidth of interest (10 kHz to 1 MHz). At each frequency a sinusoidal excitation voltage with constant amplitude was applied to the system. Both V_1 and V_2 voltages were recorded. The measured signals were analyzed by fitting them into a sinusoidal waveform to determine their amplitude and phase.

These results were then used to calculate the actuator's frequency response (gain and phase difference) and match it with the derived transfer function (Figure 4.5). Use of a manual stepwise sweep resulted in a frequency response with little noise, but took significant time to complete. The measurement noise was a function of frequency, being the largest in the kHz range due to attenuation of the measured voltage V_1.

A linear sine sweep (or linear chirp) was the second input used to measure the DUT's frequency response (Figure 4.6b). Frequency of the sine signal swept linearly the desired range (10 kHz to 1 MHz) within a short time interval while maintaining other parameters constant. Similarly to the stepwise sweep, the sine sweep input started in the function generator and then was amplified. However, for this input only one test was needed to obtain actuator's frequency response. After each test, the recorded input and output signals were processed in Matlab's System Identification toolbox to obtain the transfer function with 1 pole, 1 zero, and a gain. The main advantage of this method over the manual stepwise sweep was a shorter acquisition time and faster data analysis. Essentially, the sine sweep input provided a shortcut to the system ID step in Figure 4.5.

4.3.2 Quality of the measurements

The measured frequency response $H = V_1/V_2$ depends entirely on circuit parameters as shown in (4.4). However, only few of them can be deliberately selected before the experiments – V_2, R_m. To increase accuracy and sensitivity of the measurements these values should be

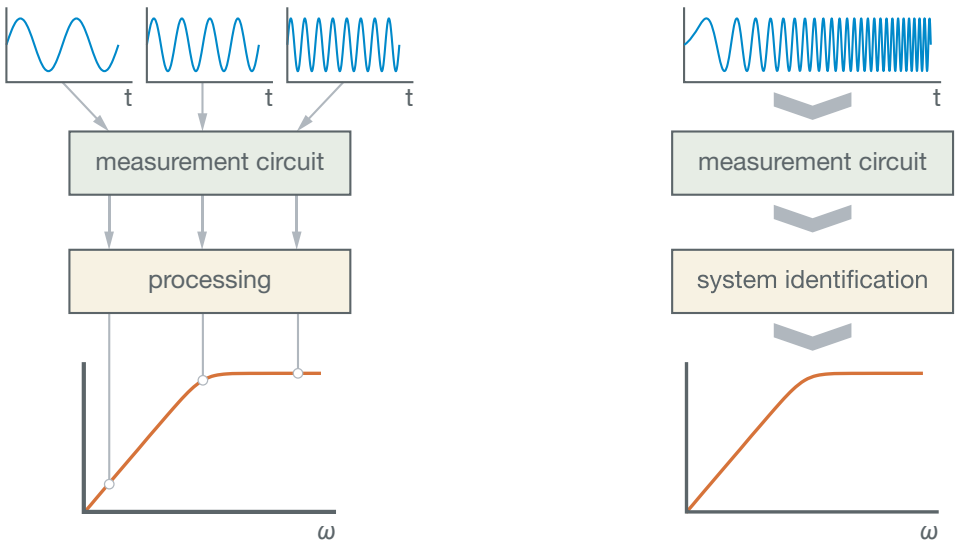

(a) Manual stepwise sweep (b) Linear sine sweep

Figure 4.6: Figure demonstrating two different test methods: a manual stepwise sweep and a linear sine sweep

chosen optimally.

Sensitivity of the measurements was defined as a ratio of change in the measured response to a corresponding variation in DUT's capacitance ($\Delta H/\Delta C_{\mathrm{x}}$). It is expected that the circuit's output is nonlinear and therefore the sensitivity is not constant. Maximizing it in the measured frequency range will benefit the measurement's quality. Next, the amplitude of measured voltage V_1 is expected to be much smaller than of V_2 (especially at lower frequencies) since the circuit acts as a high-pass filter. If the attenuation values are too high, measurements of V_1 will be erroneous and dominated by noise, therefore leading to inaccurate calculated values of H and ultimately C_{x}. Thus, the quality measurements can only be expected if the minimum magnitude of the measured output signal exceeds a certain

level. These conditions for optimum measurements can be summarized as

$$\begin{cases} \max\limits_{R_\mathrm{m}} \dfrac{\Delta H}{\Delta C_\mathrm{x}} \; \forall \omega \in [10\,\mathrm{kHz},\, 1\,\mathrm{MHz}] \\ |V_1(\omega,\, R_\mathrm{m})| > V_\mathrm{min} \end{cases} \Rightarrow \begin{cases} \max\limits_{R_\mathrm{m}} \dfrac{dH}{dC_\mathrm{x}} \; \forall \omega \in [10\,\mathrm{kHz},\, 1\,\mathrm{MHz}] \\ |H(\omega,\, R_\mathrm{m})| > H_\mathrm{min}, \text{ if } |V_2| - \text{const } \forall\, \omega, \end{cases} \tag{4.5}$$

where V_min is the smallest empirically established level of measured voltage that ensures consistent, high confidence fitting of data onto the sinusoidal waveform during post analysis.

The amplitude of V_2 could not be increased arbitrarily since only quasistatic motion of actuators is allowed during *electrical* characterization tests. The maximum amplitude for V_2 across all of the *electrical* characterization tests was set to 1 V. This was a conservative estimate because displacement of actuators varied depending on their type (Table 5.2).

Evaluation of expressions (4.5) can be facilitated by reorganizing (4.3)

$$H(s) = \frac{1 + sR_\mathrm{x}C_\mathrm{x}}{1 + \kappa + sR_\mathrm{x}(C_\mathrm{x} + C_\mathrm{p})}, \text{ then} \tag{4.6}$$

$$\frac{dH}{dC_\mathrm{x}} = \frac{sR_\mathrm{x}(\kappa + sR_\mathrm{x}C_\mathrm{p})}{(1 + \kappa + sR_\mathrm{x}(C_\mathrm{x} + C_\mathrm{p}))^2}, \tag{4.7}$$

where $s = j\omega$ and $\kappa = \frac{R_\mathrm{x}}{R_\mathrm{m}} \frac{R_\mathrm{p}+R_\mathrm{m}}{R_\mathrm{p}}$. Since H and dH/dC_x are complex functions, the L2-norms (magnitudes) of these functions were used for maximum search. Magnitudes of expressions

(4.6) and (4.7) are

$$|H| = \frac{\sqrt{C_\mathrm{x}^2 R_\mathrm{x}^2 \omega^2 + 1}}{\sqrt{R_\mathrm{x}^2 \omega^2 (C_\mathrm{p} + C_\mathrm{x})^2 + (\kappa + 1)^2}} \tag{4.8}$$

$$\left|\frac{dH}{dC_\mathrm{x}}\right| = \frac{R_\mathrm{x}\omega\sqrt{C_\mathrm{p}^2 R_\mathrm{x}^2 \omega^2 + \kappa^2}}{R_\mathrm{x}^2 \omega^2 (C_\mathrm{p} + C_\mathrm{x})^2 + (\kappa + 1)^2} \tag{4.9}$$

4.3.3 Constraints on the reference resistor R_m value

Analysis of the theoretical frequency response from the measurement circuit showed that sufficiently low values of R_m decouple zero and pole of the system and drastically decrease impact of R_x and R_p on the DUT response. This simplifies processing of the results and improves quality of the measurements. This condition basically ensures that impedance of the measurement tool (oscilloscope probes) is significantly higher than the measured load – R_m.

At the same time, small values of R_m shift measurement circuit pole towards higher frequency range. This becomes an issue when the pole moves outside of the testing circuit's bandwidth. Then, the inflection point on the frequency response plot disappears and the system identification becomes inaccurate and unstable. Considering these aspects and mechanical resonance frequencies of DUTs, the conservative constraints for R_m were stated as:

(i) $R_\mathrm{m} \leq 0.01 R_\mathrm{x}$ and $R_\mathrm{m} \leq 0.01 R_\mathrm{p}$ (impedance constraint);

(ii) $\max p_1 = -5 \cdot 2\pi \cdot 10\,\mathrm{kHz} \approx -314 \cdot 10^3$ rad/s, where 10 kHz is estimated mechanical resonance of actuators and 5 is a conservative coefficient;

(iii) $\min p_1 = -2\pi \cdot 1\,\text{MHz} \approx -6.28 \cdot 10^6$ rad/s, where 1 MHz is the maximum operational range of the measurement test circuit.

These constraints were combined with the simplified equation for the system pole ($-p_1 \approx 1/R_\text{m}(C_\text{x}+C_\text{p})$) and estimated range for the total capacitance $C_\text{x}+C_\text{p} \approx (5\ldots35)\,\text{pF}$. Then, after rearrangement for R_m:

$$\begin{cases} R_\text{m} \leq 50\,\text{k}\Omega \\ R_\text{m} \leq 640\,\text{k}\Omega \text{ for } \min(C_\text{x}+C_\text{p});\ R_\text{m} \leq 91\,\text{k}\Omega \text{ for } \max(C_\text{x}+C_\text{p}) \\ R_\text{m} \geq 32\,\text{k}\Omega \text{ for } \min(C_\text{x}+C_\text{p});\ R_\text{m} \geq 4.6\,\text{k}\Omega \text{ for } \max(C_\text{x}+C_\text{p}) \end{cases} \tag{4.10}$$

To satisfy all constraints from (4.10), the reference resistor has to be within range $(32\ldots50)\,\text{k}\Omega$. The value used in the test circuit was chosen to be $46.9\,\text{k}\Omega$.

4.3.4 Choice of ω for tests with DC bias

The manual stepwise sweep is relatively time consuming and was implemented to obtain a full frequency response of the unactuated motors. After verification of the theoretical model and obtaining the transfer function, sweeping the entire bandwidth is unnecessary and too time intensive for monitoring changes in actuator's capacitance. Frequency response at only one of the frequencies is enough to calculate modified capacitance using the obtained transfer function. However, it is important to choose a frequency that will still allow good quality of the measurements. This section focuses on the choice of frequency used during tests with DC bias to maximize measurement sensitivity.

Given the constraints in (4.5), an optimal frequency ω_opt can be found from the zero

derivative requirement

$$\frac{d}{d\omega}\left(\left|\frac{dH}{dC_\mathrm{x}}\right|\right)=0 \quad \Rightarrow \quad \omega_\mathrm{opt}=\frac{\kappa(\kappa+1)}{R_\mathrm{x}\sqrt{\kappa^2(C_\mathrm{p}+C_\mathrm{x})^2-2C_\mathrm{p}^2(\kappa+1)^2}}, \text{ given that} \tag{4.11}$$

$$\left(\frac{C_\mathrm{x}+C_\mathrm{p}}{C_\mathrm{p}}\right)^2>2\left(\frac{\kappa+1}{\kappa}\right)^2. \tag{4.12}$$

These expressions can be simplified, considering the estimated values for circuit parameters discussed above (Table 4.1) and chosen value for the reference resistor (4.3.3).

$$\begin{gathered} R_\mathrm{p}\gg R_\mathrm{m} \quad \Rightarrow \quad \kappa=\frac{R_\mathrm{x}}{R_\mathrm{m}}\frac{R_\mathrm{p}+R_\mathrm{m}}{R_\mathrm{p}}\approx\frac{R_\mathrm{x}}{R_\mathrm{m}} \\ R_\mathrm{x}\gg R_\mathrm{m} \quad \Rightarrow \quad \kappa\gg 1 \quad \Rightarrow \quad \kappa+1\approx\kappa \end{gathered} \tag{4.13}$$

$$\omega_\mathrm{opt}\approx\frac{1}{R_\mathrm{m}}\frac{1}{\sqrt{C_\mathrm{x}^2+2C_\mathrm{x}C_\mathrm{p}-C_\mathrm{p}^2}}=\frac{1}{R_\mathrm{m}C_\mathrm{p}}\frac{1}{\sqrt{\alpha^2+2\alpha-1}}\equiv\omega_\mathrm{opt}^*, \tag{4.14}$$

where $\alpha={}^{C_\mathrm{x}}/_{C_\mathrm{p}}$. Also, the requirement (4.12) becomes $\alpha^2+2\alpha-1>0$ thus $\alpha>\sqrt{2}-1$ and $C_\mathrm{x}>(\sqrt{2}-1)C_\mathrm{p}\approx 0.41C_\mathrm{p}$. This is a requirement at which the optimum frequency exists; if it is violated, the sensitivity monotonically increases with the frequency (dH/dC_x asymptotically approaches a maximum value which is not explicitly defined).

The circuit's sensitivity to the capacitance change dH/dC_x (4.9) at the optimum frequency becomes

$$S_\mathrm{H}\equiv\left|\frac{dH}{dC_\mathrm{x}}\right|_{\omega\,\to\,\omega_\mathrm{opt}^*}=\frac{1}{2\sqrt{C_\mathrm{x}^2+2C_\mathrm{x}C_\mathrm{p}}}=\frac{1}{2C_\mathrm{p}\sqrt{\alpha^2+2\alpha}}. \tag{4.15}$$

This expression is independent of R_m, R_x, and R_p which is the result of the approximation

in (4.14). The derived expression demonstrates that the optimized sensitivity is inversely proportional to the measured capacitance C_x which is a limiting factor in the accuracy of measurements. Also, (4.15) highlights the detrimental impact of any parasitic capacitance.

The magnitude of the circuit's transfer function H (4.8) at the optimum frequency becomes

$$|H|_{\omega \to \omega^*_{\mathrm{opt}}} \approx \frac{\sqrt{1+\frac{\alpha^2\kappa^2}{\alpha^2+2\alpha-1}}}{\sqrt{\kappa^2+\kappa^2\frac{(1+\alpha)^2}{\alpha^2+2\alpha-1}}} \approx \frac{1}{\kappa}\sqrt{\frac{\kappa^2\alpha^2+2\alpha-1}{2\alpha^2+4\alpha}} \approx \sqrt{\frac{\alpha}{2\alpha+4}} \tag{4.16}$$

The circuit's sensitivity in (4.15) assumes that the optimum measurement frequency (4.14) is used for each unknown capacitance C_x. This is clearly impossible to achieve in practical realization. Realistically only one frequency needs to be chosen for the entire range of C_x (Table 4.1).

Figure 4.7 demonstrates comparison between best case scenario (ω^*_{opt} for every C_x) and two frequencies that are optimal to opposite ends of the estimated C_x range: 100 kHz works for max C_x, and 1000 kHz works for min C_x. Circuit sensitivity at 1000 kHz is significantly higher for the lower end of measured capacitance but it very quickly drops off. The 100 kHz sensitivity stays relatively constant throughout the entire range of C_x. However, the magnitude of the response at 100 kHz is alarmingly low, especially for small C_x.

Several different strategies can be adopted for rationalizing the selection of ω: to maximize the highest dH/dC_x, to maximize the smallest dH/dC_x, to maximize the average dH/dC_x over the entire range of expected C_x, and so on. Here, the first approach was implemented since the high values of C_x are achievable only at the very last stages of actuator

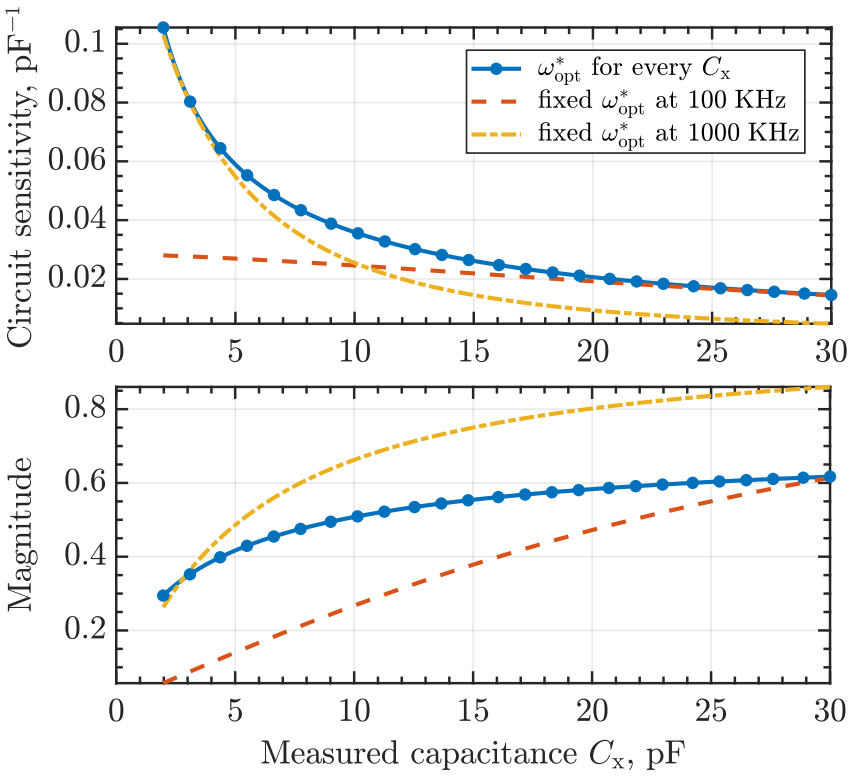

Figure 4.7: Comparison of theoretical sensitivity dH/dC_x and magnitude of H for various measurement frequencies ω

motion and, therefore, are less meaningful. To validate the model and analysis, each DUT and each DC bias value were tested on three frequencies: 800 kHz, 900 kHz, and 1000 kHz (Figure 4.8).

The range of capacitances used in Figure 4.7 was estimated based on actuators' design (Table 5.2). The calculated value for $\min C_x$ was under 1 pF and expected $\max C_x$ exceeded 30 pF.

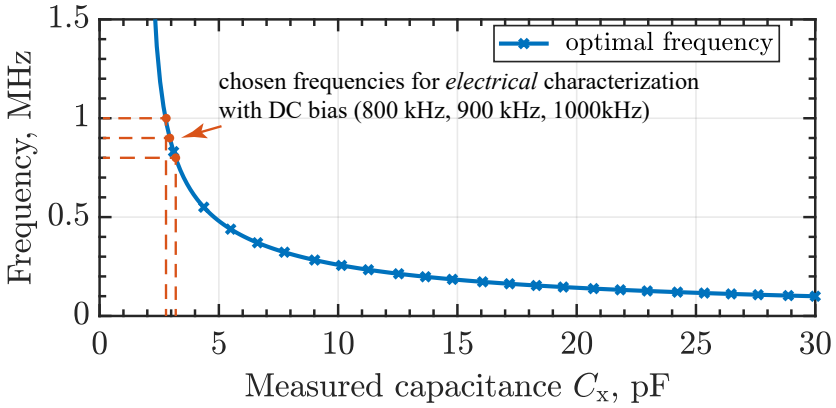

Figure 4.8: Optimal measurement frequency ω^*_{opt} as a function of measured capacitance C_x. Calculated using (4.14), model parameters from Table 4.1 and $R_m = 46.9\,\text{k}\Omega$

4.4 Experimental setup and characterization

To validate this characterization method, an experimental test setup was built as shown in Figure 4.2. The reference resistor was chosen as described in Section 4.3.3, a function generator (AFG3022C from Tektronix) was used to provide the inputs described in Section 4.3.1, and was controlled from MATLAB. An oscilloscope (MDO4054-3 from Tektronix) was used to measure voltages V_1 and V_2. The amplifying circuit was a custom design and is described below, along with validation of the test setup with fixed resistors and capacitors, and the selection of actuators used for testing.

4.4.1 High Voltage Amplifying Circuit

In addition to the time varying nature of the function generator inputs, high voltages are also required for this characterization. A previous high voltage amplifying circuit used in the tests with SOI motors from Chapter 2 [20, 64] had several limitations that made it

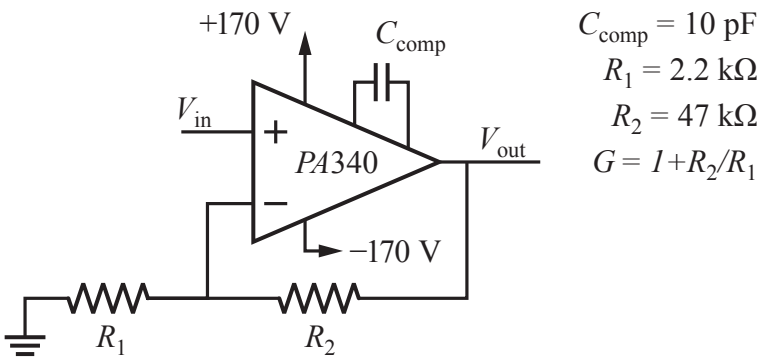

Figure 4.9: High voltage amplifier for electrical tests

inapplicable for the new tests. For instance, the voltage discretization had only 8-bit resolution in the entire range (0 V to 250 V) which made it impossible to create the continuous waveforms described above. Also, the bandwidth of the previous power amplifier (HV256 from Microchip) limited the actuating frequencies to 5 kHz. Finally, the previous power amplifier was designed to generate a signal at only one polarity. With some electrostatic actuators (e.g. zipping actuators), dielectric charging issues arise so both positive and negative voltages are required. Previous studies with capacitive actuators required switching the actuation voltage polarity to ensure their continuous and repeatable operation [65].

For the electrical characterization tests, a new amplifying circuit was designed with special attention to high bandwidth and dual-polarity capabilities. This circuit used a non-inverting amplifier configuration (Figure 4.9) based on a MOSFET amplifier (Apex, PA340 [66, 67]).

To confirm the required bandwidth, the new amplifier circuit was characterized using a manual stepwise sweep to measure its frequency response (Figure 4.10). The measured gain is nearly constant under 100 kHz but drops by 3 dB at 500 kHz and by 7 dB at 1000 kHz. The

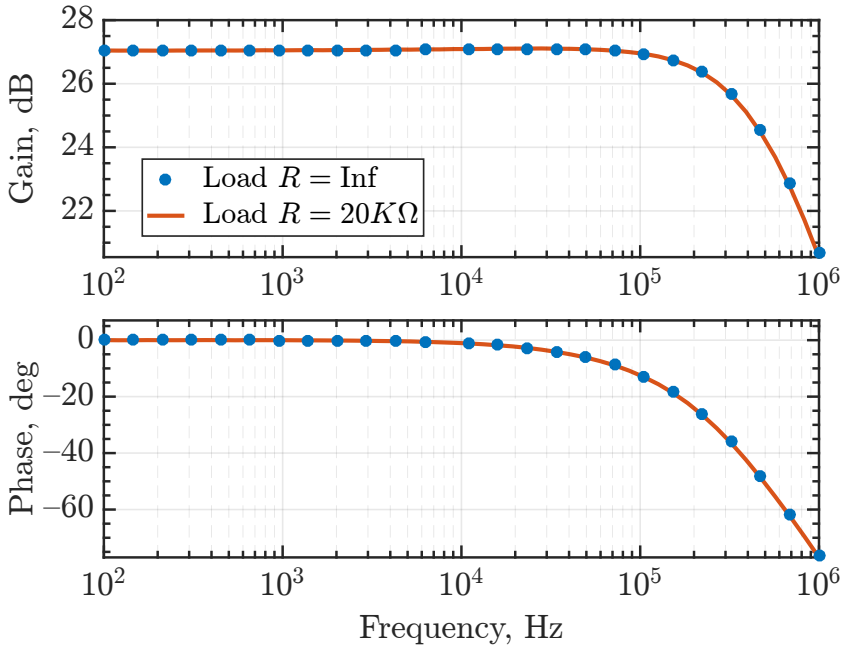

Figure 4.10: Amplifying circuit: frequency response. Note that both curves represent measured data. Only a subset of the data points for $R = \text{Inf}$ are included for clarity

magnitude response (Figure 4.11) shows high linearity over a large range of voltages. These results demonstrate that the assembled amplifying circuit based on the PA340 amplifier is capable of high bandwidth (up to 1 MHz) and voltage (> 100 V) tests on the electrostatic actuators. However, frequencies above 100 kHz can be utilized only with compensation for the gain drop off and phase shift. For this reason, the frequency response in characterization tests is measured with respect to the output from the amplifier and not from the function generator.

The measured frequency response with infinite load (open circuit) and with 20 kΩ load are nearly identical which indicates that the output is not sensitive to increases in load. Therefore the amplified voltage is expected to be the same when applied to a DUT.

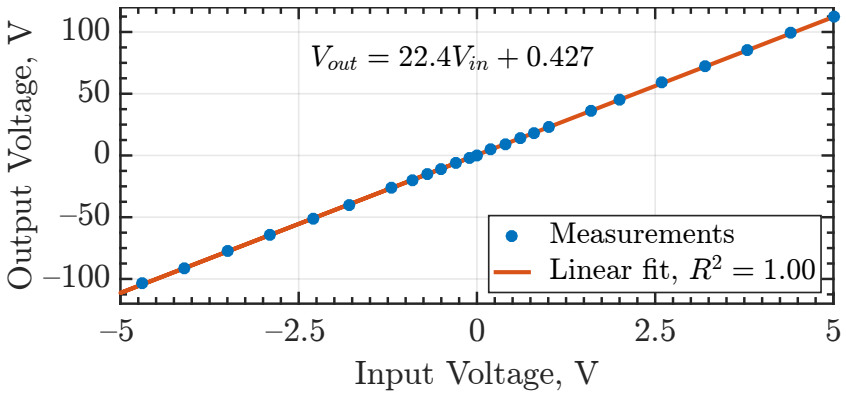

Figure 4.11: Amplifying circuit: comparison of input and output voltage magnitudes

4.4.2 Measurement Circuit

The measurement side of the experimental setup described in Figure 4.2 and the corresponding circuit in Figure 4.3 is composed of a mixed domain oscilloscope (MDO4054-3 from Tektronix) and a reference resistor, R_{m}, connected to the electrostatic actuator (MEMS DUT). Similarly to the function generator, the oscilloscope is connected to and controlled from a desktop PC using MATLAB. This allowed streamlining arbitrary/compound waveform generation and results collection for a large number of tests.

Usually, similar tests are performed using a lock-in amplifier (as in [68]). However due to limitations in available equipment, a mixed domain oscilloscope was used. To improve the signal-to-noise ratio and accuracy in the *electrical* characterization tests, both measured signals (V_1 and V_2) were averaged over 64 samples using an internal oscilloscope algorithm, and at least 10 periods were recorded for data analysis. This was possible since the circuit was in the state of dynamic equilibrium and actuators performed as linear systems. Internal oscillators of the function generator and the oscilloscope were synchronized to ensure output

frequency stability and to prevent signal floating.

Averaging of the signal to improve quality of the measurements could not be implemented in the *electromechanical* characterization tests due to highly dynamic movement of the actuators which prevents any type of equilibrium from taking place.

4.4.3 Experimental Setup Validation

To validate the experimental setup without an embedded actuator and explore the tradeoffs between using the manual stepwise and linear sine sweep inputs, several preliminary tests were performed with surface mount resistors and capacitors of known values substituting for the actuator model R_x and C_x. The main goal of these tests was to verify the measurement concept, evaluate the affect of parasitic elements, and estimate the accuracy of measurements.

The characterization tests used zero DC offset with the harmonic excitation, equivalent to future actuators under test in an initial (not actuated) position. All major steps of this procedure are demonstrated in Figure 4.5, top part. As discussed in Section 4.3.1, the frequency response was measured in 50 logarithmically spaced frequencies between 10 kHz and 1 MHz.

Validation of the experimental setup and system identification (ID) methods was performed individually with all of the following components:

1. surface mount capacitors to sweep C_x: $C_0 = 8\,\text{pF}$, $10\,\text{pF}$ and $12\,\text{pF}$, $R_0 = \text{inf}$;

2. surface mount resistors to sweep R_x: $R_0 = 56.0\,\text{k}\Omega$, $99.8\,\text{k}\Omega$, $220\,\text{k}\Omega$ and $1000\,\text{k}\Omega$, $C_0 = \text{inf}$; This test was done mostly for reference and general interest since system ID

could not be applied to the results.

3. infinite load (open circuit), to evaluate parasitic capacitance: $C_0 = \text{inf}$, $R_0 = \text{inf}$.

Measured frequency responses for each of these tests are presented below in Figures 4.12 – 4.14 and the resulting identified parameters for the transfer function in (4.4) (zero, pole, and gain) calculated using Matlab's System Identification toolbox are provided in Tables 4.2 – 4.4. Both gain and phase data was used in the identification calculations. A fit percentage is included to demonstrate how well the system modeled with these parameters matches the measured data. These tables also include the identified parasitic capacitance C_p and device parameters, C_x and R_x calculated from the zero, pole, and gain terms. It is important to note that the resistors used were $\pm 1\%$ accuracy and the capacitors were $\pm 5\%$, however their values were verified using 4.5 digit multimeter (Agilent U1253B).

Multiple tests showed that the best system identification results were achieved for slightly different values of C_p from the expected oscilloscope probe values. Since the measurement circuit model did not contain an explicit parasitic capacitance element (and it was certainly present in the physical setup), it was decided to use the best fit value for C_p as a method to compensate for unaccounted capacitance (the best fit C_p value varied in the tests but was around 6 pF versus the expected 4.7 pF from the probes alone).

The second method of obtaining DUT's transfer function used linear sine sweep in the range between 10 kHz and 3 MHz as the input signal instead of harmonic wave at a single frequency. A typical example of measured voltage signals in sine sweep tests is demonstrated in Figure 4.15; data was obtained from a comb drive actuator ($w2\ r81\ cd5.0n4$). The entire

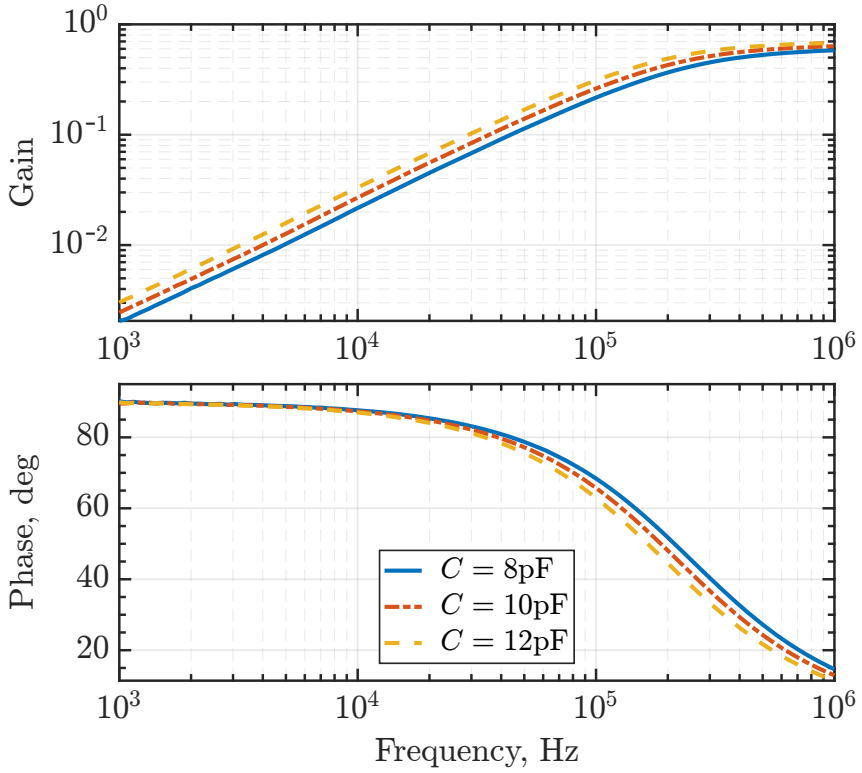

Figure 4.12: Measurement system validation, SMD capacitor as DUT

Table 4.2: Results of system ID for system validation with SMD capacitor as DUT

Zero	**Pole**	**Gain**	**Fit (%)**	$\boldsymbol{R_x}$ (MΩ)	$\boldsymbol{C_p}$ (pF)	$\boldsymbol{C_x}$ (pF)	$\boldsymbol{C_0}$ (pF)
$-2.18 \cdot 10^3$	$-1.62 \cdot 10^6$	$5.96 \cdot 10^{-1}$	99.3	57.9	5.36	7.91	8
$-2.00 \cdot 10^3$	$-1.42 \cdot 10^6$	$6.45 \cdot 10^{-1}$	99.3	51.3	5.38	9.76	10
$-1.71 \cdot 10^3$	$-1.25 \cdot 10^6$	$6.89 \cdot 10^{-1}$	99.4	49.3	5.35	11.8	12

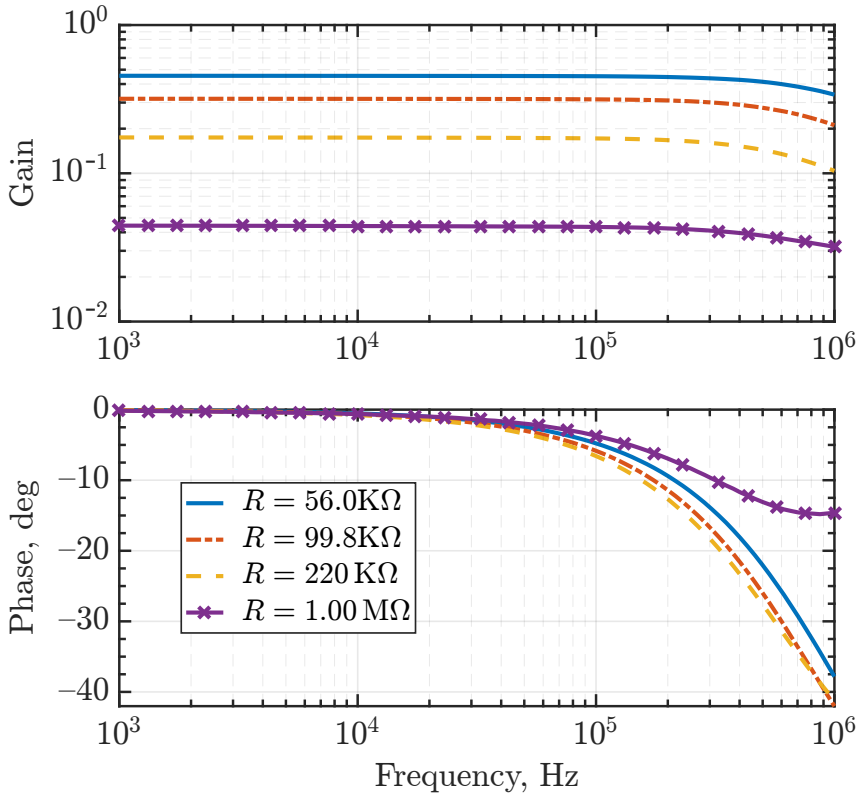

Figure 4.13: Measurement system validation, SMD resistor as DUT (included for reference only)

Table 4.3: Results of system ID for system validation with SMD resistor as DUT (included for reference only)

Zero	**Pole**	**Gain**	**Fit (%)**	$\boldsymbol{C_p}$ (pF)	$\boldsymbol{C_x}$ (pF)	$\boldsymbol{R_0}$ (kΩ)
$-8.30 \cdot 10^7$	$-6.97 \cdot 10^6$	$3.81 \cdot 10^{-2}$	99.1	5.42	0.215	56.0
$-5.20 \cdot 10^7$	$-5.54 \cdot 10^6$	$3.38 \cdot 10^{-2}$	99.2	5.48	0.193	99.8
$-2.53 \cdot 10^7$	$-4.50 \cdot 10^6$	$3.09 \cdot 10^{-2}$	98.5	5.59	0.180	221
$-6.40 \cdot 10^6$	$-3.82 \cdot 10^6$	$2.63 \cdot 10^{-2}$	95.2	5.71	0.156	1010

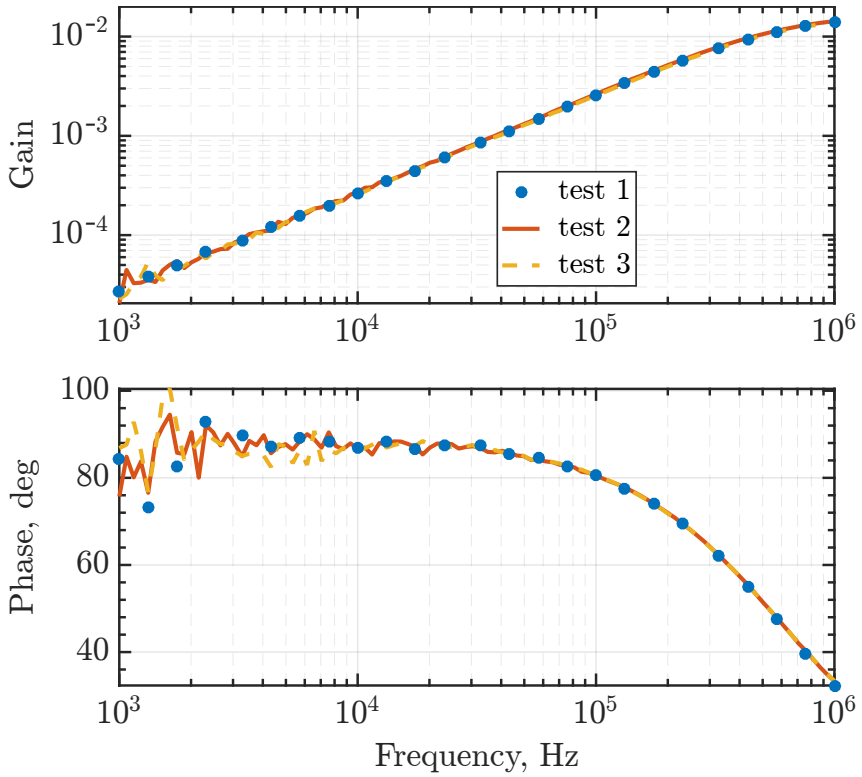

Figure 4.14: Measurement system validation, no DUT (open circuit)

Table 4.4: Results of system ID for system validation without DUT (open circuit)

Zero	**Pole**	**Gain**	**Fit (%)**	$\boldsymbol{R_x}$ (MΩ)	$\boldsymbol{C_p}$ (pF)	$\boldsymbol{C_x}$ (pF)
$-4.30 \cdot 10^3$	$-3.94 \cdot 10^6$	$1.66 \cdot 10^{-2}$	99.4	2580	5.35	$9.01 \cdot 10^{-2}$
$-5.02 \cdot 10^3$	$-3.99 \cdot 10^6$	$1.71 \cdot 10^{-2}$	98.8	2180	5.27	$9.15 \cdot 10^{-2}$
$-5.14 \cdot 10^3$	$-4.00 \cdot 10^6$	$1.65 \cdot 10^{-2}$	98.7	2200	5.27	$8.83 \cdot 10^{-2}$

frequency response and transfer function terms were calculated from the measured data using Matlab's System Identification toolbox. Simultaneous coverage of the entire bandwidth drastically reduced data sampling and processing time but at the expense of accuracy. To evaluate the extent of inaccuracies, several additional tests were conducted.

A comparison of frequency responses obtained from a comb drive actuator ($w2\ r81\ cd5.0n4$) using both a manual stepwise sweep and linear sine sweep is shown in Figure 4.16. While collecting data from the linear sine sweep is fast, this particular method suffers in accuracy at the lower frequencies due to lower gains and fewer cycles captured in that range, and unavailability of averaging the measured signal like in manual sweep tests. These resulting errors in system identification are described graphically in Figure 4.17 in comparison to corresponding values obtained in a manual stepwise sweep used as a reference given it's more accurate results. This figure includes data tests with varying parameters: total sweeping time, sampling frequency, and highest frequency.

Analysis shows that the gain (K) and pole (p_1) terms of the transfer function (4.4) deviate within few percent from the corresponding values obtained in manual stepwise sweep (represented by the blue dots at zero). The transfer function zero (z_1), on the other hand, showed large deviation and spread. This is a result of z_1 located in the lower frequency range where the measured transfer function was less reliable. Given the choice of R_{m} in Section 4.3.3, C_{x} and C_{p} can be determined using only transfer function pole (p_1) and gain (K), both of which demonstrate reproducible values and high accuracy. Moreover, error in the zero term primarily adds error to the estimate of R_{x}. Therefore, the linear sine sweep

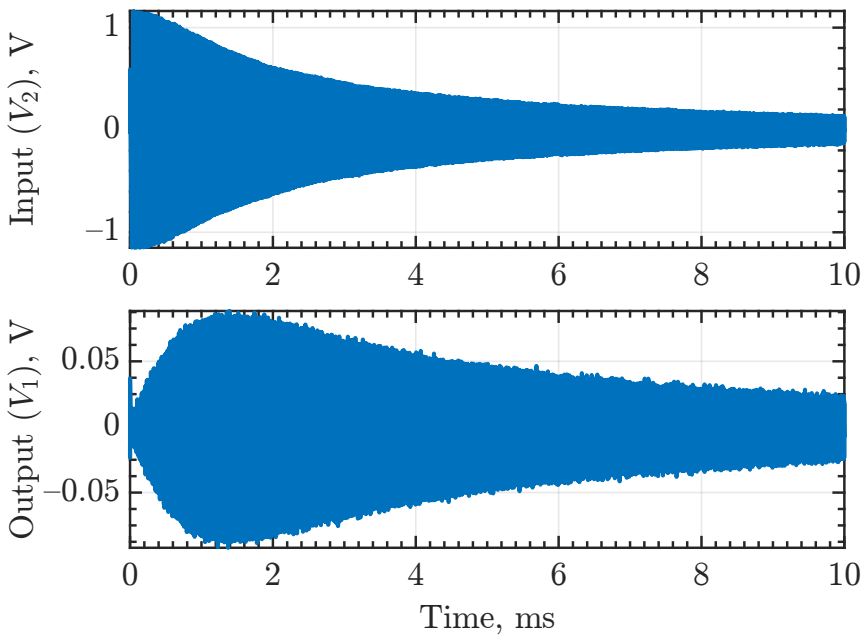

Figure 4.15: Example of measured input and output voltages in a linear sine sweep *electrical* characterization test. Data obtained from a comb drive actuator ($w2\ r81\ cd5.0n4$), frequency linearly changed from 10 kHz to 3 MHz within 10 ms

still resulted in an accurate estimate of C_x for electrostatic actuators

Validations tests showed that the developed transfer function (4.4) accurately describes the measured frequency response of both open circuit (no DUT, only parasitic elements) and SMD capacitors as DUTs. In the latter tests, capacitance C_x calculated from the measured frequency response deviated only several percent from the actual value of the used capacitors (Table 4.2). In addition, absolute values of DUT's capacitance are not as important and permit small inaccuracies in measurements, whereas change in capacitance of electrostatic actuators is essential since generated force is directly proportional to it. So as long as the measurement errors stay constant, they will cancel out and provide accurate measurement of the capacitance change. Since the measurement error of C_x does not vary significantly

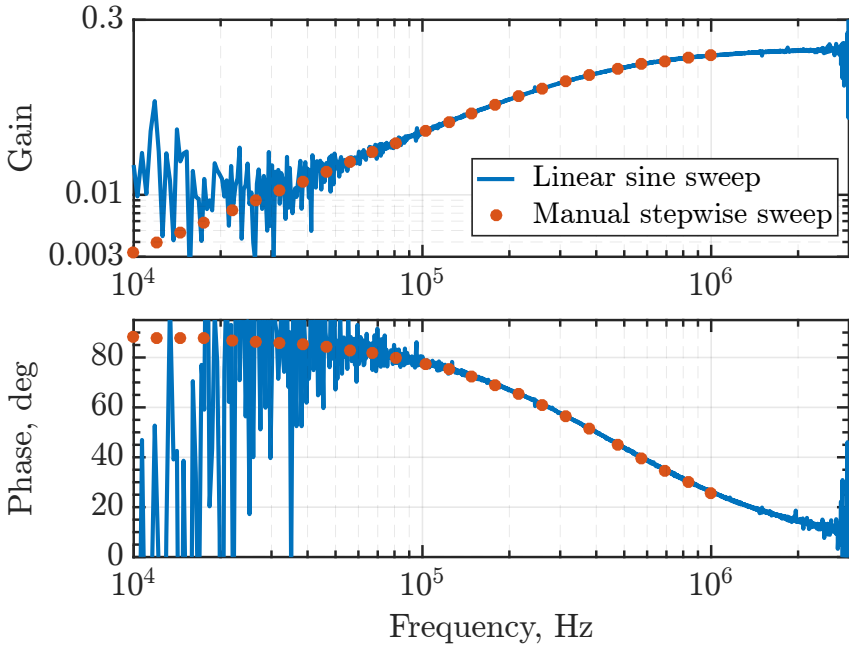

Figure 4.16: Comparison of frequency response of a comb drive actuator ($w2\ r81\ cd5.0n4$) obtained from manual and sine sweep methods

Figure 4.17: Deviation in transfer function constants calculated from linear sine and manual stepwise sweep.

for different values of SMD capacitors, the proposed measurement method was considered acceptable for further examination of the actuators.

4.4.4 Actuators under test

All characterization and validation tests above were done with zero DC bias and constant C_x. *Electrical* characterization tests on both comb drive and gap closing actuators were done with varying DC biases as described in Section 4.3. After processing all of measurements, each actuator had 3 sets of data that described its performance: a set of DC biases applied to the actuator and sets of corresponding displacement and capacitance of the actuator.

Both comb drive and gap closing actuators were fabricated on a silicon-on-insulator (SOI) wafer (40 µm structural layer, 2 µm oxide layer) using a standard SOI manufacturing process (as described in Section 2.3.1). The devices were transferred to the silicon layer in a single DRIE step. After the etch, the wafer was coated with photoresist to protect small gaps from particle contamination and diced. Then, the photoresist layer was ashed with oxygen plasma and devices were released by wet etching the buried oxide in 49 % hydrofluoric (HF) acid. No stiction of silicon features was observed during drying of devices due to the relatively thick structural and oxide layers. After drying, aluminum wires were bonded directly to the silicon pads. To prevent electrical shorting of the electrodes due to accidental contact during the tests, a 200 nm layer of aluminum oxide (Al_2O_3) was conformally deposited on the released structures using an atomic layer deposition (ALD) process [52].

Table 4.5: Manual and linear sine sweep calibration of a comb drive actuator ($w2\ r80\ cd6.2n2$ #5–#7)

Type	**Zero**	**Pole**	**Gain**	**Fit (%)**	$\boldsymbol{R_x}$ (MΩ)	$\boldsymbol{C_p}$ (pF)	$\boldsymbol{C_x}$ (pF)
manual	$-3.76 \cdot 10^3$	$-2.90 \cdot 10^6$	$1.59 \cdot 10^{-1}$	99.4	227	6.22	1.17
sweep	$-1.70 \cdot 10^4$	$-2.98 \cdot 10^6$	$1.61 \cdot 10^{-1}$	97.1	50.7	6.02	1.16

Comb drive actuators have the benefit of a linear capacitance change with displacement and relatively stable movement over a large range of applied DC biases. Gap closing actuators are often more challenging to characterize given the nonlinear force versus displacement characteristics and instability at displacements above one third the initial gap.

4.5 Results

All measurement and analysis steps in the following sections follow the procedure described in Section 4.3.

4.5.1 Comb drive actuators

To start, both manual stepwise and linear sine sweeps were performed on the comb drive actuators described above to measure frequency response and identify circuit parameters C_x, R_x, and parasitic capacitance C_p with zero DC bias. The results are presented in Table 4.5. Both methods show strong agreement on C_x. These results are not compared to an analytical result for C_x due to expected deviations from fabrication described in Chapter 2.

Applying a DC bias moves the comb drive, therefore changing the capacitance of the actuator. To minimize the time required to take measurements, only a single frequency was

used for each measurement of gain and phase at a given DC bias as described in Section 4.3.4. To validate results, *electrical* characterization procedure was done three times at different frequencies (800 kHz, 900 kHz, and 1000 kHz) for each of the tested actuators. Gain and phase measurements were then extracted from the measured data for each value of DC bias voltage (Figure 4.18), and capacitance was calculated from these measurements based on the full transfer function found using the linear sine sweep. Gain and phase measurements were used separately to calculate the actuator capacitance C_x in order to compare the efficacy of each measurement.

As shown in Figure 4.19, the capacitance identified using gain measurements is repeatable and reliable at all three excitation frequencies. Also, it matches the value of C_x at zero displacement (and zero DC bias) calculated from the frequency response (Table 4.5). The phase measurements overestimate capacitance and are likely more error prone due to inaccuracies in phase measurement.

Finally, the displacement of each comb drive at each DC bias was measured using photographs taken during the tests. Capacitance can then be plotted as a function of displacement as in Figure 4.19. Capacitance is expected to be a linear function of displacement as seen in Section 4.4.4. While this linear trend is seen at larger displacements from the experimental data, it is not linear at smaller displacements due to fringing fields from the ends of comb drive fingers [38]. Ultimately, actuator force can be computed using the slope of the capacitance curve in Figure 4.19 and the bias voltage squared.

A comparison of measurements taken from multiple comb drives is shown in Figure 4.20.

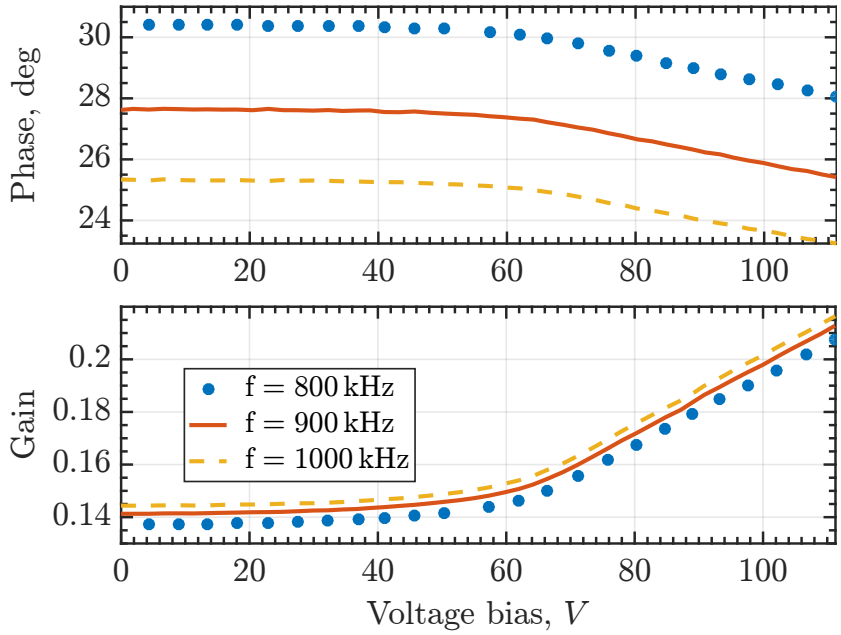

Figure 4.18: Example of change in phase and gain in quasi-static comb drive test (*electrical* characterization, $w2$ $r80$ $cd6.2n2$ #5–#7)

Four comb drives were measured including two different designs from two different wafers. Not surprisingly given design and fabrication variations, each had a slightly different initial capacitance and slopes which resulted in different forces. The expected square root dependence of bias voltage based on comb drive displacement is seen in the bottom half of Figure 4.20. For convenience capacitance in each curve was offset to start from zero. As mentioned previously, this step does not impact force calculation since it depends on the slope of capacitance curve and not absolute values.

4.5.2 Gap closing actuators

Gap closing actuators are more challenging to characterize based on their nonlinear capacitance versus displacement curves and their inherent instability when the displacement

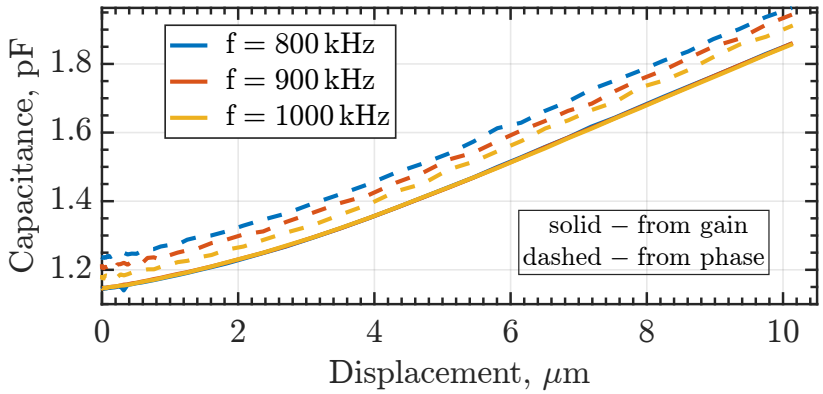

Figure 4.19: Change of comb drive's capacitance as a function of its displacement, comparison of phase and gain based calculations ($w2\ r80\ cd6.2n2$ #5–#7)

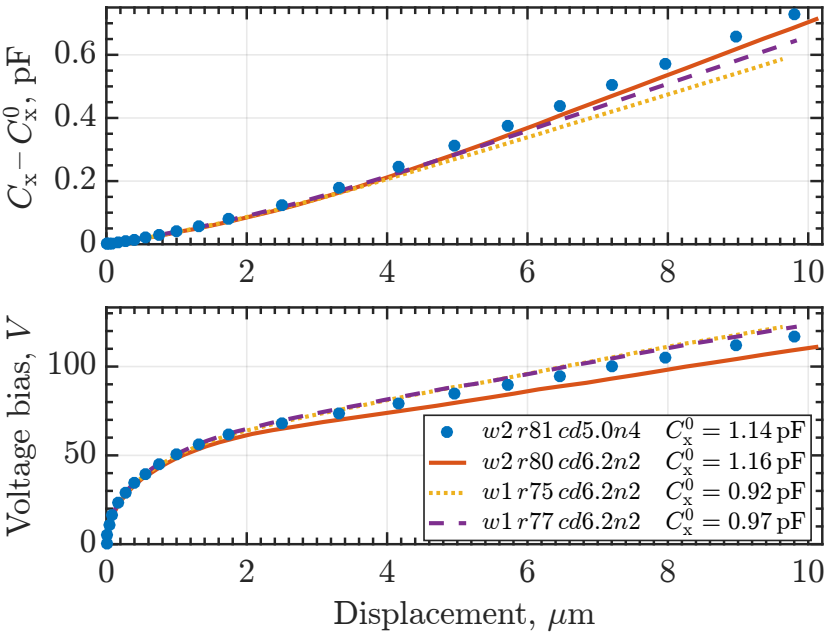

Figure 4.20: Comparison of capacitance change from several comb drives (*electrical* characterization, 2 wafers, 4 dies, 2 cd designs)

Table 4.6: Manual and linear sine sweep calibration of a gap closing actuator ($w2\ r81\ gc4sl3$-2 #3–#7)

Type	**Zero**	**Pole**	**Gain**	**Fit (%)**	$\boldsymbol{R_x}$ (MΩ)	$\boldsymbol{C_p}$ (pF)	$\boldsymbol{C_x}$ (pF)
manual	$-3.65 \cdot 10^3$	$-3.15 \cdot 10^6$	$1.06 \cdot 10^{-1}$	99.4	381	6.07	0.719
sweep	$-1.34 \cdot 10^4$	$-3.23 \cdot 10^6$	$1.06 \cdot 10^{-1}$	92.5	106	5.93	0.702

reaches one third the initial gap. However, the *electrical* characterization can be used to obtain capacitance curves and then calculate force versus displacement dependence, for these actuators as well. As with comb drives, both a manual stepwise and linear sine sweep were used to measure frequency response and calculate the initial capacitance of the gap closing actuator at zero displacement (Table 4.6). Both approaches resulted in approximately the same estimate for actuator capacitance.

For each gap closing actuator, *electrical* characterization procedure was done four times with different frequencies in contrast to the three used for the comb drive actuators: 700 kHz, 800 kHz, 900 kHz and 1000 kHz. An example of calculated gain and phase at each frequency varying with DC bias voltage (5 V... 110 V) is shown in Figure 4.21. Similarly to the comb drive example, the gain measurements were more consistent and ultimately led to more reliable capacitance measurements versus displacement as shown in Figure 4.22. The zero displacement capacitance C_x calculated from gain measurements matches those measured in Table 4.6. Figure 4.22 clearly shows the nonlinear dependence of capacitance on displacement in these actuators.

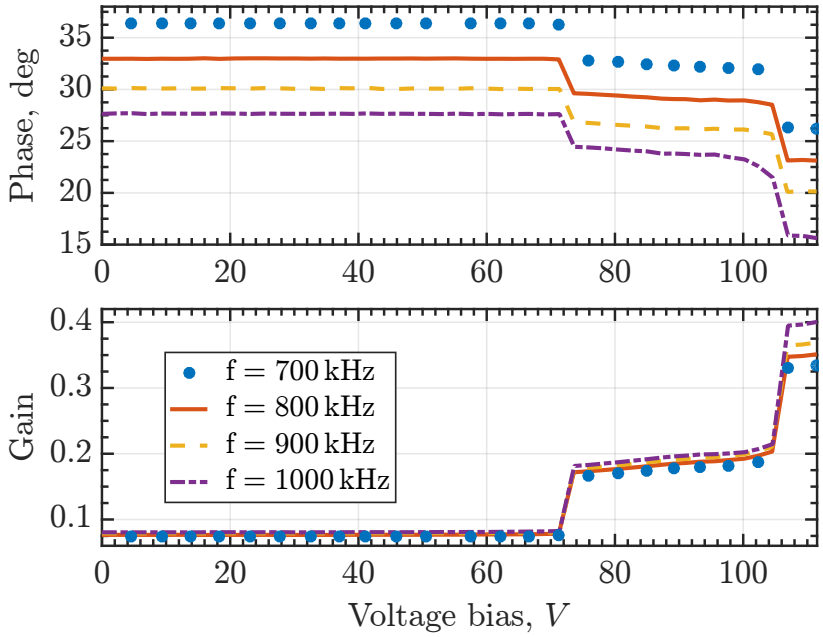

Figure 4.21: Example of change in phase and gain in quasi-static GCA test (*electrical* characterization, $w2$ $r81$ $gc5sl4$-*gap* #22–#25)

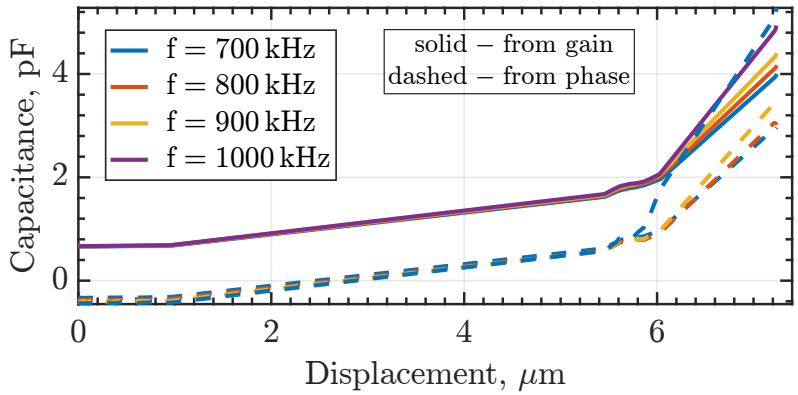

Figure 4.22: Change of GCA's capacitance as a function of its displacement, comparison of phase and gain based calculations ($w2$ $r81$ $gc5sl4$-*gap* #22–#25)

4.5.3 Comparison of various electrostatic actuators

To compare capability for force output between actuators, a comb drive actuator, gap closing actuator with rigid electrodes, and a zipping actuator (e.g., [69]) were all tested and results were plotted together in Figure 4.23. The top plot in this figure showing change in capacitance from its initial value (C_{x}^{0} listed for each actuator) versus displacement. These plots are very useful for comparison of mechanical and force characteristics of electrostatic actuators. It is evident what is the maximum displacement of each actuator and at what DC voltage bias it is achieved; what is the voltage required for producing noticeable movement and how does capacitance change at that stage stage (e.g. existence of fringing effects); is there a pull-in effect and at what voltage does it take place (jump in displacement at 50 V for $w1\ r75\ gc-rig$ and at 85 V for $w1\ r77\ gc5sl4-60$); is there any weird behavior like dielectric charging (visible in $w1\ r77\ gc5sl4-60$ curve on the bottom plot); and so on.

Moreover, it is extremely important that electrostatic forces can be estimated and compared from the capacitance curves (change of capacitance with displacement, top plot in Figure 4.23) since it is proportional to dC_{x}/dx. Basically, the higher the slope of the capacitance curve, the higher is the produced force. Then, it becomes evident that comb drive generates negligible force comparing to gap closing actuators. Rigid GCA has the highest slope (in the 5 µm area) but that force is produced over very small distance which makes it really hard to harvest in practice. Zipping GCA has lower slope (and force) but it is produced over longer distance (7 µm to 8 µm range). Note, electrostatic force is also proportional to the applied voltage squared. Considering that all these actuators are designed

to operate at the same maximum voltage level, for the purposes of fair comparison it is convenient to assume that applied voltage is always at maximum.

Force comparisons estimated using the slopes of capacitance curves in Figure 4.23 provides limited information and does not work in some cases. At first, due to pull-in effect in GCAs, the measurement points are available only in the beginning and end of the motion range. In the middle part, where actuator most likely starts transferring force, capacitance values could not be measured using quasistatic tests. Secondly, *electrical* characterization tests were done without any load or resistive forces applied to the actuator. When present, loads would either prevent actuators from completing their full range of motion or delay the displacement until applied DC bias generates force high enough to overcome resistance. In the latter case rigid GCAs would not change its original (no-load) capacitance curve. However, thinner electrodes in flexible or zipping GCAs can start bending if actuator stopped in the midpoint of its motion and electrostatic forces are high enough (described in Chapter 5). This would increase both capacitance and the attractive force, rendering estimates from no-load characterization tests invalid.

Therefore, slope of the no-load capacitance curves can not be used to characterize true maximum force for some of GCAs. Another possible benchmark for flexible and zipping GCAs can be the difference between maximum and initial capacitance assuming the same distance of force transfer. Capacitance difference is proportional to the energy increase in the capacitor and, thus, to the work done by the actuator. The actuator that does more work over the same distance will generate higher force. However, this or any other benchmarks

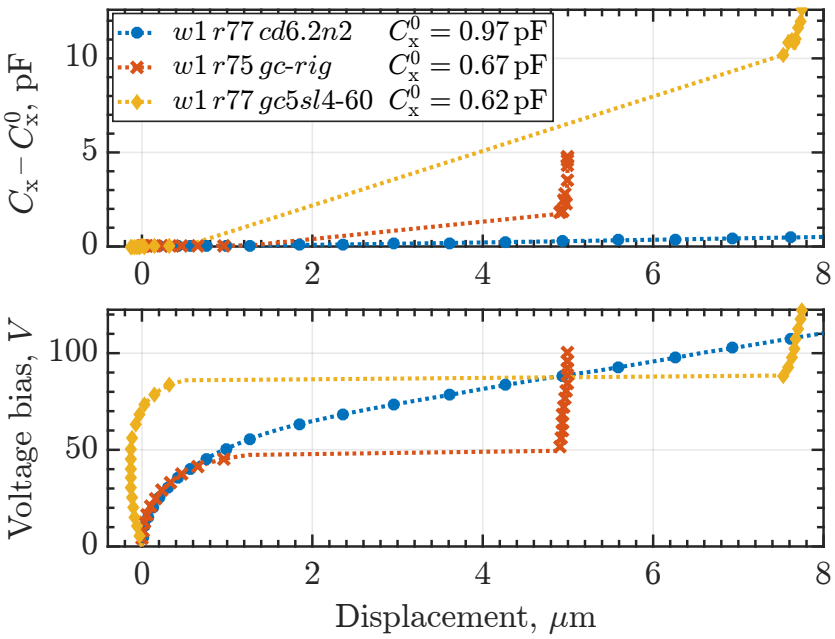

Figure 4.23: Comparison of quasi-static measurements from several electrostatic actuators (comb drive, rigid GCA, and zipping GCA)

calculated from quasistatic tests cannot account for nonlinear dynamic effects that take place in non rigid GCAs. Another characterization method that tries to tackle this issue is described in Chapter 6.

4.6 Conclusions

By identifying capacitance versus displacement using only electrical and photographic measurements, the technique presented in this chapter offers a fast and effective means of comparing force output between different types of electrostatic actuator. Measuring the change in actuator capacitance is a proxy measurement for actuator force, and is a far simpler measurement to make in comparison to the requirement for calibrated springs. This

technique was validated using surface mount resistors and capacitors as stand-ins for the electrostatic actuator and techniques to optimize the measurement frequency and reference resistor were presented. The results showed expected trends in capacitance for comb drives, gap-closing actuators, and zipping actuators, and were able to show expected phenomena like electrostatic pull-in quite clearly in gap-closing and zipping actuators.

Chapter 5

Increasing Force with Compliant Electrodes

5.1 Introduction

The highest calculated force for a thick film electrostatic motor in Chapter 3 using the optimization process in Chapter 2 was calculated to be roughly 20 mN (Table 3.1 for $MF = 7\,\mu m$). This value is equivalent to a 2 g mass which is a significant improvement for electrostatic motors in millirobotics had this process worked [37, 46, 70, 71]. However, even if the motors worked as designed, this force margin would have greatly limited the diversity of potential applications for these motors, even without considering the potential indirect force losses during usage. More useful forces are in the range of 10s to 100s of milliNewtons for microrobotic mechanisms [15].

Fortunately, there are several other potential design approaches to increase the resulting force to make these motors far more useful. Reducing the gap between electrodes in gap closing actuators and increasing the dielectric constant are two methods explored to increase force in this chapter.

5.2 Modeling Expected Force

As discussed in Section 2.3.3.2, the Al_2O_3 film protects the electrodes from electric shorting even during hard contact. Also, it was observed that at high voltages the electrodes were zipping together and closing the gap between them. This substantially increases the final force, however the effective force at engagement, F_{eng}, stays the same (Figure 2.9) because the zipping behavior occurs only after the motor begins acting on the load.

In previous designs, the electrode dimensions in the optimization process were chosen to minimize their bending and prevent contact when fully closed. Since experimental results have shown that this requirement is not necessary, designs can instead use more compliant electrodes to increase the engagement force. The electrostatic force can bend flexible interdigitated electrodes, pulling them closer together and further increasing the attractive force (Figure 5.1b). In this case, the parallel plate assumption is violated since the gap between electrodes is not constant, and the actuator force is calculated instead by,

$$F_{\text{g.-c.}} = \frac{1}{2}\int_0^L \frac{\varepsilon_r \varepsilon_0 t}{g(x)^2} V^2 \, dx. \tag{5.1}$$

As seen in Figure 5.1b, $g(x)$ is reduced at various points along the beam in comparison to the rigid electrodes in Figure 5.1a due to the electrode compliance, thereby increasing the overall force at the point of actuator engagement.

If electrodes are made even more compliant, the gap can be reduced further due to deflection of the electrode across the entire gap (Figure 5.1c). These electrodes will further

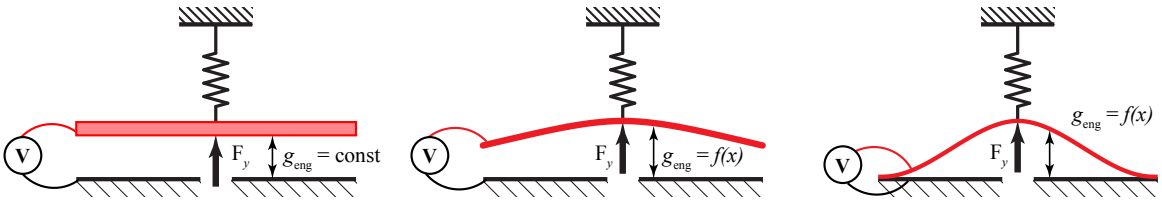

(a) Rigid electrodes (b) Compliant electrodes (c) Zipping electrodes

Figure 5.1: Effect of compliance on electrode shape

demonstrate zipping behavior after this initial contact as the gap collapses due to pull-in, and contact rapidly propagates along the interface/electrodes. This phenomenon occurs due to extremely high electrostatic forces that appear near the contact area (Figure 5.1c) where the interdigitated gap approaches zero. This geometry and behavior can be compared with a tip of a crack that propagates via closing instead of expanding. Zipping actuators have been previously analyzed [72, 73] and demonstrated to operate as optical and relay switches where large displacements are required [13, 74].

5.2.1 Compliant Electrodes

Both compliant (or flexible) and zipping electrodes promise to increase force in comparison to rigid electrodes due to a reduction in the engagement gap, g_{eng}. This gap is critical as it ultimately limits the engagement force, F_{eng}. Flexible electrodes are defined with an assumption of no physical contact between the surfaces before or after engagement – the flexible electrodes only bend. Upon finishing the stroke (effectively reaching g_{f}), the electrodes can make contact but this does not contribute to the useful force from the motor. Using this definition, the force from compliant electrodes can be directly calculated from

the static boundary value problem (BVP) of a cantilever beam bending by the electrostatic force,

$$\frac{d^2}{dx^2}\left(EJ\frac{d^2w(x)}{dx^2}\right) = F_{\text{g.-c.}} = \frac{1}{2}\int_0^L \frac{\varepsilon_r\varepsilon_0 t}{\left(g(x)-w(x)\right)^2}V^2\,dx,\ w(0)=0,\ w'(0)=0 \tag{5.2}$$

This equation shows good behavior until the voltage is increased enough to cause the pull-in instability. For higher voltages, the numerical solutions to this equation become highly unstable due to a singularity caused by a zero in the denominator. Even when a thin dielectric film is added in the model and the gap variable is limited by a non-zero lower boundary, the solution has large problems with convergence and the final result greatly depends on the tolerances and other procedural constants.

5.2.2 Zipping Electrodes

One method to model the geometry and forces of zipping electrodes was proposed by Li in [1] (Figure 5.2). This work treated the flexible electrode as a thin Euler beam, and the fixed electrode was considered to be absolutely rigid with a constant slope (the initial gap between electrodes increased linearly). This model utilized a quasi-static approach; only the initial (undisturbed) and final (zipped) states of the flexible beam were calculated, and the transient states as well as transition speed stayed unknown. The flexible beam in the final state was split into two parts: a zipped component (in continuous contact with the fixed electrode) and an unzipped component. The main goal of the solution was to calculate the transition point (L_s in Figure 5.2) between these parts. This was achieved by numerically

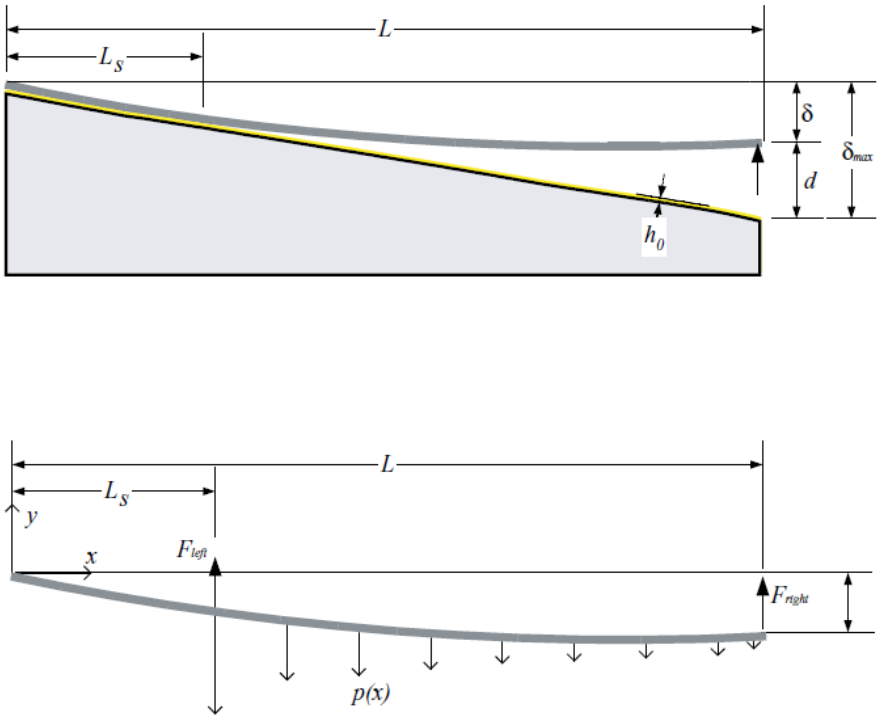

Figure 5.2: Model of zipping actuator from [1]

solving a parametric BVP problem in MATLAB. Once the displacement of the actuator tip was calculated using this approach, actuator engagement force was defined and calculated at the engagement gap similar to the methodology used for the compliant actuators in the previous section (5.2).

5.2.3 Force Comparison

The procedure and MATLAB script from [1] were used to calculate the engagement force from zipping electrodes, and force values for the compliant electrodes were calculated using (5.2). Both results are compared to rigid electrodes with the parameters provided in Table 5.1. For a fair comparison, the engagement gap between electrodes was made

equal and constant for all three cases. Thickness of the flexible beam (resulting in differing movable electrode compliance was the primary difference between three models, even though it resulted in drastically different outcomes. The zipping actuator was also made longer to further reduce compliance.

In these calculations and the following analysis, the displacement of the actuator's movable electrodes (both rigid and flexible) is defined by the gap connected to the point of force transfer through the flexible arm (Figure 5.1). This displacement is used to compare the gap at which the motor shuttle would normally be engaged, defined as g_{eng} in Table 5.1. However, it is important to note that the "real" (varying) distance across the length of the electrodes was used to analyze the force output of the actuator. This simplification was mainly a means to compare the actuator's performance since, ultimately, performance depends only on displacement and force transmitted through the flexible arm.

For a fair comparison, force per area (F_y/A) is provided for each actuator and defined as the force at the engagement gap (g_{eng}) divided by the areal footprint of the actuator. Based on this analysis with the chosen electrode parameters in Table 5.1, flexible electrodes almost double the expected areal force density of the actuators. Allowing the electrodes to zip results in an order of magnitude increase in predicted areal force density. This increase is due to the fact that the electrodes can be partially zipped when the motor engages and very high forces result from the small gaps in the partially zipped actuator.

Table 5.1: Comparison of engagement force generated by one electrode pair

	Rigid	Flexible	Zipping
w, µm	43	20	20
L, µm	500	500	600
g_{eng}, µm	3	3	3
F_{y}, mN	0.90	1.06	18.1
F_{y}/A, mN/mm^2	14.1	25.8	368

5.2.3.1 Shape of the Fixed Electrode

Based on this analysis, zipping actuation is worth further study due to the order of magnitude increase in actuator force. The analysis above assumed a compliant zipping electrode and a constant initial gap between electrodes (flat rigid electrode) Figure 5.1c. However, parallel electrodes are not required. Next, the effect of the fixed electrode shape (slope) on the force-gap relationship was estimated. Force calculations were done using the same MATLAB script from [1] with linearly sloped rigid and straight flexible electrodes (Figure 5.3), where s is the related to the linear slope of the inter-electrode gap (s is the maximum additional gap between electrodes, $s = 0$ corresponds to a flat rigid electrode) and g_1 is the minimum (initial) gap.

A plot of force versus gap for several different values of s is provided in Figure 5.4. The forces in this figure are calculated using the same electrode and gap parameters provided in Table 5.1. As seen in the figure, an increase in the parameter s (and therefore increased electrode slope) decreases the electrostatic force as expected due to the increased gap between electrodes. Interestingly, this force reduction is high at small gaps and relatively small at

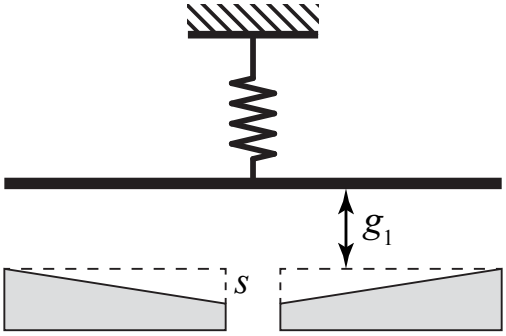

Figure 5.3: Sloped shape of the fixed electrode in zipping actuators

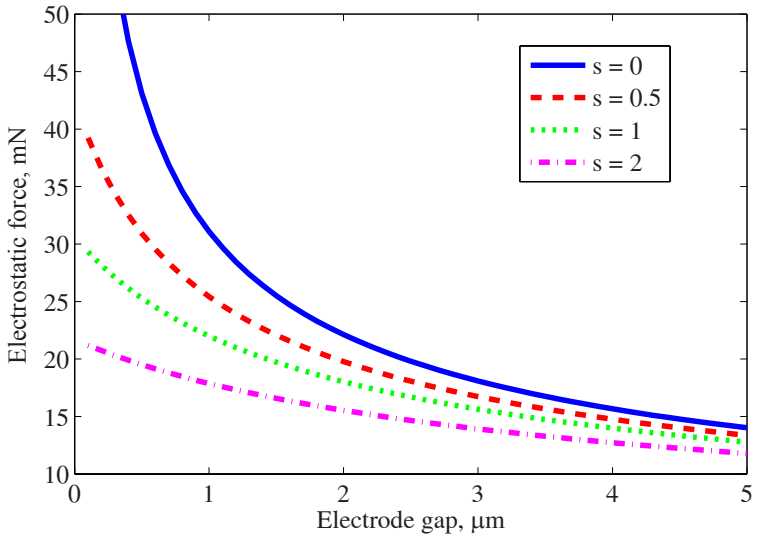

Figure 5.4: Force-gap relationship for different fixed electrode slopes. The electrode gap is g_1 and force is defined as the engagement force F_{eng}. s is defined in Figure 5.3

large gaps, effectively flattening the force curve. As a result, the total motor force does not change considerably through its full displacement. In a motor with rigid straight electrodes the electrostatic force continues to increase as the gap closes past g_{eng}, but that increase does not improve the force output (Figure 2.9). Flattening of the force profile, as enabled through sloped electrodes, can potentially increase the efficiency of the motor because it will not waste energy doing more work than is needed.

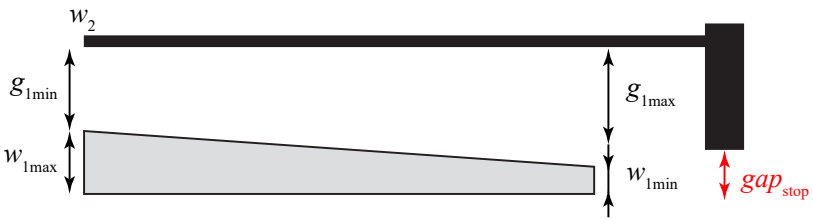

Figure 5.5: Variable parameters in zipping electrodes

5.3 Actuator design and fabrication

5.3.1 Actuator Variations and Design

To validate these modeled forces, parameterized actuators of each type (rigid, compliant, and zipping) were designed and fabricated. Compliant actuators were designed in a similar fashion to the rigid actuators in Section 2.2.6 but the movable actuators were made more compliant with smaller widths. While rigid actuators had electrode widths of 8.3 µm, the compliant actuators had fixed electrode widths of 8.3 µm and movable electrode widths varying from 7.3 µm down to 3.8 µm.

Based on the numerical analysis discussed above, designs with movable electrode widths of 4.3 µm and 3.8 µm were expected to zip close. In addition to parallel electrodes with no slope, electrodes of the same two widths were also designed to interact with sloped fixed electrodes. The parameter s was designed to range from 0 to 3. These designs comprised the zipping actuators tested.

The number of independent design parameters (gaps, slopes, etc.) that had a significant effect on the motor performance was much higher than in the rigid electrode design. Some of

these parameters are listed in Figure 5.5, and Table 5.2 represents all layout variations that were designed and fabricated. While the actuators on their own were the primary interest of this chapter, these actuators were integrated into inchworm motors and therefore designed with motor operation in mind. Therefore, the thickness and angle of the motor's flexible arm were also varied to account for the expected displacement and maximum forces. In addition, modeled force magnitudes were used as a rough design guideline; more emphasis was placed on assuring that each actuator displaced the correct amount to complete an entire inchworm cycle when used in the full motor design. Finally, gap stops were pushed back so that they did not obstruct zipping between electrodes. As seen in Table 5.2, actuator force, calculated as F_{y}, was expected to range from 5.56 mN to 79.7 mN for the rigid to a zipping actuator respectively. Similarly, motor force, calculated as F_{x}, was expected to range from 4.29 mN to 119 mN for rigid to zipping motors. All of the actuators except for Rigid and Flex 1-3 were designed to zip close.

5.3.2 Actuator Fabrication

The motors were manufactured using a similar process to that described in Section 2.3.1, using a single deep reactive ion etch on an SOI wafer. For these motors, the device layer thickness was 40 µm with a buried oxide layer of 4 µm or 5 µm depending on the wafer used. Wafer resistivities were similar or less than 10 mΩ cm. A key difference between the motors fabricated here and those fabricated in Section 2.3.1 was that several modifications were made to the DRIE recipe to achieve better etch uniformity and higher

Table 5.2: Parameters of motors with zipping electrodes

Name	w_1 (µm)		w_2	g_1 (µm)		s	**gap st.**	**flex arm**		F_y	F_x
	max	min	(µm)	max	min	(µm)	(µm)	$\alpha, ^\circ$	b_{arm}	(mN)	(mN)
Rigid	8.3		8.3	5.6		0	4.9	67	3.3	5.56	4.29
Flex #1	8.3		7.3	5.6		0	4.9	67	3.3	5.72	4.42
Flex #2	8.3		6.3	5.6		0	4.9	67	3.3	6.07	4.72
Flex #3	8.3		5.3	5.6		0	4.9	67	3.3	8.06	6.41
Flex #4	8.3		4.3	5.6		0	4.9	67	4.0	79.7	67.2
Flex #5	8.3		3.8	5.6		0	4.9	67	4.0	72.6	61.2
Fl #4 Sl #1	8.3	7.8	4.3	6.1	5.6	0.5	5.9	67	4.0	69.4	58.5
Fl #4 Sl #1s	8.3	7.8	4.3	5.6	5.1	0.5	5.4	67	4.0	79.4	67.0
Fl #4 Sl #2	8.3	7.3	4.3	6.6	5.6	1.0	6.2	67	4.0	62.1	52.3
Fl #4 Sl #2s	8.3	7.3	4.3	5.6	4.6	1.0	5.2	67	4.0	78.8	66.5
Fl #4 Sl #3	8.3	6.3	4.3	7.6	5.6	2.0	7.2	67	4.0	52.2	43.9
Fl #4 Sl #3s	8.3	6.3	4.3	6.1	4.1	2.0	5.7	67	4.0	66.0	55.6
Fl #5 Sl #1	8.3	7.8	3.8	6.1	5.6	0.5	5.9	67	4.0	63.3	53.3
Fl #5 Sl #1s	8.3	7.8	3.8	5.6	5.1	0.5	5.4	67	4.0	72.4	61.0
Fl #5 Sl #2	8.3	7.3	3.8	6.6	5.6	1.0	6.2	67	4.0	56.7	47.7
Fl #5 Sl #2s	8.3	7.3	3.8	5.6	4.6	1.0	5.2	67	4.0	72.0	60.7
Fl #5 Sl #3	8.3	6.3	3.8	7.6	5.6	2.0	7.2	67	4.0	47.7	40.1
Fl #5 Sl #3s	8.3	6.3	3.8	6.1	4.1	2.0	5.7	67	4.0	60.5	50.9
Fl #5 Sl #4	9.3	6.3	3.8	8.6	5.6	3.0	8.1	67	4.0	41.8	35.1
Fl #5 Sl #4s	9.3	6.3	3.8	7.1	4.1	3.0	6.6	67	4.0	50.2	42.2
Fl #4 Sl #3 a60	8.3	6.3	4.3	7.6	5.6	2.0	7.2	60	4.0	52.2	59.8
Fl #4 Sl #3 a50	8.3	6.3	4.3	7.6	5.6	2.0	7.2	50	4.0	52.2	87.2
Fl #4 Sl #3 a45	8.3	6.3	4.3	7.6	5.6	2.0	7.2	45	4.0	52.2	104.0
Fl #5 Sl #4 a60	9.3	6.3	3.8	8.6	5.6	3.0	8.1	60	4.0	41.8	47.8
Fl #5 Sl #4 a50	9.3	6.3	3.8	8.6	5.6	3.0	8.1	50	4.0	41.8	69.7
Fl #5 Sl #4 a45	9.3	6.3	3.8	8.6	5.6	3.0	8.1	45	4.0	41.8	83.2
Fl #5 Sl #4 a35	9.3	6.3	3.8	8.6	5.6	3.0	8.1	35	4.0	41.8	119.0

Table 5.3: Wafers used for manufacturing

Wafer	Properties	Comments
#1	530/5/40 µm, res (1 . . . 3) mΩ-cm	UMD cleanroom
#2	500/4/40 µm, res <10 mΩ-cm	ARL cleanroom

Table 5.4: Al_2O_3 homogeneous dielectric layers tested for actuators insulation

Label	Structure	T, °C	Cycles	Comments
AlO1	AlO	150	800	Negligent charging, low leakage current, breaks down around 120 V
AlO2	AlO	150	1000	Some charging, low leakage current, breaks down around 140 V. Also deposited at 220 °C and with ozone
AlO3	AlO	150	1200	Noticable charging, low leakage current, breaks down around 160 V
AlO4	AlO	150	1600	Extensive charging, erratic leakage current, inconsistent breakdown voltage

AlO – dielectric layer consisting of only Al_2O_3 oxide

aspect ratio of the trenches. Since these trenches ultimately define the gaps in the actuator, it was important that they be as vertical and smooth as possible.

Finally, several variations of dielectric films were deposited using ALD (including multilayer options) to reduce leakage current and/or increase dielectric constant and therefore output force. A selection of these variations are included in Tables 5.4 and 5.5.

5.4 Experimental setup

5.4.1 Electrical Characterization

Actuator force characteristics are particularly challenging to measure, given that displacements are often the only obvious output and actuator springs require significant calibration [20]. Therefore, an *electrical* characterization method as described in Chapter 4

Table 5.5: Laminated dielectric layers (Al_2O_3 and TiO_2) tested for actuators insulation

Label	Structure	T, °C	Cycles	Comments
ATO1	AlO/ATO/AlO (A:T=1:3)	150	50/400/50	Conductive even after multiple annealing attempts
ATO5	AlO/ATO/AlO (A:T=1:3)	150	200/600/200	Annealing at 300 °C for 3 hours, bubbles. High leakage current even before zipping
ATO6	AlO/ATO (A:T=1:3)	150	200/400	Annealing at 300 °C for 3 hours. Significant charging. Breaks down around 120 V
ATO7	AlO/ATO (A:T=1:4)	150	100/380	Annealing at 200 °C for 3 hours. After few weeks moderate leeking. Multiple annealing and tests, after last breaks down around 100 V.
ATO8	AlO/ATO (A:T=1:3.5)	150	150/400	Annealing at 200 °C for 3 hours. Breaks down around 100 V. Multiple annealing and tests
ATO9	AlO/ATO (A:T=1:3)	220	200/400	Multiple annealings and tests. After 300 °C for 3 hours leakage became very low. Significant charging, breaks down above 120 V
ATO10	AlO/ATO (A:T=1:10)	150	100/200	Multiple annealings and tests. Charging. Breaks down around 100 V.
ATO11	AlO/ATO (A:T=1:10)	150	100/200	Annealing at 200 °C for 6 hours

AlO – dielectric layer consisting of only Al_2O_3 oxide;
ATO – laminate layer consisting of interchanging Al_2O_3 and TiO_2 oxides.

was used. In this method, the frequency response of the actuator is measured at different displacements (resulting from different applied DC bias voltages). Using this frequency response and a model of the test setup, the actuator capacitance can be calculated for varying displacements withing its range of motion. Since actuator force is proportional to the derivative of this capacitance, actuator force can then be found at corresponding displacements. For inchworm motors, force at engagement (g_{eng}) is its defining characteristic. However, due to instabilities in the gap closing actuators and the resulting fast motion, it is impossible to make capacitance measurements at the engagement point using *electrical* characterization method. Therefore, these capacitance curves (plot of capacitance vs displacement) will be used only for estimates of actuators' force. Comparison between actuators can be done using slopes of capacitance curves, a higher slope implies a higher electrostatic force.

The *electrical* characterization tests on zipping actuators used the same test setup, methods and procedures as described in Chapter 4.

5.4.2 Disengagement Force Characterization

Due limitations of the measured data in *electrical* characterization, the test setup was modified to gather transient response and more direct measure of the force from actuators. These tests were described in Chapter 4 as *electromechanical* characterization. An experimental setup demonstrated in Figure 5.6 was used to perform these tests. The electronics used to drive the actuator and measure the frequency response are the same as in Figure 4.2 (pictured as 1-5,7 in Figure 5.6). The actuator is depicted as a zipping actuator in this

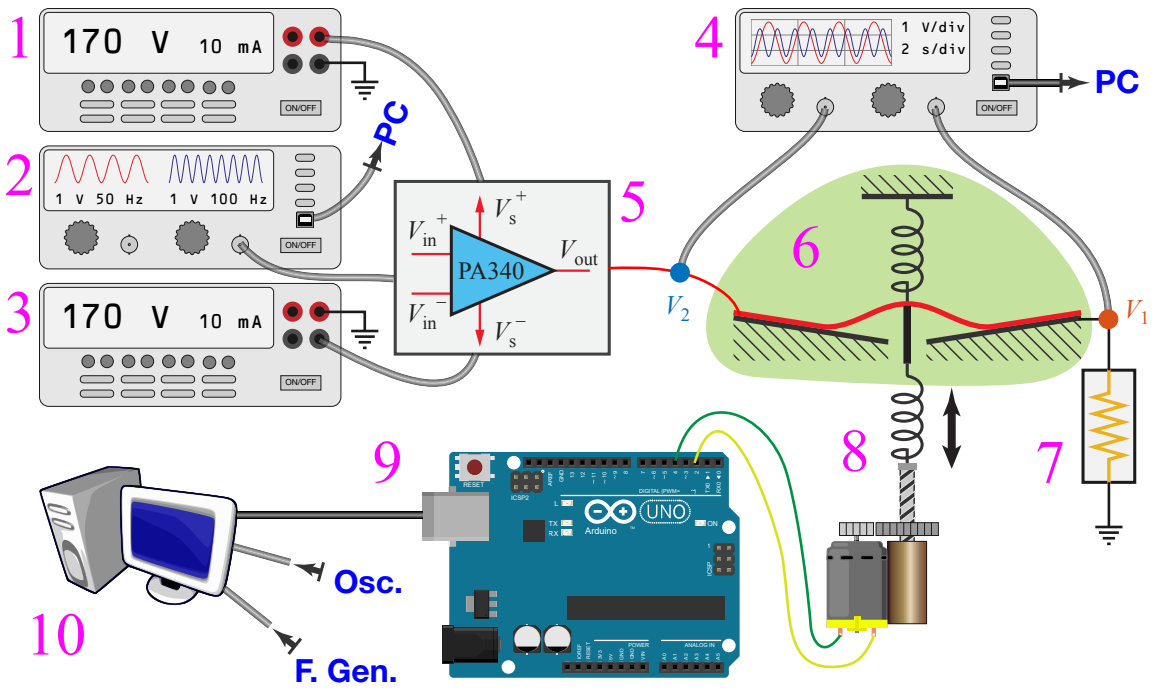

Figure 5.6: Test setup used to measure the maximum disengagement forces in gap closing actuators.

Figure and labeled as 6. The new portions of this test setup include a servo motor and thin probe (modeled as linear spring, item 8) used to load the actuator after it has been engaged. This motor is driven by an Arduino (item 9) and a PC (item 10) is used to capture motor displacement as well as electronic and photographic data from the actuator.

Electromechanical characterization tests were conducted as follows: a DC voltage was applied to the actuator while recording voltage signals V_1 and V_2. Upon actuator stabilization, its picture was taken for displacement measurement. Then, the servo motor drove a thin probe to mechanically contact the actuator and force it to disengage (while keeping the DC voltage ON). When resistive force from the thin probe was high enough to counteract the electrostatic force in the zipping actuator, the electrodes would disengage. The resulting

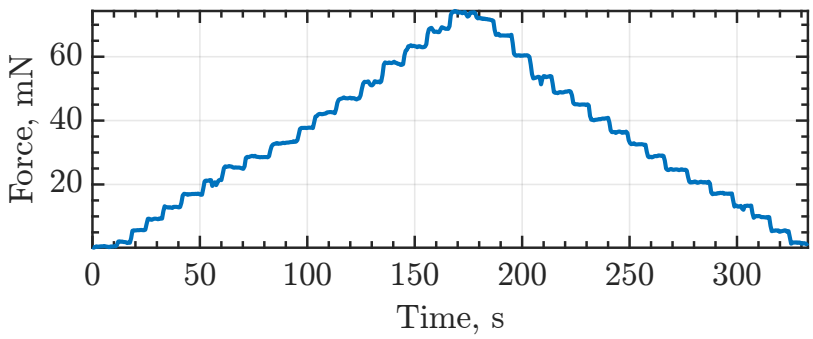

Figure 5.7: Force sensor data during the probe spring constant calibration test

voltage spike in V_1 was recorded and served as the trigger to turn off applied DC voltage. Then, actuator was reset and the experiment was repeated for higher DC voltage.

These characterization tests allowed to measure directly disengagement force of electrostatic actuators at varying applied voltages. The probe used to push the actuator was calibrated to measure its spring constant. The distance that servo motor moved the probe before the disengagement of the actuator was calculated based on voltage spike from V_1. The voltage V_1 was used to calculate current flowed into or out of the DUT since it was measured across the known resistor R_{m}. This current then was integrated to obtain the charge transferred into the actuator.

Since actuators and motors will ultimately have a load applied, the disengagement force can be thought of as the maximum load that the actuator can support. While disengagement force will certainly have some relationship to engagement force, this relationship is complex and differs between the types of actuators discussed in this work (rigid, compliant, and zipping).

To calibrate this experimental setup, the load applied by the motor and thin probe

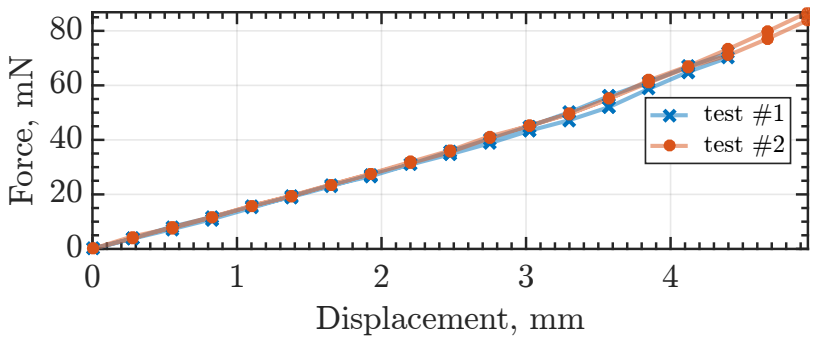

Figure 5.8: Results of the probe spring constant calibration tests

(modeled as linear spring) was instead applied to an ATI Nano17 6-axis force/torque sensor. Figure 5.7 shows forces measured from the ATI Nano17 over time with small displacement steps applied to the spring. This data was used to generate a calibration curve for the spring in Figure 5.8. Two different trials were run and shown to be consistent and relatively linear, especially over the small displacements used to disengage the actuators. In this linear region, the spring constant was found to be 14 mN/mm. Disengagement forces calculated using this spring constant and the applied motor displacement are used in the following results.

In addition, the sourcemeter used in this test setup allowed for the measurement of charge delivered to the actuator and returned from the actuator over time. During disengagement, charge returned to the source describes how capacitance changes over time ($\Delta Q = \Delta CV$). Returned charge is defined as the total amount of charge returned to the source. A larger returned charge is indicative of a higher change of capacitance and a higher force.

Disengagement forces will change for different actuators based on their geometry and mechanics. For example, it may be easier to peel very compliant actuators apart versus rigid

actuators even though the applied force might be the same. Normalized force is provided as a metric to compare this effect and is defined as the disengagement force divided by the returned charge. A higher normalized force will mean that it is more difficult to disengage the actuator even though overall force is approximately the same. These actuators might be a better option in motors designed to support varying loads. Conversely, a smaller normalized force indicates that it is easy to disengage the actuator.

5.5 Results

5.5.1 Electrical characterization

5.5.1.1 Actuator comparison

Figure 5.9 compares the change in capacitance as well as the voltage versus displacement curves for rigid, compliant, and zipping actuators plotted together. Only the final stage of the movement is plotted to highlight the most interesting behavior. The instabilities are indicated by a rapidly increasing slope seen most clearly in the voltage vs displacement plot (bottom half of Figure 5.9). The zipping actuators show clear increases in force over the rigid actuator. This matches the expected results. However, the magnitude of the improvement is far below that expected in Table 5.2. Hypotheses for this mismatch are discussed further in Section 5.6.

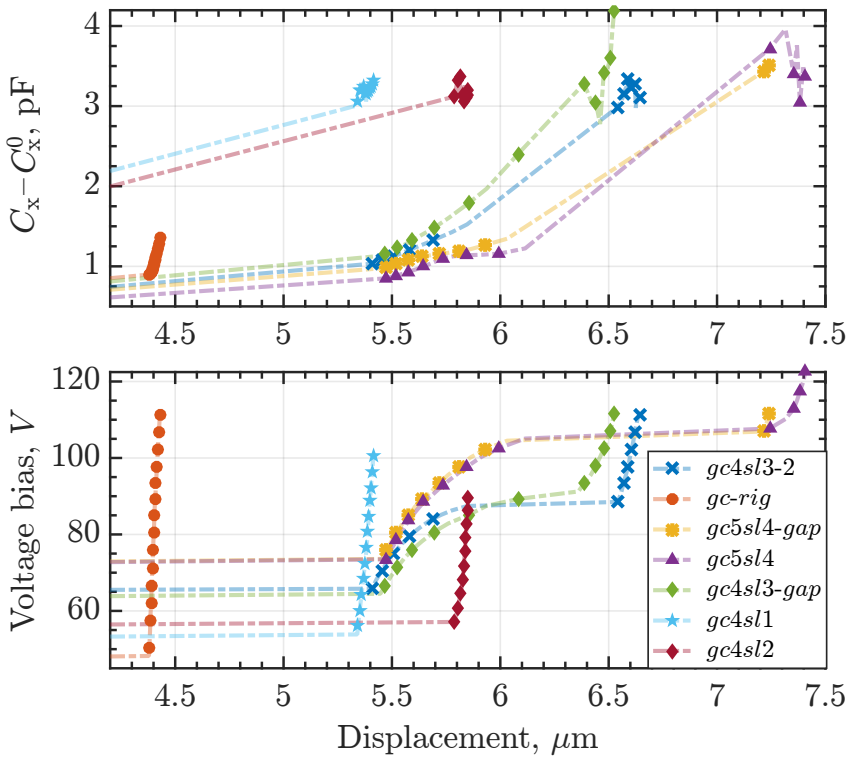

Figure 5.9: Demonstration of varying zipping behavior at GCAs with different designs ('s' parameter and electrode compliance). Only the final stage of the movement is demonstrated to highlight pull-in.

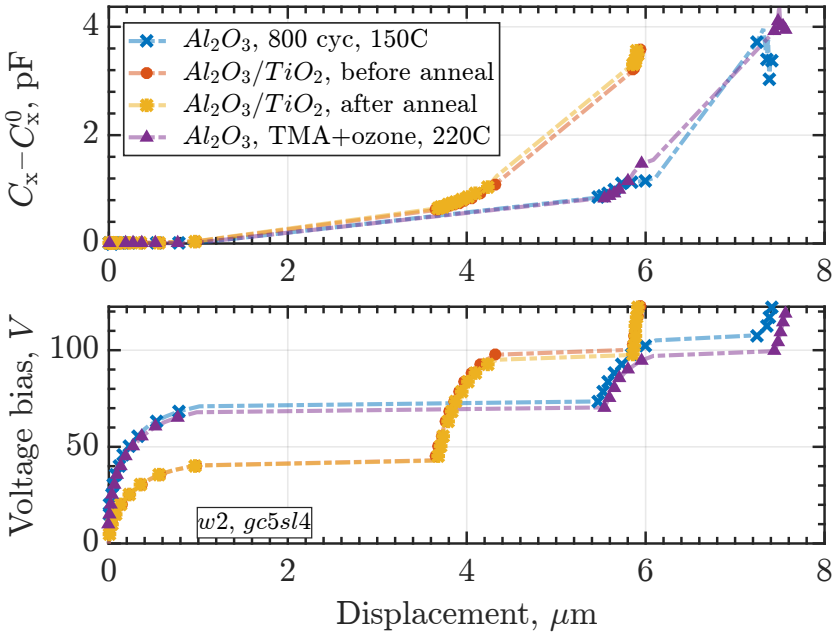

Figure 5.10: Zipping GCA ($w2$, $gc5sl4$) in quasi-static tests, comparison of several different dielectric layers.

5.5.1.2 Dielectric film comparison

As seen in Figure 5.10, the dielectric film coating of the electrodes can have significant effects on the change in capacitance and ultimately actuator force. Films with higher dielectric constant like the aluminum oxide and titanium oxide laminates (indicated by the red circles and yellow squares) are expected to have a higher capacitance at the same displacement and this clear in Figure 5.10. However, the displacement at which an instability is reached is smaller for the laminate dielectrics. Since these laminates increase the electrostatic force, an earlier pull-in is to be expected.

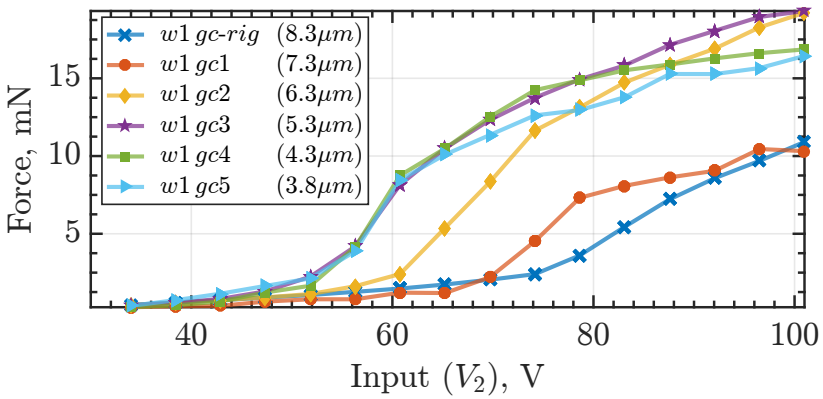

Figure 5.11: Comparison of release forces in compliant GCAs as a function of applied voltage and thickness of movable electrodes

5.5.2 Disengagement force

5.5.2.1 Compliant electrodes

Figure 5.11 compares the disengagement force as a function of the applied voltage and thickness of the movable electrodes. As expected, an increase in applied voltage results in a higher disengagement force and this relationship is nonlinear. One noticeable result is that the voltage at which the disengagement force begins to dramatically increase decreases as the electrode width decreases (and the electrode becomes more compliant) although this seems to level off at an electrode width of 5.3 µm. This makes sense as all of the smaller electrode widths including 5.3 µm zipped in and were in physical contact. Small differences at higher voltages for these actuators are likely due to the energy stored in the movable electrode as a spring.

The returned charge was also measured during these disengagement force tests to obtain a measure of the actuator force (Figure 5.12). A smaller returned charge should be

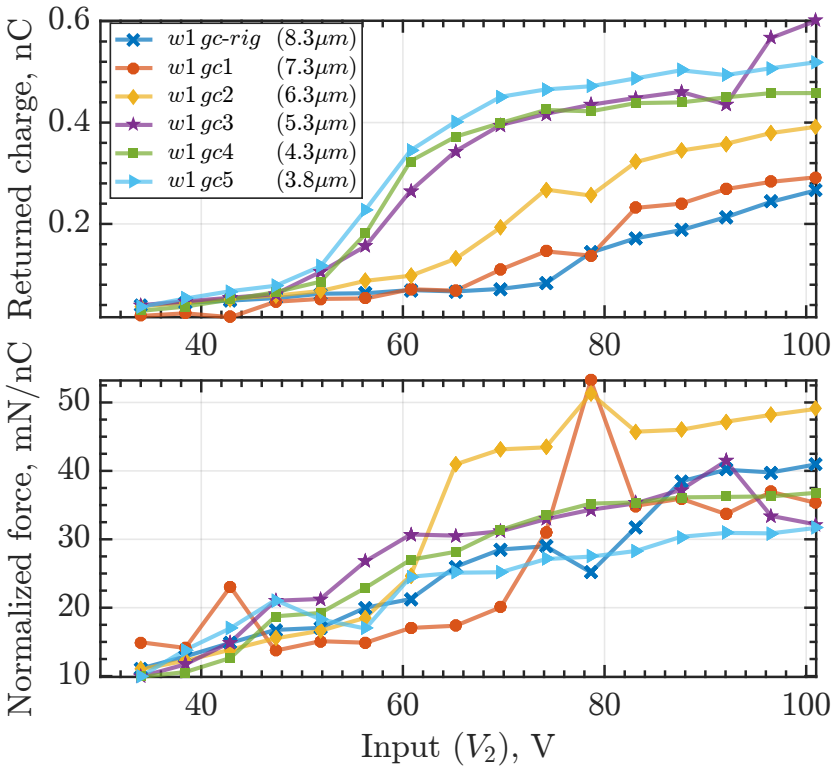

Figure 5.12: Comparison of return charge and normalized release force for compliant electrodes

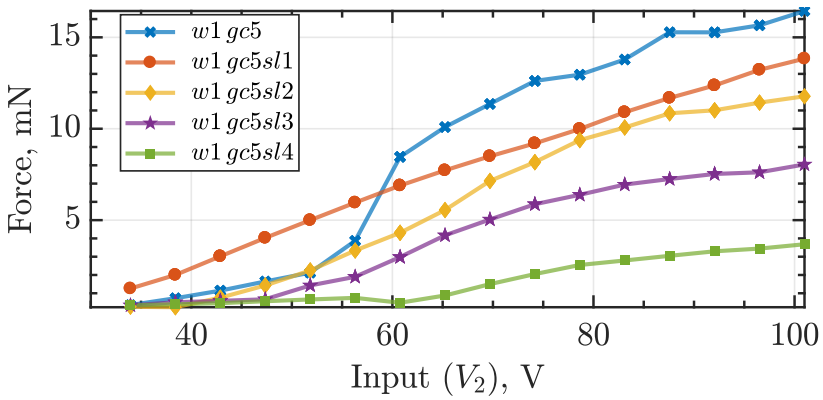

Figure 5.13: Comparison of release forces in GCAs with 3.8 µm movable electrodes as a function of applied voltage and electrodes' 's' parameter

indicative of a smaller change in capacitance, and therefore a smaller force. As expected, more compliant electrodes result in higher returned charge. The actuator with rigid electrodes is expected to have the lowest force and was also measured with the smallest returned charge. Normalized forces were fairly similar indicating that these electrodes disengaged in similar manners.

5.5.2.2 Sloped zipping actuators

The analysis demonstrated that actuators with a larger 's' value should see a reduced force due to the increased gap between electrodes. Figure 5.13 shows this trend as expected for actuators with a movable electrode width of 3.8 µm. The actuator with parallel electrodes has the highest disengagement force and the actuator with the greatest slope in its fixed electrode has the lowest disengagement force at about 25 % that of the parallel electrodes. In addition, the analysis predicted that the actuator force versus displacement curve would flatten out. While disengagement force does not directly measure this, voltage can be thought

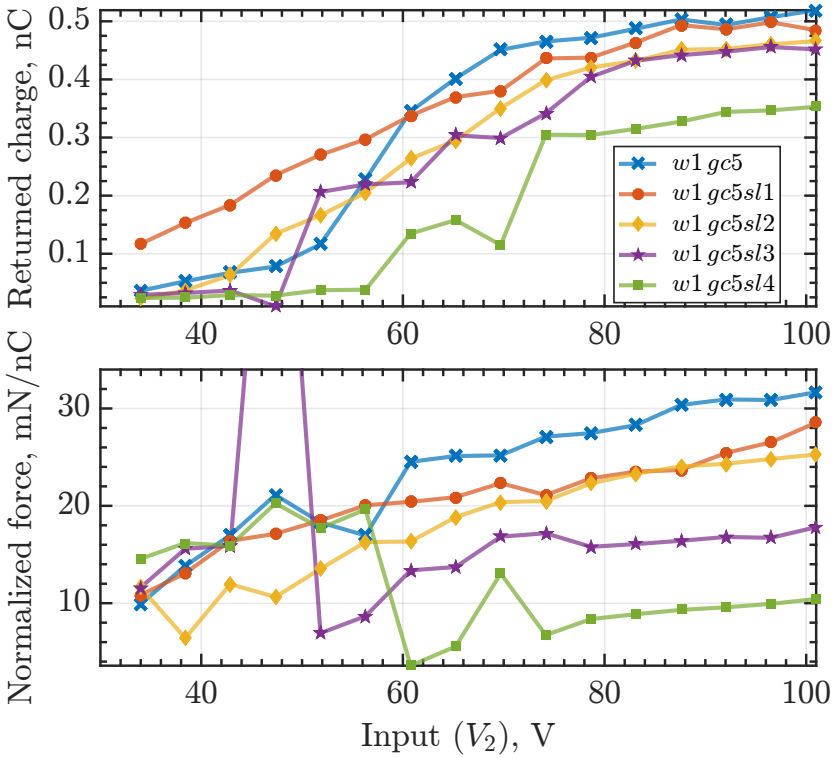

Figure 5.14: Comparison of return charge and normalized release force for zipping/sloped electrodes with 3.8 µm movable electrodes

of analogously to displacement and the disengagement force versus voltage curves do indeed flatten out in comparison to the parallel electrodes in Figure 5.13.

The returned charge in Figure 5.14 indicates a similar force trend. The largest returned charge is found in the actuator with parallel electrodes while the smallest returned charge is found in the actuator with the largest slope. Normalized force is an especially interesting metric to look at in these actuators. Since the sloped electrodes encourage peeling at disengagement, higher slopes result in especially low normalized force. The parallel electrodes have the highest normalized force – over $3x$ the normalized force of the actuator with $s = 4$.

Very similar results are found when comparing actuators with a movable electrode

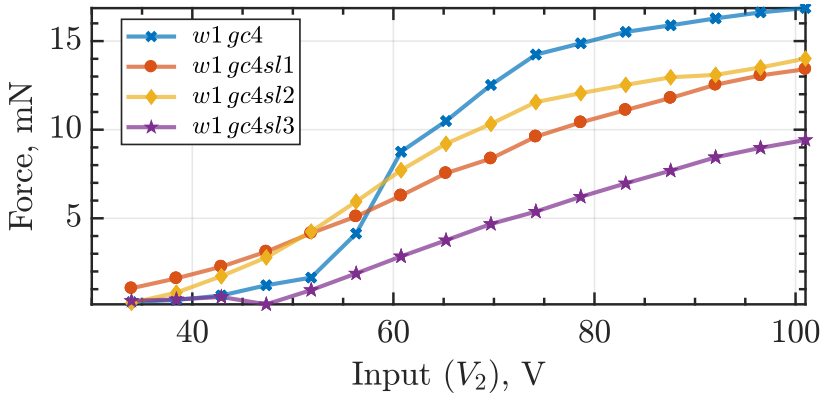

Figure 5.15: Comparison of release forces in GCAs with 4.3 µm movable electrodes as a function of applied voltage and electrodes' slope

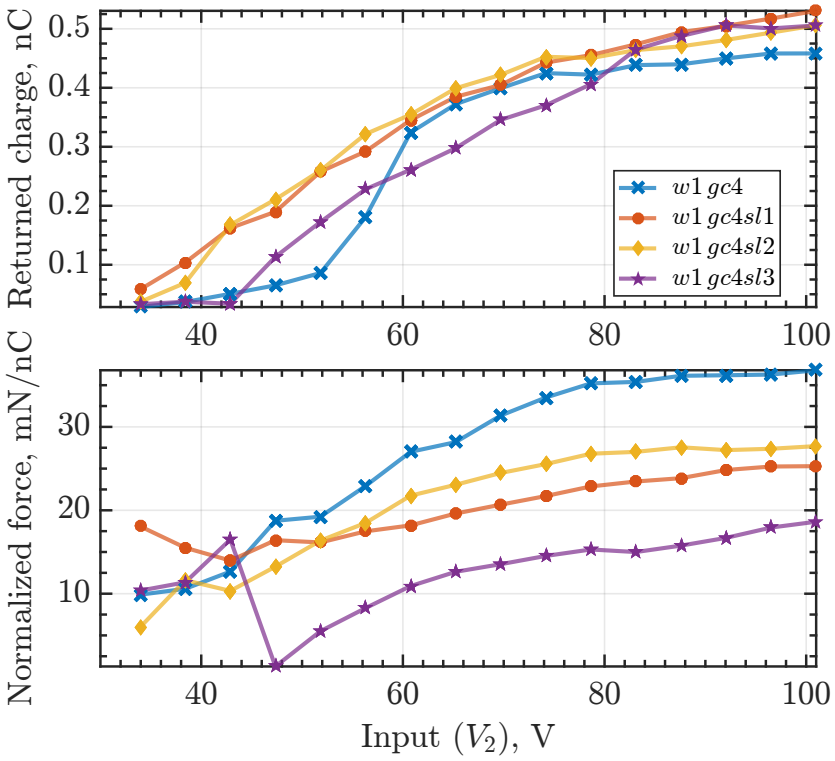

Figure 5.16: Comparison of return charge and normalized release force for zipping/sloped electrodes with 4.3 µm movable electrodes

thickness of 4.3 µm in Figures 5.15 and 5.16. Here, we expect that returned charge should be very similar. Actuator force is dependent on the gaps and actuator gaps are the same for the actuators even though electrode compliance is different. More interesting differences can be found in normalized force; the differences in normalized force between actuators with different slopes are not as dramatic in the case where a stiffer electrode is used. This indicates that it is more difficult to disengage an actuator with more rigid electrodes.

5.5.3 Motor tests

Finally, full motors using both compliant and zipping actuators were tested. Motors using non-rigid actuators had numerous challenges during actuation. In many cases, actuators with compliant electrodes pulled in at different rates resulting in one side not pulling in at all. This is related to the discussion of asymmetric pull-in in Chapter 2. It is hypothesized that the flexible arm is not sufficient to stabilize the motor in this case due to the different dynamics of zipping actuators. With very careful actuator timing, some small displacements were seen, but the forces were not nearly as high as expected. Overall, while zipping actuators may be useful for a number of applications (e.g. [1]), their incorporation into inchworm motors proved to be too challenging. These challenges, and lower forces in particular, are discussed in greater detail in the following section.

5.6 Discussion

Most notably in both actuator and motor tests, the expected changes in capacitance (relating to force) and forces did not come close to matching the predicted force improvements from zipping actuators. One observation relates to the sidewall fabrication of electrostatic gap closing actuators. As seen in 5.1, the electrostatic force greatly depends on the gap between electrodes. Therefore, the quality of sidewalls (smoothness, orientation, and slope) is very important, and the remaining gap can severely reduce the produced force. A simple estimation for a constant sidewall angle shows that the decrease of force in GCAs is

$$\rho = \frac{F_{\text{sloped}}}{F_{\text{best}}} = \frac{1}{1 + 2\,t/g\tan\alpha}, \tag{5.3}$$

where α is the sidewall angle, t silicon layer thickness, and g is the smallest gap (across thickness) between electrodes. Figure 5.17 shows the decrease in actuator force for several different gaps. This plot makes it apparent that standard, rigid GCAs do not suffer from manufacturing issues as strongly as the zipping actuators due to the relatively large gap always maintained between electrodes to prevent shorting. This might be one of the reasons electrostatic motors presented in Chapter 2 exerted force within 10 % of predicted values.

However, the proposed benefit of zipping GCAs lays in their ability to form a near zero gap between electrodes and utilize the resulting high intensity electric field for high forces. Sloping of the sidewalls or other extra roughness brings a significant force reduction as seen in Figure 5.17. In zipping actuators, engagement with the shuttle occurs after electrodes

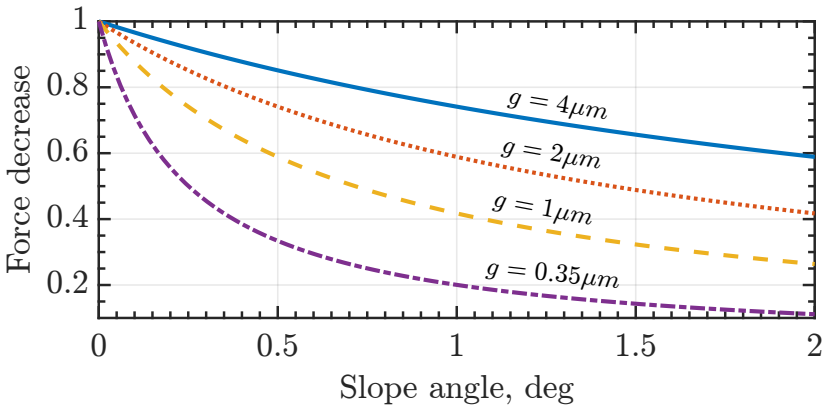

Figure 5.17: GCA force decrease due to sloped sidewalls for several gaps ($t = 40\,\mu m$)

made contact; therefore the gap to consider for (5.3) is equal to double the thickness of the ALD dielectric films used as electrical insulators ($g \approx 0.35\,\mu m$). If the sidewalls are sloped only 1° or 2°, the electrostatic force is only correspondingly 20 % or 10 % of its predicted value.

In rigid GCAs, the engagement gap determines the maximum force ($g_{eng} \approx 2\,\mu m$). The fraction of predicted electrostatic force for the same slope angles (1° and 2°) is significantly higher – 60 % and 40 %.

The challenges of fabricating MEMS electrostatic actuators with perfect sidewalls was discussed previously. However, the new zipping design sets stringent requirements on the manufacturing quality (maybe even unrealistically high for standard DRIE equipment). The surface of the trenches is never smooth after DRIE but there are several techniques to improve it (DRIE recipe, annealing, oxidation + etch, isotropic etch, etc.). The sidewall angle can be adjusted by varying the DRIE recipe parameters but it is difficult to maintain the same profile across an entire wafer and through the entire trench.

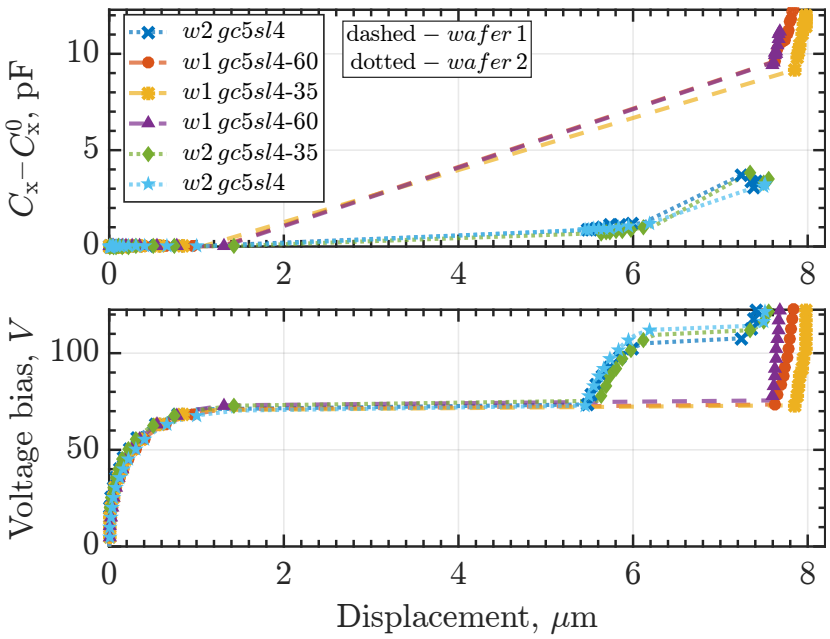

Figure 5.18: Contrast in capacitance measurements between similar design GCAs but manufactured on different wafers.

To further validate this hypothesis, the same actuators were fabricated on a very similar wafer using the a slightly different version of the STS deep reactive ion etcher in a different lab. The capacitance measurements for the same GCA fabricated on these two different tools is shown in Figure 5.18. The actuators fabricated on the second wafer show drastically different changes in capacitance and therefore very different forces. However, this was unexpected. The actuation of the two groups of GCAs was very similar as seen in the voltage versus displacement plot. While the two groups have slight changes in pull-in voltages, this is not unusual. In addition, the devices looked very similar visually and test structures used to track the progress of the deep reactive ion etch during fabrication did not raise concerns.

Two conclusions were drawn from this experiment. The first is that all flaws of the GCAs on the second wafer were extremely well concealed. The problem was exacerbated by

the fact that the reentrant trenches are more common due to specifics of the DRIE process. This means that the remaining gap is located at the bottom of the structures and can not be visually identified during tests. In addition, the microscopic scale of actuators restricts the detailed nondestructive inspection only to a scanning electron microscope (SEM). However the high aspect ratio of trenches makes it almost impossible to peer all the way to the bottom. The destructive methods have an obvious drawback of destroying the DUT. Also detection of a slight slope or thickness difference on the order of 1 µm on a slender freestanding feature carries a lot of practical challenges (resolution, scallops, clean cross-section, perpendicularity of the camera view to the cross-section, etc.) which ultimately reduces the accuracy of these measurements. To truly understand the nature of the problem, a better understanding of what is going on during the transient zipping behavior is needed. However, measuring this at bandwidths of several hundred kiloHertz is challenging.

5.7 Conclusions

This chapter explored the use of compliant electrodes in gap-closing actuators to increase force output. Both non-zipping and zipping actuators were designed and fabricated. These actuators were tested using both electrical and electromechanical characterization techniques. The same electrical characterization described in Chapter 4 showed expected increases in ΔC_x as the movable electrodes became more compliant, but these increases were not nearly as high as expected. The electromechanical tests described in this chapter to characterize disengagement provided another proxy for force measurement and also

characterized how easy it was for different actuators to disengage when encountering a load.

Overall, while designs with compliant electrodes did increase actuator force, they did not increase it as much as expected from initial calculations. Several hypotheses were raised and explored including the effect of sidewall slope and roughness in these zipping actuators. The same actuator designs fabricated in two different cleanrooms showed significantly different force profiles – an unexpected result, but one that supports the hypothesis that minor changes in sidewall roughness and profile can significant affect actuator force output during zipping.

Chapter 6

Measurement of transient behavior in electrostatic zipping actuators

6.1 Introduction

Zipping actuators are complex gap closing actuators with interesting dynamic behavior [1]. By definition, they require contact between electrodes and require an insulating layer to prevent shorting. This contact and insulating layer can ultimately affect the actuator performance and many applications (e.g. relays, microrobotics) require knowledge of the force and displacement of these actuators over time. However, characterizing the transient performance of these actuators is challenging due to the inherent instability and very high speeds of actuation (typically on the order of 10 µs). To capture the transient properties of these actuators during actuation as well as the affect of different insulating layers used in gap closing actuators, new characterization methods are needed.

This chapter offers two contributions: 1) a new characterization method of fast dynamics in which the actuator is considered primarily as an electrical device versus an elec-

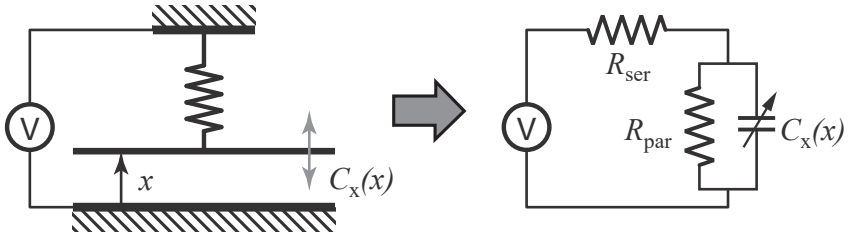

Figure 6.1: Electrical model of the electrostatic actuator

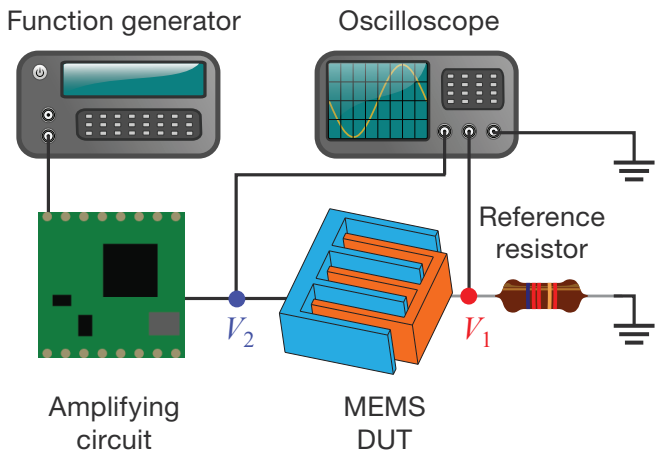

Figure 6.2: Electrical setup in electrostatic actuators characterization tests

tromechanical system, and 2) use of this method to characterize the effect of different etch parameters and different dielectrics in zipping actuators. Central to both of these contributions is the circuit model in Figure 6.1. Here, R_{ser} represents resistance of the connection wires and electrodes themselves; R_{par} represents the parasitic resistance (ionized air, substrate, etc) that allows for leakage current across the capacitor; and $C_{\text{x}}(x)$ symbolizes the inter-electrode capacitance of the actuator (referred to as device under test or DUT).

An equivalent circuit describing the full test setup in Figure 6.2 is shown in Figure 6.3. Here, Z_{inp} represents the generalized input impedance of the amplifying circuit, function generator, and other circuit components that occur before measurement point V_2 in Figure 6.3. V_{inp} symbolizes the expected output voltage from the amplifying circuit. Z_{p1} and Z_{p2} represent the oscilloscope probes that were used to measure voltages V_1 and V_2 respectively. R_{m} represents a passive reference resistor. Finally, the MEMS DUT was represented by the model in Figure 6.1 with the exception of R_{ser}. Preliminary tests showed that its impact was

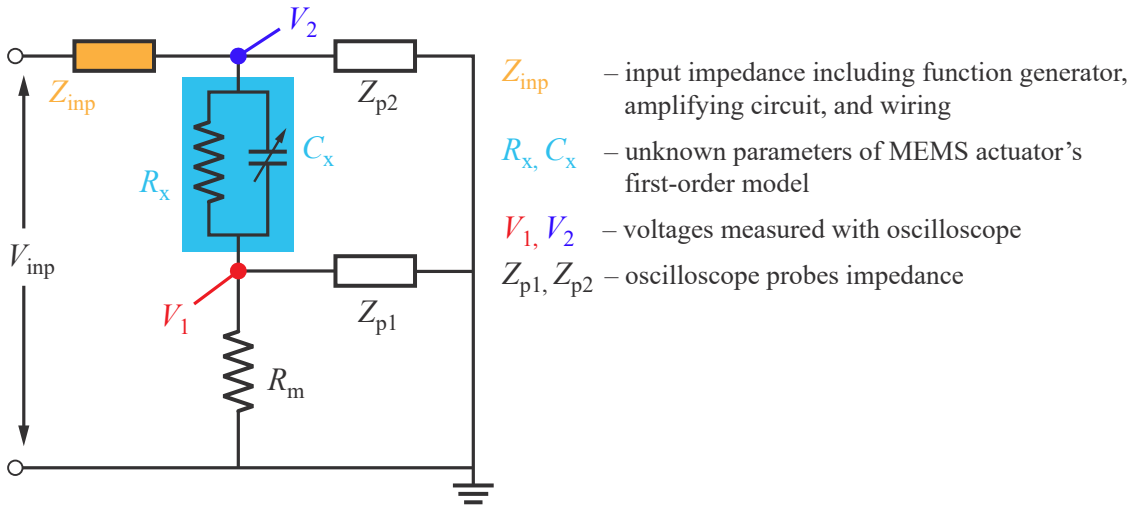

Figure 6.3: Electrical diagram of the electrical measurement setup

insignificant.

Chapter 4 previously characterized the quasistatic performance of electrostatic actuators using this basic circuit model and the test setup shown in Figure 6.2. In this case, a frequency response was measured from the actuator in order to identify the system and calculate actuator capacitance. However, measuring fast dynamic performance will require a new type of input and analysis.

6.1.1 Measuring actuator dynamics

A controlled constant rate spike (or asymmetric triangle) function was used in dynamic tests to obtain a time domain response (Figure 6.4). Since the rate of change in voltage is constant, the current across the capacitor C_x (representing the DUT) can be assumed constant in a first-order approximation. This approximation assumes that R_x is much larger than the impedance of the capacitive actuator. Therefore, assuming high impedance probes,

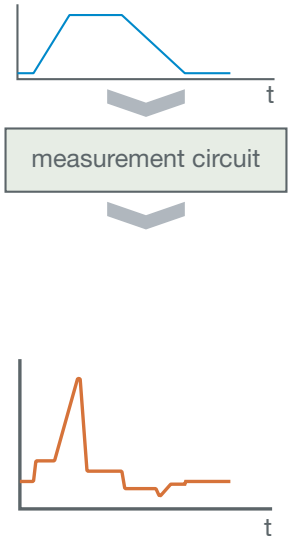

Figure 6.4: Constant rate spike input

the voltage drop on R_m is constant too.

$$V_1 = R_{\mathrm{m}} C_{\mathrm{x}} \frac{dV}{dt} \tag{6.1}$$

In the case of variable capacitance, the measured voltage (V_1) across the reference resistor (R_{m}) can be used to calculate the current and then the charge delivered to the DUT:

$$I_1(t) = \frac{V_1(t)}{R_{\mathrm{m}}}, \tag{6.2}$$

$$Q_1(t) = \int_0^t I_1 \, dt = \int_0^t \frac{V_1(t)}{R_{\mathrm{m}}} \, dt, \tag{6.3}$$

In the previous work, the change in actuator capacitance was matched to optical tracking of the actuator's displacement. However, in this case the optical tracking of an actuator's

displacements during ramp tests was practically impossible due to the lack of optical measurement equipment with µs-sampling capability that also has the resolution and light collection abilities required to measure a small motion. Hence, the measured temporal voltage (and calculated current and charge) data could not be matched up with the corresponding displacements. However, the main actuation phases in a cycle were deduced based on comparison of the expected and measured data.

Ultimately, use of this characterization method provides a measurement of three important properties of electrostatic actuators: force output, efficiency (due to leakage current), and trapped charge (that can affect pull-in and other performance over time). Due to the dynamic nature of these tests, no averaging was done and the results were more noisy and less consistent than quasistatic measurements performed previously. However, this method enabled insight into the fast dynamics and charge transfer in the actuators due to the higher temporal resolution of the MDO4054-3 oscilloscope (500 MHz).

Since the actuators in this study were operated in a constant voltage regime, the generated force is directly proportional to the change in capacitance and the voltage squared. The change in capacitance, in turn, is proportional to the delivered charge ($\Delta C = \Delta Q/V$ where ΔQ is defined from 6.3). Therefore, the measured voltage (and calculated charge) in ramp tests can be used to compare actuator capacitances and the force output of these actuators over time. Speed of charge transfer can also provide information on the speed of actuation.

6.1.2 Measuring leakage current

Measuring the charge transferred to and from the actuator can also be used to characterize the actuator's efficiency. Efficiency will depend on the actuator design and dielectric film properties. One significant detriment to actuator efficiency is leakage current in the actuator. The definition of leakage current in GCAs is the same as for standard capacitors – a small amount of current flows (or leaks) through the actuator when a voltage is applied. This current depends on several parameters: voltage magnitude, overlapping area of the electrodes and overall architecture of the actuator, the actuator's state/position, the dielectric film, and the medium that the actuator is in (e.g. vacuum, air, fluid). Leakage current can be determined from 6.2 when the actuator is in equilibrium.

There are several pathways through which leakage current can flow. The first pathway is independent of actuator position and is due to its manufacture on an SOI wafer; current can flow through the buried oxide layer to the common substrate. This can be exacerbated by any manufacturing debris (e.g. silicon grass) stuck amongst the actuator structures after release. With proper control over handling and fabrication, the contribution from this pathway is minimal.

A second route for leakage current is through the medium between the electrodes. For most of the tests conducted, this medium was air. This pathway is due in part to ionization of air in the presence of a strong electric field. Ionized air molecules can create short-lived conducting channels between the electrodes [51, 75]. The contribution of this route was not significant in the usual tests since the electrodes would move, close the gap and come into

contact when a high electric was applied. At that point the other phenomena would become dominant.

The final leakage mechanism bore the most responsibility for failures and actuator performance deterioration during experimentation. Dielectric films on the electrodes prevent the electrodes from shorting when in contact – especially important for zipping actuators in which contact is required. These films are intentionally designed to be thin (for a higher final capacitance) resulting in less insulation. In addition, the films were deposited using atomic layer deposition and often included intrinsic voids and other imperfections; cycling of the hard contact between electrodes enhances these imperfections due to gradual mechanical wear. The contribution of this leakage mechanism was expected to be marginal for low voltages but more dominant at higher voltages when electrodes were in contact.

6.1.3 Measuring trapped charge

Due to the high electric fields and physical contact between electrodes in zipping actuators, charge can also be trapped in the dielectric layer. This trapped charge typically sets up an opposing electric field and can change pull-in voltage and performance of the actuator over time [76]. 6.3 shows how the transfer of charge to and from the power supply can be measured over time. In an ideal electrostatic actuator or capacitor, charge would be transferred to the electrodes and the same amount of charge would be returned to the power supply. However, in a real system, more charge will be transferred to the actuator than will be returned. Leakage current as described above is one source of hysteresis in this curve and

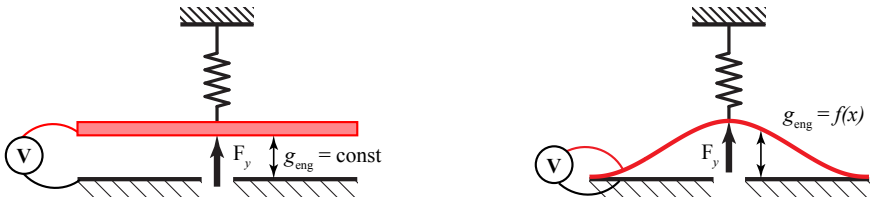

(a) Rigid electrodes (b) Zipping electrodes

Figure 6.5: Effect of compliance on electrode shape

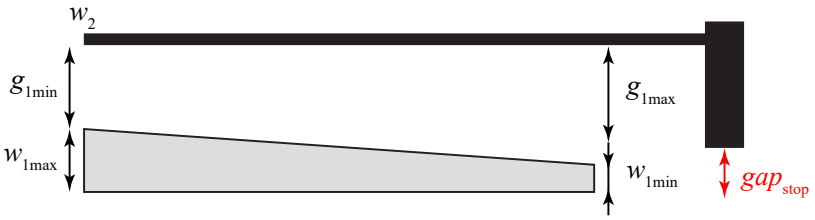

Figure 6.6: Variable parameters in zipping electrodes

the second is trapped charge that can not be returned to the power supply when voltage is ramped down.

6.2 Actuator design and fabrication

Both rigid and zipping actuators were designed for comparison purposes (Figure 6.5). The primary difference between these two actuator designs was the width of the movable electrode and the fixed electrode of the zipping actuators also had a slope to increase displacement (described more in depth in Chapter 5. The parameters for the actuator designs used to to study both the dynamic performance and dielectric behavior of these actuators are provided in Table 6.1 and a graphical description of the variables used is shown in Figure 6.6.

Table 6.1: Design parameters of actuators used for testing

Name	w_1		w_2	g_1		**zip**	F_y
	max	min		max	min	(Y/N)	
Rigid	8.3		8.3	5.6		N	5.56
Fl #5 Sl #4	9.3	6.3	3.8	8.6	5.6	Y	41.8

Table 6.2: Wafers used for manufacturing

Wafer	Properties	Comments
#w1	530/5/40 µm, res (1 . . . 3) mΩ-cm	UMD cleanroom
#w2	500/4/40 µm, res <10 mΩ-cm	ARL cleanroom

6.2.1 Actuator Fabrication

The motors were manufactured using a similar process to that described in Section 2.3.1, using a single deep reactive ion etch on an SOI wafer followed by an HF release. For these motors, the device layer thickness was 40 µm. A key difference between the motors fabricated here and those fabricated in Section 2.3.1 was that several modifications were made to the DRIE recipe to achieve better etch uniformity and higher aspect ratio of the trenches. Since these trenches ultimately define the gaps in the actuator, it was important that they be as vertical and smooth as possible.

To better understand the effect of etch parameters on the dynamics of zipping actuators, two different wafers and deep reactive ion etchers were used to fabricate the motors (Table 6.2). While the wafers used were very similar with the exception of a slightly thicker buried oxide layer in $w2$, the equipment and recipes used for the etch resulted in different sidewalls for the different motors. Given that zipping actuators require intimate contact between the two electrodes to provide high forces, it was hypothesized that even small differences in

Table 6.3: Al_2O_3 homogeneous dielectric layers tested for actuators insulation

Label	Structure	T, °C	Cycles	Comments
AlO1	AlO	150	800	Negligent charging, low leakage current, breaks down around 120 V
AlO2	AlO	150	1000	Some charging, low leakage current, breaks down around 140 V. Also deposited at 220 °C and with ozone
AlO3	AlO	150	1200	Noticable charging, low leakage current, breaks down around 160 V
AlO4	AlO	150	1600	Extensive charging, erratic leakage current, inconsistent breakdown voltage

AlO – dielectric layer consisting of only Al_2O_3 oxide

sidewall profile and roughness could result in significant affect on actuator performance.

Finally, several variations of dielectric films were deposited using ALD (including multilayer options) to reduce leakage current and/or increase dielectric constant and therefore output force. A standard approach previously taken by the authors uses homogenous aluminum oxide (Al_2O_3) deposited using atomic layer deposition (Beneq Atomic Layer Deposition). Various thicknesses of Al_2O_3 were examined in this work to compare their affect on force, leakage current, and trapped charge. Variations are described in Table 6.3.

Previous work [77, 78] demonstrated that laminated dielectric films dramatically increased the relative permittivity (ε_r) resulting in an increased force at the trade-off of higher leakage current and decreased breakdown voltage. Laminated dielectric films are commonly fabricated using ALD process by depositing alternating thin oxide layers. Considering the sequential nature of ALD manufacturing, the parameters of laminated dielectric films (e.g. thickness of each layer, order and number of layers) are easy to adjust and accurately control. Several oxides that are most commonly reported in laminated dielectrics are TiO_2, ZnO, and

Al_2O_3. The first 2 oxides are nearly conductive in the pure form but have very high relative permittivity (≈ 100). Al_2O_3, on the other hand, is a very good dielectric with a relative permittivity of ≈ 10. Alternating a very high dielectric layer with Al_2O_3 theoretically combines the advantages of each. The reported measured relative permittivity of these laminates varies significantly and this provides another opportunity to significantly increase the GCA's maximum capacitance and thus the exerted force.

Several different compositions for laminated dielectric films were deposited and tested (Table 6.4). The alternating oxides were TiO_2 and Al_2O_3. The choice for TiO_2 was made since it was readily available in the UMD FabLab and significant data on the manufacturing process exists. TiO_2 also has a very high relative dielectric measurement along with acceptable leakage current values in the literature [79, 80].

As noted in Table 6.4, the biggest challenge for use of these laminate dielectrics was the high conductivity of some films. In these cases, significant current flowed at all applied voltages. Basically, the films created a continuous coating with a fairly low internal resistance. In some instances the measured resistance between actuators' contact pads was on the order of $100\,\Omega$ which made them inoperable. Application of voltage led to significant heating within the actuator. Attempts of burning any low resistance bridges that may have been created by the ALD laminates by pumping large current (100s mA) were not successful in increasing the resistance between actuator electrodes.

One method used to solve this conductivity problem was through annealing the laminates after deposition. Multiple numbers of anneals at $200\,^{\circ}C$ or $300\,^{\circ}C$ were used in a

Table 6.4: Laminated dielectric layers (Al_2O_3 and TiO_2) tested for actuator insulation

Label	Structure	T, °C	Cycles	Comments
ATO1	AlO/ATO/AlO (A:T=1:3)	150	50/400/50	Conductive even after multiple annealing attempts
ATO5	AlO/ATO/AlO (A:T=1:3)	150	200/600/200	Annealing at 300 °C for 3 hours, bubbles. High leakage current even before zipping
ATO6	AlO/ATO (A:T=1:3)	150	200/400	Annealing at 300 °C for 3 hours. Significant charging. Breaks down around 120 V
ATO7	AlO/ATO (A:T=1:4)	150	100/380	Annealing at 200 °C for 3 hours. After few weeks moderate leeking. Multiple annealing and tests, after last breaks down around 100 V.
ATO8	AlO/ATO (A:T=1:3.5)	150	150/400	Annealing at 200 °C for 3 hours. Breaks down around 100 V. Multiple annealing and tests
ATO9	AlO/ATO (A:T=1:3)	220	200/400	Multiple annealings and tests. After 300 °C for 3 hours leakage became very low. Significant charging, breaks down above 120 V
ATO10	AlO/ATO (A:T=1:10)	150	100/200	Multiple annealings and tests. Charging. Breaks down around 100 V.
ATO11	AlO/ATO (A:T=1:10)	150	100/200	Annealing at 200 °C for 6 hours

AlO – dielectric layer consisting of only Al_2O_3 oxide;
ATO – laminate layer consisting of interchanging Al_2O_3 and TiO_2 oxides.

variety of experiments to measure charge transfer and leakage current. However, these annealing steps occasionally resulted in bubbles appearing on the oxide film after heat exposure, likely due to water trapped in the films during deposition. Notes on the different dielectric laminates fabricated are included in Table 6.4.

6.3 Experimental setup

For this characterization method, an experimental test setup was built as shown in Figure 6.2. The reference resistor was chosen to optimize sensitivity, a function generator (AFG3022C from Tektronix) was used to provide the constant rate spike input, and was controlled from MATLAB. An oscilloscope (MD4054-3 from Tektronix) was used to measure voltages V_2 as well as V_1 used to compute the current and charge transferred to and from the actuator. The amplifying circuit was a custom design to provide amplification over the high bandwidth required for testing. The high temporal resolution of the oscilloscope enabled the capture of device dynamics and charge transfer at very high speeds.

6.3.1 Ramp Tests

For ramp tests, a controlled constant rate spike (e.g., Figure 6.4) was applied to the DUT. The maximum voltage varied between tests, but primary voltages of interest are voltages below and above pull-in. Voltages below pull-in should provide results similar to the quasistatic measurements made in Chapter 4 while voltages above pull-in should provide more insights into the actuator's dynamics.

During the ramp-up phase, it is expected that a constant voltage V_1 will be measured due to the constant slope ramp (6.1). During the second phase, voltage V_1 returns to zero as the input voltage V_2 is constant, but the actuator has not yet moved. During a third phase, the actuators move and zip together. A high V_1 in this phase is indicative of more charge

transfer to the actuator (6.2 and 6.3). A larger charge transfer in this phase would indicate more electrostatic force. We will define this charge as 'max charge' as well as any charge lost and not returned (due to leakage current or trapping) as 'residual charge.'

6.3.2 Leakage Current

The leakage current was defined as current flowing through the reference resistor when the applied voltage is constant and the actuator is at steady state. Since the the zero level voltage, V_0, at V_2 fluctuated from test to test, leakage current at a particular input voltage (V_2^{DC}) was calculated as

$$I_{\mathrm{leak}}(V_2^{\mathrm{DC}}) = \frac{V_1(V_2^{\mathrm{DC}}) - V_0(V_2^{\mathrm{DC}} \equiv 0)}{R_{\mathrm{m}}}. \tag{6.4}$$

To identify possible semiconductor effects such as voltage barriers, different polarities of the input voltage were applied to the actuator during leakage current tests. In the results below, all polarities are positive unless otherwise indicated with a negative sign.

6.4 Results

6.4.1 Actuator dynamics

6.4.1.1 Actuator dynamics due to different etch profiles

To start, the same zipping actuator was compared from the two different wafers at voltages below pull-in and higher than pull-in (pull-in voltage $\approx 72\,\mathrm{V}$). A comparison of

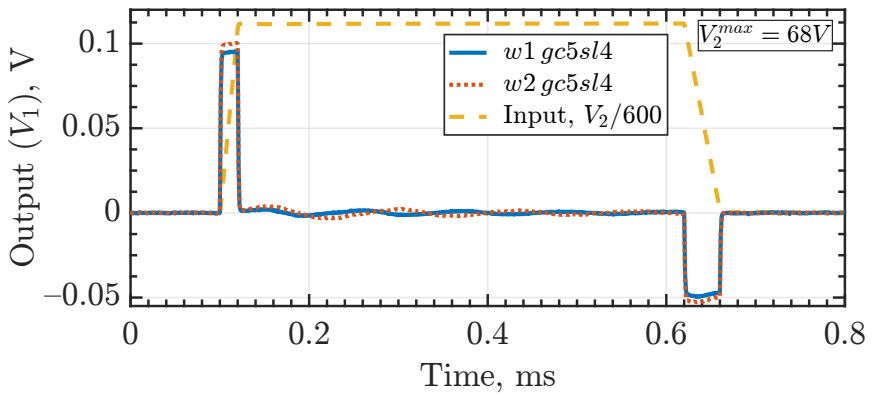

Figure 6.7: Comparison of ramp test data for GCAs of the same design but from different wafers. Small input amplitude condition, no zipping. ($gc5sl4$, $w1$ vs $w2$, input voltage V_2 is scaled down, pull-in voltage $\approx 72\,\mathrm{V}$)

ramp test data in the two different zipping actuators at an input voltage lower than pull-in is provided in Figure 6.7. At 100 µ sec, the input voltage linearly increases for 20 µ sec. Since the rate of voltage increase is constant, the voltage measured across R_m is approximately the same for both devices and constant as expected. Small oscillations once the input voltage has hit its maximum value are likely indicative of small movements in the actuator. When the input voltage is ramped down to zero again over 40 µ sec, the voltage measured across R_m is once again approximately the same for both devices and constant as expected. The difference in magnitude for ramp up and ramp down are due to the differing rates used for both.

Results are far more interesting when the actuators are actuated above their pull-in voltage causing zipping actuation. Figures 6.8 and 6.9 (zoomed version of first 100 µ sec) demonstrate several phases of the actuator's response to the applied voltage. In the first stage, the input voltage linearly increases at a rate far exceeding the actuator's reaction

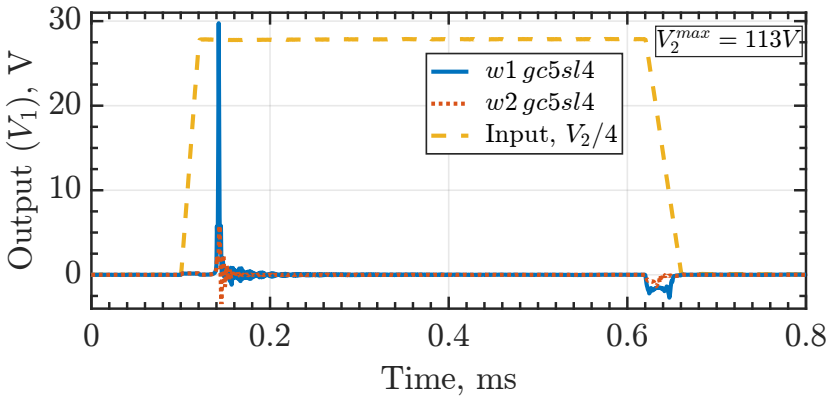

Figure 6.8: Comparison of ramp test data at GCAs of the same design but from different wafers. High input amplitude condition, zipping actuation. ($gc5sl4$, $w1$ vs $w2$, input voltage V_2 is scaled down, pull-in voltage ≈ 72 V)

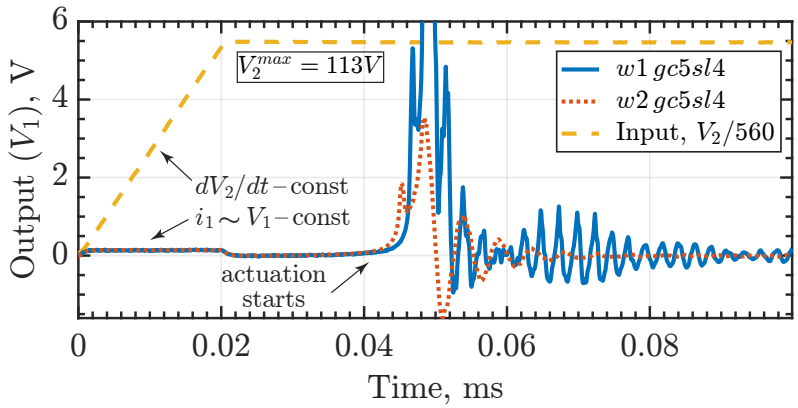

Figure 6.9: Ramp tests data: comparison of the response during actuation phase. $gc5sl4$ GCAs from $w1$ and $w2$ wafers.

speed. There is no actual displacement during this phase and the current through the reference resistor charges the initial actuator capacitance (including any parasitic capacitances in the test setup). Since the capacitance is constant, the current is roughly constant too in agreement with the basic RC circuit model (this is more clear in Figure 6.7).

In the second stage, the voltage is at its maximum (which is higher than actuator's pull-in voltage) and voltage V_1 returns to zero, but the actuators still don't move (which

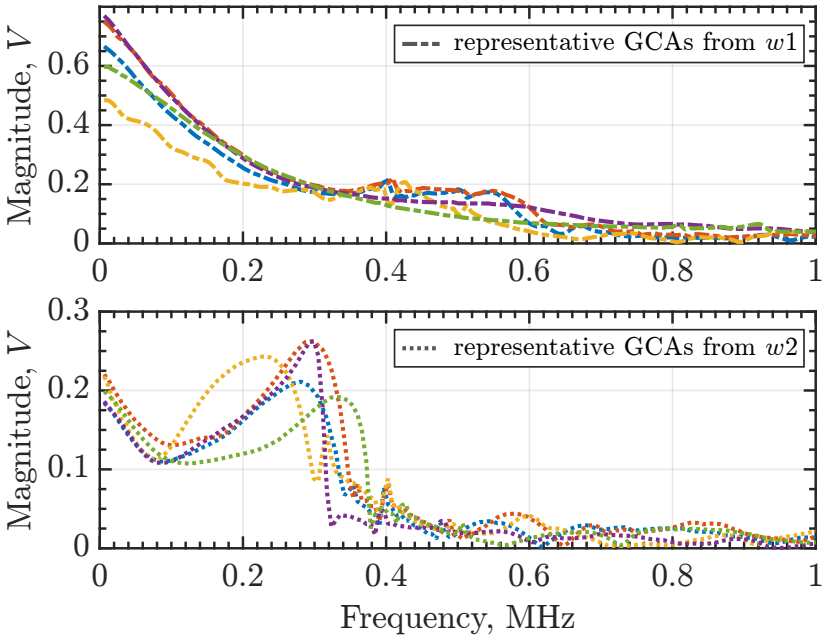

Figure 6.10: Fourier transform of GCAs response upon actuation in ramp tests

would be indicated by fluctuations in V_1). Experiments showed that the duration of this phase depends on the voltage amplitude which indicates that it most likely depends on the ability of the electrostatic force to move the inertia of the actuator.

In the third stage, the actuators move, engage, and zip with the opposite fixed electrodes. In this stage, the response of the actuators from the two different wafers ($w1$ and $w2$) is drastically different. The actuator from $w1$ demonstrates a higher voltage change across the reference resistor that lasts longer than the change in $w2$ corresponding to both a higher current and a higher charge transferred to the actuator. This indicates higher electrostatic force. Significant ringing occurs after 60 µsec indicating charge transfer to and from the actuator.

The actuator from $w1$ also shows oscillations around zero voltage after the two elec-

trodes engage while damped oscillations are only seen in $w2$ during engagement. Because these oscillations are symmetric around zero, charge is being transferred back and forth from the actuator to the power supply indicating no useful force generation. Figure 6.10 illustrates the difference between the oscillations in the actuators from $w1$ and $w2$ using the FFT of the voltage. Actuators from $w1$ exhibit a pronounced maximum in the vicinity of 300 kHz, whereas actuators from $w2$ demonstrate generally decreasing trend for higher frequencies.

The working hypothesis regarding these oscillations in $w1$ actuators is that the zipped electrodes are undergoing torsional vibrations. In a deep reactive ion etched trench, the gap between opposite electrodes can vary through the thickness of the silicon layer – a re-entrant or 'v' profile. If the sidewalls of the electrodes are not perfectly parallel, the engagement of the electrodes becomes nonuniform and a small gap can remain even when the electrodes are fully zipped. Consequently, when electrodes engage at high speed, this gap allows for torsional vibrations (or ringing) resulting in the change of capacitance and charge oscillations that were recorded in Figure 6.9.

Another possible explanation for the observed ringing in $w1$ is contact bounce similar to the phenomenon detected in switches when toggled. To try to validate this possible motion, high-speed and stroboscopic videos were captured, but neither provided any evidence of electrode bouncing. The electrode engagement phase seemed clean, but the return demonstrated some oscillations. These were not as obvious in the ramp tests (ramp down), probably due to much lower variation in capacitance. Of course capturing 300 kHz dynamics on high-speed video was nearly impossible, but stroboscopic recordings provided some

insight into the transient dynamic effects.

The oscillations captured by this characterization method are particularly interesting due to their affect on the force characteristics of the actuators. The drastic difference in charge delivered to actuators from $w1$ and $w2$ was unexpected since the manufacturing steps were identical but performed on different equipment. A visual check of the devices as well as various test features designed to track the progress of the deep reactive ion etch did not raise any initial concerns. Also, a quasistatic view of actuation in $w1$ and $w2$ actuators was similar although at slightly different pull-in voltages which is not unusual.

Given the microscopic scale of these actuators, a detailed nondestructive inspection of the gaps between electrodes is limited to a scanning electron micrograph (SEM). However, the high aspect ratio of trenches makes it almost impossible to view the bottom of the trenches. In addition, detection of a slight slope or thickness difference on the order of 1 µm on a slender freestanding feature carries a lot of practical challenges (resolution, scallops, clean cross-section, perpendicularity of the camera view to the cross-section, etc.) which ultimately reduces the accuracy of these measurements. These results affirm the necessity for a characterization method like this one to evaluate a fabricated actuator's transient performance.

6.4.1.2 Rigid versus zipping actuator dynamics

The previous results demonstrated how a change in etch profile can result in dramatically different transient responses and charge transfer in zipping actuators. As a sanity

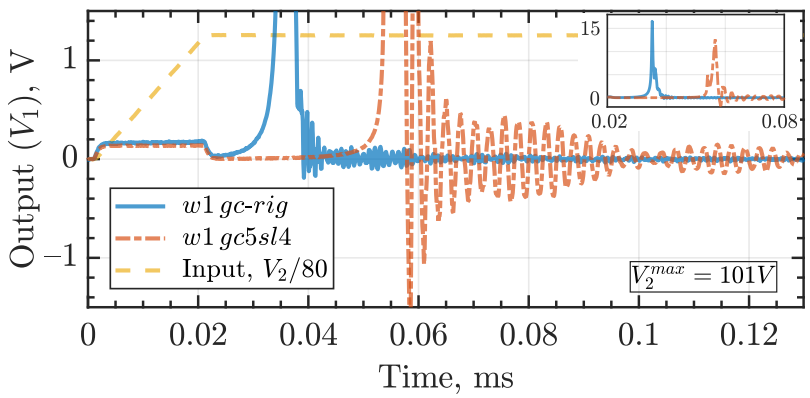

Figure 6.11: Ramp tests data: comparison of the response from zipping and rigid GCAs (both are $w1$ and AlO1)

check, the performance of a zipping actuator is also compared to a more traditional rigid electrode gap closing actuator (Figure 6.11). The inset plot shows the magnitude difference between the two responses. The higher output voltage measured in the rigid actuator for approximately the same duration indicates higher capacitance and output force in this rigid actuator. While output force is challenging to measure directly without calibrated spring constants, a disengagement force for each actuator was measured in a separate experiment (Chapter 4). The disengagement force for the rigid actuator was measured at approximately 11 mN versus approximately 4 mN for the zipping actuator at the same applied voltages in these tests, in part confirming the expected force output from the voltage changes in Figure 6.11.

This figure also shows that the rigid actuator was much faster than the zipping actuator and experienced fewer oscillations. The speed can be partly attributed to the fact that the zipping actuators were longer (600 µm vs 500 µm) and therefore had greater mass. Another contributing factor is the higher electrostatic force resulting in a higher actuator acceleration.

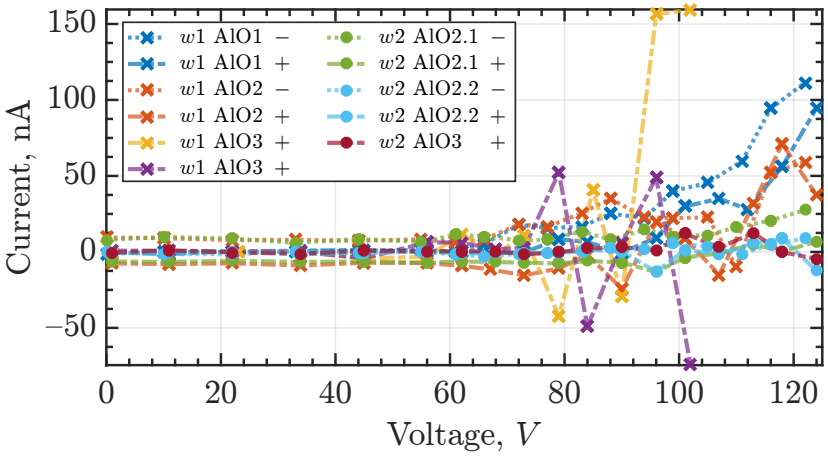

Figure 6.12: Leakage current in actuators as a function of applied voltage. Tests from $w1$ and $w2$ wafers, and several homogeneous (Al_2O_3) dielectric films are included. '+' and '–' signs indicate polarity of applied voltage

Given that the electrodes of the rigid actuator did not come into contact and the small gaps result in a relatively high damping environment, the lack of oscillations in the rigid electrode actuator is not a surprise.

6.4.2 Leakage Current

Figure 6.12 demonstrates changes in leakage current as a function of applied voltage in GCAs with homogeneous dielectric films. The measurements were performed during cyclic/periodic ramp tests. Voltage at the beginning of a cycle (Figure 6.8) was used as a zero level (V_0). A large number of data points ($> 1 \cdot 10^3$) right before the ramp down (Figure 6.8) were averaged to obtain the output voltage for the corresponding constant input V_2^{DC} from 6.4. It should be noted that even though the entire input signal is clearly not constant, the duration and location of the selected data points was chosen to guarantee

the absence of dynamics influence. Thus, the maximum input voltage after ramp up was kept constant long enough ($> 200\,\mu s$) for all mechanical and electrical transient oscillations to decay. The same holds for the zero level voltage data points.

Several observations can be made from the plot (Figure 6.12). To start with, the current only marginally changes until the pull-in voltage ($\approx 70\,V$) when the electrodes engage in contact. Even though (6.4) accounts for the varying zero level voltage, in several tests a constant but measurable current is still present up to the pull-in limit. This is most probably the result of residual charge in the DUT or noisy fluctuations in the measurement circuit since that voltage signal was on the edge of equipment resolution/sensitivity.

Figure 6.12 includes tests with different polarity of the input voltage (same color and marker, dotted vs dash-dot line, signs '+' and '–' indicate the actual polarity). These tests were performed to identify possible semiconductor effects such as voltage barriers. Even though some difference in the magnitude of leakage current and the observed pull-in limit was present, it was not significant and can be explained by the measurement distribution from test to test and rather small magnitude of the measured values ($< 200\,nA$). Various phenomena influenced the measurements accuracy due to the sensitive nature of GCAs including the history of previous tests (due to charging), time since annealing, any particles attracted by high electric field, etc.

After earlier findings, it is not a surprise to observe the different behavior between $w1$ and $w2$ leakage curves (set apart by markers in Figure 6.12). In GCAs from $w2$ the leakage did not exceed $30\,nA$ even at their peak and demonstrated rather gradual increase with

applied voltage. In $w1$ actuators, on the other hand, the leakage current demonstrated clear exponential increase after pull-in and the current magnitude rose above 150 nA. Considering that this difference was consistent in all tested actuators with various homogeneous ALD films, the effect of dielectric can be ruled out. However, the discrepancy in leakage current perfectly fits with the sloped walls reasoning described in Chapter 5. Non-vertical sidewalls lead to lower contact area which consequently results in reduced leakage current (using the common assumption that average current area density is constant).

Another peculiar behavior in leakage curves especially noticeable in $w1$ devices was erratic bounces of current measurements even within one DUT and test. In some cases the bounces were large enough to change polarity even though the applied voltage stayed the same sign. The nature of this behavior is still unclear however the fact that all erratic curves were obtained from DUTs with the thickest oxide (AlO3) points to the dielectric charging issue. In all ramp tests the measurements were done by incrementally increasing the maximum voltage and cycling the actuator to get to the stable regime. In DUTs that demonstrated charging, the number of test cycles was limited due to gradual charge accumulation resulting in inconsistent behavior. Therefore between each ramp test the DUT was cycled with high frequency, large amplitude sine signal to reset the DUT. This method was demonstrated to be effective but not to the extent of an anneal for several hours. The residual trapped charge in the dielectric (volume, surface, or interface) can be responsible for the leakage current swings and its polarity changes. Also, considering that the magnitude of leakage current in Figure 6.12 is several orders of magnitude smaller than one during charging and

discharging GCAs, the change of polarity can be a result of an unidentified zero level shift of the amplifying and/or measurement circuit.

Figure 6.12 reports only on GCAs with homogeneous dielectric films deposited using ALD. The material in all these films was Al_2O_3, and the differences between each film are described in Table 6.3. The majority of these films demonstrated diminishing returns for breakdown and leakage characteristics with increasing oxide layer thickness. The trapped charge effects, on the other hand, showed exponential increase with oxide growth. These effects were mostly pronounced in shift of pull-in and disengage voltage levels which in the extreme cases led to the disengage failure (using only the restoring forces of flexures) and even to actuator movement in the opposite direction.

As a rough rule during all tests, DUTs with AlO1 (800 cycles) showed minimal charging effect up to the breakdown limit (120 V), DUTs with AlO3 (1200 cycles) demonstrated some charging in the main test range (up to 120 V) which prompted pull-in voltage increase but not the disengage failure. DUTs with AlO4 (1600 cycles) were too susceptible to charging to be used or even tested since the GCA disengage had to always be manual. The tests showed that other parameters of ALD process also impacted the characteristics of the ALD films. The majority of tests (including all of the above) were done with homogeneous Al_2O_3 dielectrics deposited at 150 °C using trimethylaluminium (TMA) and deionized (DI) water as precursors. Experiments with higher deposition temperatures (220 °C) or different precursors (TMA and ozone) showed comparable breakdown properties but significantly larger charging effects. Moreover, the charge accumulation process was much faster which often resulted in

spontaneous disengagement (shortly after zipping) even when the actuated voltage was still applied. The exact (or even rough) explanation of these results is beyond the scope of this work.

An important conclusion from these observations is the inability to arbitrarily increase the oxide film thickness to operate at very high actuation voltages without breakdown. There is an optimal dielectric film thickness that enables highest actuation voltage with minimal trapped charge.

6.4.2.1 Transferred Charge in Ramp Tests

Another method to examine charge lost to leakage current or trapping is through measurement of the charge transferred during various phases of the constant rate spike. Figure 6.13 shows a comparison of charge transfer to GCAs of the same design but from the two different wafers, w_1 and w_2. This particular figure uses a V_2^{max} below pull-in. The curves trace a loop. Charge increases as a higher voltage is applied and then continues to increase a bit as V_2 is held constant (best seen in the dotted orange curve for w_2). As voltage is ramped back down, charge is returned to the power supply.

Similar to the drastic differences seen between wafers in Figure 6.8, the same difference is seen when V_2^{max} is above pull-in in Figure 6.14. In this case, charge from w_1 is much higher, indicating a higher force. However, more charge is also lost in this case due to the greater hysteresis in the w_1 curve.

This same data is presented in a slightly different way in Figure 6.15. In this case,

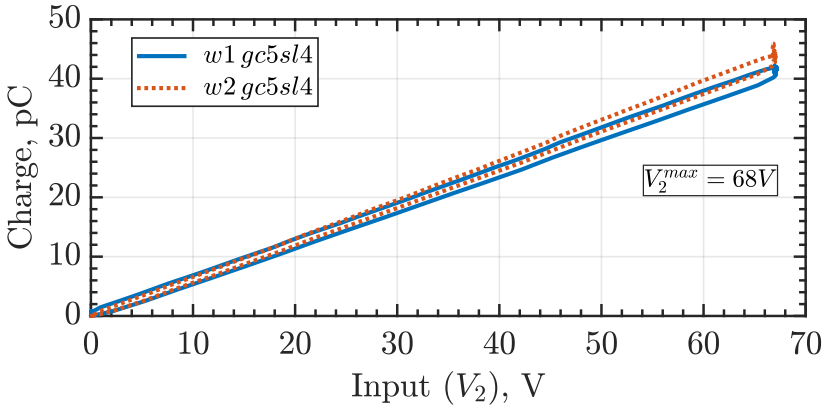

Figure 6.13: Comparison of charge transfer to GCAs of the same design but from different wafers. Ramp tests, small input amplitude condition, no zipping. The same data as in Figure 6.7

various ALD laminates are also compared. In the max charge plot, all of the actuators from w_1 have a higher max charge than any actuators from w_2. Within w_1 wafers, certain laminates like AlO3 show exceptionally high max charge, but they also have very high residual charge. Actuators from w_2 are more consistent. Despite the fact that they have a lower max charge, they also have a relatively low residual charge. These results can provide insights into force and efficiency for future actuator designs.

6.5 Conclusions

This chapter describes a new characterization method to capture the fast dynamics of electrostatic actuators, and zipping actuators in particular. The characterization method is used to explore the effects of different etch parameters and dielectrics used in zipping actuators. Actuator force is captured through measurement of charge transfer, and current measurement is also used to capture data on leakage current which ultimately provides a

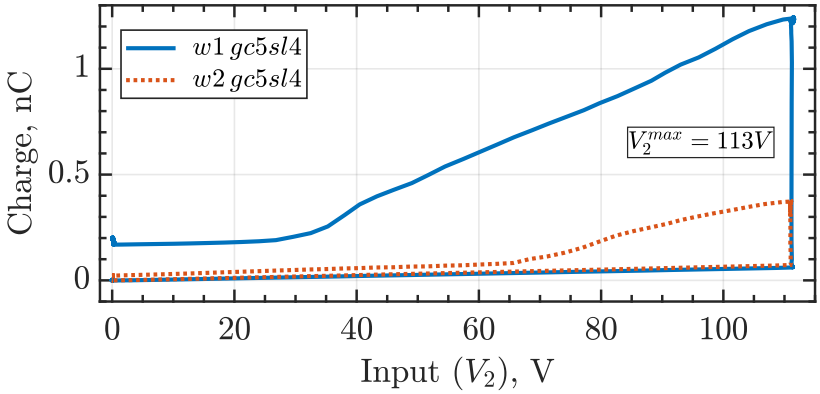

Figure 6.14: Comparison of charge transfer to GCAs of the same design but from different wafers. Ramp tests, high input amplitude condition, zipping actuation. The same data as in Figure 6.8

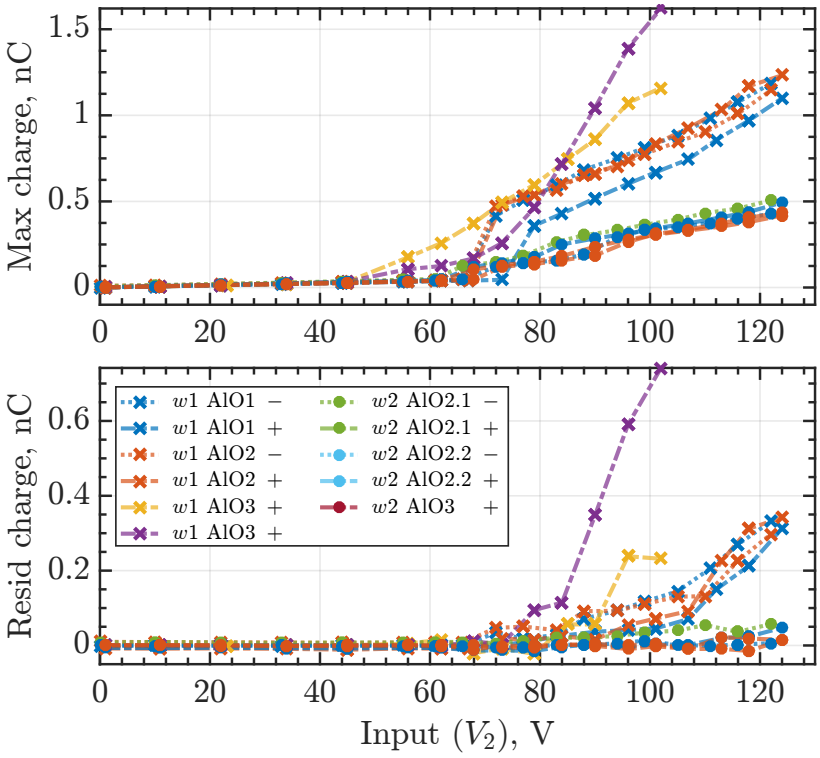

Figure 6.15: Maximum and residual charge in GCAs as a function of applied voltage. The same data as in Figure 6.12

measure of actuator efficiency. Results were used to demonstrate interesting underdamped dynamics in an actuator presumed to have a greater slope in its etch profile. Leakage current measurements demonstrated the significant influence that both sidewall profile and dielectric thickness have on actuator efficiency.

Chapter 7

Conclusions

7.1 Summary

This work in the design and fabrication of electrostatic inchworm motors has led to significant progress in the force density available from these motors. A telling metric is that these motor designs have been integrated into millirobotic systems designed in other groups (e.g., [21,22]). While the motors did not ultimately achieve the estimated force metrics, new techniques for characterizing force output and efficiency from the motors were developed to help diagnose these problems.

7.2 List of Contributions

The primary contributions of the this work are summarized as follows:

- A new design for electrostatic inchworm motors that incorporate a flexible driving arm to improve both force density and efficiency. Designs were optimized and validated.
- A novel technique to characterize force output from electrostatic actuators by measuring changes in capacitance. This technique allows for pure electrical characterization of motors in contrast to the requirement for calibrated springs in previous work. This technique was validated on both passive components as well as three different types of

electrostatic actuator.

- New electrostatic actuator designs and models that take advantage of compliant electrodes. These actuator designs were fabricated and compared using both the electrical characterization described above and a novel electromechanical characterization that measured both disengagement force and returned charge during actuator disengagement.

- Another new electrical characterization technique using constant rate spikes to characterize the fast dynamics of electrostatic pull-in validated on both rigid electrode and zipping actuators.

7.3 Future Directions

One of the most significant conclusions from this work is the recognition that fabrication processes need to be improved to obtain straight sidewalls for electrostatic actuators like these to reach their potential for generating force. As fabrication processes are constantly being improved, there may still be hope for both the thick-film and compliant electrode electrostatic actuator designs to achieve the kind of forces estimated in theory. However, as is evident from Figure 5.17 even on 40 µm SOI wafer slope of the sidewalls becomes huge detriment for zipping actuators. Basically, the thinner is dielectric layer between electrodes in zipping GCA, the bigger is influence of the fabrication quality. One of the methods of solving this issue would be developing good quality conformal dielectric layers that can be

uniformly applied in the high aspect ratio trenches.

Another problem of the electrostatic inchworm motors that needs to be solved for high force applications is high yield of the manufacturing process. The higher the force GCA needs to produce, the higher area it usually occupies. In case of thick film GCAs the area reached 10s of mm^2. The problem is the fact that entire inchworm motor has to work as one mechanism, all pieces of which perform as designed. So even if one submicron particle gets in the photoresist layer and disturbs the trench between one pair of interdigitated fingers, the entire motor is rendered malfunctioning.

If the manufacturing problems are solved, the zipping actuators with low slopes show good plromise and can perform better than rigid gap closing actuators. It is also still important to better integrate microfabricated actuators into increasingly complex microrobotic mechanisms. The inchworm motors demonstrated good robustness during tests except the case with very high or dynamic loads. Such loads as release of the shuttle after maximum load tests or drop of the manufactured die often broke some of the supporting flexures, rendering the entire motor inoperable.

In addition, there are many other millirobotic mechanisms that would be appropriate for these electrostatic inchworms. As one example, a wire climbing robot could be designed. The original design of the through-wafer motor intended to transfer force to the target by pushing the shuttle out. After actuation the shuttle's position is restored with the return springs. Alternatively, the shuttle can be replaced by a long thin cable with a diameter similar to that of the shuttle. In this case, the motor will be climbing along the cable. Considering

a conservative estimate of the motor's force (0.27 N), the motor can lift a total weight of 27 g. This payload is plenty to carry the motor ($\ll$1 g), a motor driver ($\ll$1 g, [64,81]), and a battery (1 g, [82]) for an autonomous wire ascend.

7.4 List of publications

7.4.1 First author publications:

- I. Penskiy and S. Bergbreiter, "Optimized electrostatic inchworm motors using a flexible driving arm," Journal of Micromechanics and Microengineering, vol. 23, no. 1, p. 015018, Jan. 2013.
- I. Penskiy, P. D. Samuel, J. S. Humbert, and S. Bergbreiter, "A bio-inspired active tail control actuator for nano air vehicles," in IEEE International Conference on Robotics and Automation, Minneapolis, MN, 2012, pp. 4635-4640.
- I. Penskiy, A. P. Gerratt, and S. Bergbreiter, "Friction, adhesion, and wear properties of PDMS coatings in MEMS devices," in 2011 IEEE 24th International Conference on Micro Electro Mechanical Systems, Cancun, Mexico, 2011, pp. 440-444.
- I. Penskiy, A. P. Gerratt, and S. Bergbreiter, "Efficient electrostatic inchworm motors with simple control and high force density," in Transducers, Beijing, 2011.
- I. Penskiy, A. P. Gerratt, and S. Bergbreiter, "Friction, adhesion, and wear properties of PDMS coatings in MEMS devices," in Micro Electro Mechanical Systems (MEMS),

2011 IEEE 24th International Conference on, 2011, pp. 440-444.

- I. Penskiy, A. P. Gerratt, and S. Bergbreiter, "Friction, adhesion and wear properties of PDMS films on silicon sidewalls," Journal of Micromechanics and Microengineering, vol. 21, p. 105013, Oct. 2011.

Other publications:

- H.-S. Shin, A. Charalambides, I. Penskiy, and S. Bergbreiter, "A soft microfabricated capacitive sensor for high dynamic range strain sensing," in IEEE/RSJ International Conference on Intelligent Robots and Systems, Daejeon, South Korea, 2016.

- C. Lawler, I. Penskiy, A. Sirken, and S. Bergbreiter, "Using light fields for rapid manipulation of millirobot swarms," in International Symposium on Experimental Robotics, Tokyo, 2016.

- B. N. Ranganathan, I. Penskiy, W. Dean, S. Bergbreiter, and J. S. Humbert, "Bio-inspired wind frame state sensing and estimation for MAV applications," in IEEE/RSJ International Conference on Intelligent Robots and Systems, 2015, pp. 2729-2735.

- Y. Tang, C. Chen, A. Khaligh, I. Penskiy, and S. Bergbreiter, "An Ultracompact Dual-Stage Converter for Driving Electrostatic Actuators in Mobile Microrobots," IEEE Transactions on Power Electronics, vol. 29, no. 6, pp. 2991-3000, Jun. 2014.

- A. P. Gerratt, B. Balakrisnan, I. Penskiy, and S. Bergbreiter, "Dielectric elastomer actuators fabricated using a micro-molding process," Smart Materials and Structures, vol. 23, no. 5, p. 055004, May 2014.

- A. P. Gerratt, I. Penskiy, and S. Bergbreiter, "In situ characterization of PDMS in SOI-MEMS," Journal of Micromechanics and Microengineering, vol. 23, no. 4, p. 045003, 2013.

- A. P. Gerratt, I. Penskiy, and S. Bergbreiter, "In situ characterization of PDMS in SOI-MEMS," Journal of Micromechanics and Microengineering, vol. 23, no. 4, p. 045003, Apr. 2013.

- C. Casarez, I. Penskiy, and S. Bergbreiter, "Using an inertial tail for rapid turns on a miniature legged robot," in IEEE International Conference on Robotics and Automation, Karlsruhe, Germany, 2013, pp. 5469-5474.

- E. Schaler, M. Tellers, A. Gerratt, I. Penskiy, and S. Bergbreiter, "Toward fluidic microrobots using electrowetting," in IEEE International Conference on Robotics and Automation, 2012, pp. 3461-3466.

- A. Gerratt, B. Balakrisnan, I. Penskiy, and S. Bergbreiter, "Batch fabricated bidirectional dielectric elastomer actuators," in Solid-State Sensors, Actuators and Microsystems Conference (TRANSDUCERS), 2011 16th International, 2011, pp. 2422-2425.

- A. P. Gerratt, B. Balakrisnan, I. Penskiy, and S. Bergbreiter, "Batch fabricated bidirectional dielectric elastomer actuators," in Transducers, Beijing, 2011, pp. 2422-2425.

- A. P. Gerratt, I. Penskiy, and S. Bergbreiter, "Integrated Silicon-PDMS Process for Microrobot Mechanisms," in IEEE International Conference on Robotics and Automation, Anchorage, AK, 2010. **Best Conference Paper Award**

- A. P. Gerratt, I. Penskiy, and S. Bergbreiter, "SOI-elastomer process for energy storage and rapid release," Journal of Micromechanics and Microengineering, vol. 20, no. 10, p. 104011, Oct. 2010.

- A. P. Gerratt, I. Penskiy, and S. Bergbreiter, "SOI-elastomer process for energy storage and rapid release," J. Micromech. Microeng., vol. 20, no. 10, p. 104011, Oct. 2010.

- A. P. Gerratt, I. Penskiy, and S. Bergbreiter, "Integrated silicon-PDMS process for microrobot mechanisms," in Robotics and Automation (ICRA), 2010 IEEE International Conference on, 2010, pp. 3153-3158.

- A. P. Gerratt, I. Penskiy, and S. Bergbreiter, "High Power Micromechanical Thrusters with Embedded Elastomer," in PowerMEMS, Washington DC, 2009.

Patents:

- A. Charalambides, I. Penskiy, and S. Bergbreiter, All-elastomer 3-axis contact resistive tactile sensor arrays and micromilled manufacturing methods thereof, US Patent No. 9,868,217 (issued).

Bibliography

[1] Jian Li. *Electrostatic zipping actuators and their applications to MEMS*. PhD thesis, Massachusetts Institute of Technology, 2004.

[2] M. Hirose and K. Ogawa. Honda humanoid robots development. *Philosophical Transactions of the Royal Society A: Mathematical, Physical and Engineering Sciences*, 365(1850):11–19, January 2007.

[3] William Bluethmann, Robert Ambrose, Myron Diftler, Scott Askew, Eric Huber, Michael Goza, Fredrik Rehnmark, Chris Lovchik, and Darby Magruder. Robonaut: A robot designed to work with humans in space. *Autonomous robots*, 14(2-3):179–197, 2003.

[4] Ronald S. Fearing. Challenges for Efffective Millirobots. In *Micro-NanoMechatronics and Human Science, 2006 International Symposium on*, pages 1–5. IEEE, 2006.

[5] S. Bergbreiter. *Autonomous Jumping Microrobots*. Ph.D., University of California, Berkeley, December 2007.

[6] B.A. Warneke, M.D. Scott, B.S. Leibowitz, Lixia Zhou, C.L. Bellew, J.A. Chediak, J.M. Kahn, B.E. Boser, and K.S.J. Pister. An autonomous 16 mm3 solar-powered node for distributed wireless sensor networks. In *Proceedings of IEEE Sensors, 2002*, volume 2, pages 1510–1515 vol.2, 2002.

[7] A. Dighe, U.P. Froriep, M. Sunshine, P. Anikeeva, C. Moritz, and C. Voldman. Development and in Vivo Testing of Reconfigurable Neural Probes for Chronic Electrical Recording. In *A Solid-State Sensors, Actuators and Microsystems Workshop*, Hilton Head USA, June 2014.

[8] Nathan Jackson, Arati Sridharan, Sindhu Anand, Michael Baker, Murat Okandan, and Jit Muthuswamy. Long-Term Neural Recordings Using MEMS Based Movable Microelectrodes in the Brain. *Frontiers in Neuroengineering*, 3, June 2010.

[9] Anubhav Arora, Itzhak Hakim, Joy Baxter, Ruben Rathnasingham, Ravi Srinivasan, Daniel A. Fletcher, and Samir Mitragotri. Needle-free delivery of macromolecules across the skin by nanoliter-volume pulsed microjets. *Proceedings of the National Academy of Sciences*, 104(11):4255–4260, 2007.

[10] R B Bhisitkul and C G Keller. Development of Microelectromechanical Systems (MEMS) forceps for intraocular surgery. *The British Journal of Ophthalmology*, 89(12):1586–1588, December 2005.

[11] C. Bergeles and Guang-Zhong Yang. From Passive Tool Holders to Microsurgeons: Safer, Smaller, Smarter Surgical Robots. *IEEE Transactions on Biomedical Engineering*, 61(5):1565–1576, May 2014.

[12] Kevin R. Cochran, Lawrence Fan, and Don L. DeVoe. High-power optical microswitch based on direct fiber actuation. *Sensors and Actuators A: Physical*, 119(2):512–519, April 2005.

[13] Martin Hoffmann, Dirk NÃ¼sse, and Edgar Voges. Electrostatic parallel-plate actuators with large deflections for use in optical moving-fibre switches. *Journal of Micromechanics and Microengineering*, 11(4):323, 2001.

[14] Ryan St. Pierre and Sarah Bergbreiter. Toward Autonomy in Sub-Gram Terrestrial Robots. *Annual Review of Control, Robotics, and Autonomous Systems*, 2(1):231–252, May 2019.

[15] M. Karpelson, G.Y. Wei, and R.J. Wood. A review of actuation and power electronics options for flapping-wing robotic insects. In *IEEE International Conference on Robotics and Automation*, pages 779–786, 2008. read.

[16] R. S Fearing. Powering 3 dimensional microrobots: power density limitations. *Tutorial on Micro Mechatronics and Micro Robotics, ICRA*, 98, 1998.

[17] T. Ebefors, J.U. Mattsson, E. Kalvesten, and G. Stemme. A Walking Silicon Micro-Robot. In *10th International Conference on Solid State Sensors ans Actuators*, pages 1202–1205, Japan, June 1999.

[18] Richard Yeh. *Articulated Mechanisms and Electrostatic Actuators for Autonomous Microrobots*. PhD thesis, University of California, Berkeley, 2001.

[19] Seth Hollar. *A SolarÂPowered, Milligram Prototype Robot from a ThreeÂChip Process*. PhD thesis, University of California, Berkeley, 2003.

[20] I. Penskiy and S. Bergbreiter. Optimized electrostatic inchworm motors using a flexible driving arm. *Journal of Micromechanics and Microengineering*, 23(1):015018, January 2013.

[21] Joseph Greenspun and Kristofer S. J. Pister. First leaps of an electrostatic inchworm motor-driven jumping microrobot. In *Hilton Head Solid-State Sensors, Actuators, and Microsystems Workshop*, 2018.

[22] D.S. Contreras and K. S. J. Pister. A six-legged MEMS silicon robot using multichip assembly. In *Hilton Head Solid-State Sensors, Actuators, and Microsystems Workshop*, Hilton Head Island, SC, June 2018.

[23] Aaron P. Gerratt. *SILICON AND POLYMER COMPONENTS FOR MICROROBOTS*. Doctor of Philosophy, University of Maryland, College Park, 2013.

[24] Jeffrey S. Pulskamp, Ronald G. Polcawich, and Kenn Oldham. Highly integrated PiezoMEMS enabled millimeter-scale robotics. In *ASME 2009 International Design Engineering Technical Conferences and Computers and Information in Engineering Conference*, pages 797–805. American Society of Mechanical Engineers, 2009.

[25] Justin Daminabo Pearse. *Towards the use of dielectric elastomer actuators as locomotive devices for millimeter-scale robots.* Master of Science, University of Maryland, College Park, 2012.

[26] Andrew Cao, Jongbaeg Kim, and Liwei Lin. Bi-directional electrothermal electromagnetic actuators. *Journal of Micromechanics and Microengineering*, 17(5):975–982, May 2007.

[27] Mohsen Shahinpoor. Ionic polymer-conductor composites as biomimetic sensors, robotic actuators and artificial muscles – a review. *Electrochimica Acta*, 48(14-16):2343–2353, June 2003.

[28] R. J. Wood, S. Avadhanula, R. Sahai, E. Steltz, and R. S. Fearing. Microrobot Design Using Fiber Reinforced Composites. *Journal of Mechanical Design*, 130(5):052304–052304, March 2008.

[29] J P Whitney, P S Sreetharan, K Y Ma, and R J Wood. Pop-up book MEMS. *Journal of Micromechanics and Microengineering*, 21(11):115021, November 2011.

[30] Andrew T. Baisch and Robert J. Wood. Pop-up assembly of a quadrupedal ambulatory MicroRobot. In *Intelligent Robots and Systems (IROS), 2013 IEEE/RSJ International Conference on*, pages 1518–1524. IEEE, 2013.

[31] P.S. Sreetharan, J.P. Whitney, M.D. Strauss, and R.J. Wood. Monolithic fabrication of millimeter-scale machines. *Journal of Micromechanics and Microengineering*, 22(5):055027, 2012.

[32] Erik Steltz and Ronald S. Fearing. Dynamometer Power Output Measurements of Miniature Piezoelectric Actuators. *IEEE/ASME Transactions on Mechatronics*, 14(1):1–10, February 2009.

[33] D.J. Bell, T.J. Lu, N.A. Fleck, and S.M. Spearing. MEMS actuators and sensors: observations on their performance and selection for purpose. *Journal of Micromechanics and Microengineering*, 15(7):S153–S164, 2005.

[34] Federico Carpi, Roy Kornbluh, Peter Sommer-Larsen, and Gursel Alici. Electroactive polymer actuators as artificial muscles: are they ready for bioinspired applications? *Bioinspiration & Biomimetics*, 6(4):045006, December 2011.

[35] Hyun-Phill Ko, Hoseop Jeong, and Burhanettin Koc. Piezoelectric actuator for mobile auto focus camera applications. *Journal of Electroceramics*, 23(2-4):530–535, October 2009.

[36] New Scale Technologies. http://www.newscaletech.com/technology/motors-for-oem.php.

[37] R. Yeh, S. Hollar, and K.S.J. Pister. Single mask, large force, and large displacement electrostatic linear inchworm motors. *Journal of Microelectromechanical Systems*, 11(4):330–336, 2002.

[38] W.C. Tang, M.G. Lim, and R.T. Howe. Electrostatic Comb Drive Levitation And Control Method. *Journal of Microelectromechanical Systems*, 1(4):170–178, December 1992.

[39] M.J. Daneman, N.C. Tien, O. Solgaard, A.P. Pisano, K.Y. Lau, and R.S. Muller. Linear microvibromotor for positioning optical components. *Journal of Microelectromechanical Systems*, 5(3):159–165, 1996.

[40] M.A Erismis, H.P Neves, R. Puers, and C. Van Hoof. A Low-Voltage Large-Displacement Large-Force Inchworm Actuator. *Journal of Microelectromechanical Systems*, 17(6):1294–1301, 2008.

[41] S.H. Kim, I.H. Hwang, K.W. Jo, E.S. Yoon, and J.H. Lee. High-resolution inchworm linear motor based on electrostatic twisting microactuators. *Journal of Micromechanics and Microengineering*, 15(9):1674–1682, 2005.

[42] N.R. Tas, T. Sonnenberg, R. Molenaar, and M. Elwenspoek. Design, fabrication and testing of laterally driven electrostatic motors employing walking motion and mechanical leverage. *Journal of Micromechanics and Microengineering*, 13(1):N6–15, 2003.

[43] M. Baltzer, T. Kraus, and E. Obermeier. A linear stepping actuator in surface micromachining technology for low voltages and large displacements. In *1997 International Conference on Solid State Sensors and Actuators*, volume 2, pages 781–784, June 1997.

[44] J.M. Maloney, D.S. Schreiber, and D.L. DeVoe. Large-force electrothermal linear micromotors. *Journal of Micromechanics and Microengineering*, 14(2):226–234, 2004.

[45] C. Arthur, N. Ellerington, T. Hubbard, and M. Kujath. MEMS earthworm: a thermally actuated peristaltic linear micromotor. *Journal of Micromechanics and Microengineering*, 21(3):035022, 2011.

[46] S. Hollar, A. Flynn, S. Bergbreiter, and K.S.J. Pister. Robot Leg Motion in a Planarized-SOI, Two-Layer Poly-Si Process. *Journal of Microelectromechanical Systems*, 14(4):725–740, 2005.

[47] E.S. Hung and S.D. Senturia. Extending the travel range of analog-tuned electrostatic actuators. *Journal of Microelectromechanical Systems*, 8(4):497–505, 1999.

[48] I.W. Rangelow. Critical tasks in high aspect ratio silicon dry etching for microelectromechanical systems. *Journal of Vacuum Science & Technology A: Vacuum, Surfaces, and Films*, 21(4):1550–1562, 2003.

[49] P.M. Osterberg and S.D. Senturia. M-TEST: A test chip for MEMS material property measurement using electrostatically actuated test structures. *Journal of Microelectromechanical Systems*, 6(2):107–118, 2002.

[50] Ching-Heng Chen, J. Andrew Yeh, and Pei-Wang Wang. Electrical breakdown phenomena for devices with micron separations. *Journal of Micromechanics and Microengineering*, 16:1366–1373, 2006.

[51] Takahito Ono, Dong Youn Sim, and Masayoshi Esashi. Micro-discharge and electric breakdown in a micro-gap. *Journal of Micromechanics and Microengineering*, 10(3):445–451, September 2000.

[52] N. D Hoivik, J. W Elam, R. J Linderman, V. M Bright, S. M George, and Y. C. Lee. Atomic layer deposited protective coatings for micro-electromechanical systems. *Sensors & Actuators: A. Physical*, 103(1-2):100–108, 2003.

[53] T.M. Mayer, J.W. Elam, S.M. George, P.G. Kotula, and R.S. Goeke. Atomic-layer deposition of wear-resistant coatings for microelectromechanical devices. *Applied Physics Letters*, 82(17):2883, 2003.

[54] C. Yamahata, E. Sarajlic, G.J.M. Krijnen, and M.A.M. Gijs. Subnanometer Translation of Microelectromechanical Systems Measured by Discrete Fourier Analysis of CCD Images. *Journal of Microelectromechanical Systems*, 19(5):1273–1275, 2010.

[55] J.V. Clark, D. Garmire, M. Last, J. Demmel, and S. Govindjee. Practical Techniques for Measuring MEMS Properties. In *NSTI-Nanotech*, Boston, MA, March 2004.

[56] F.M. Alsaleem, M.I. Younis, and H.M. Ouakad. On the nonlinear resonances and dynamic pull-in of electrostatically actuated resonators. *Journal of Micromechanics and Microengineering*, 19(4):045013, 2009.

[57] V. Milanovic, L. Doherty, D.A. Teasdale, C. Zhang, S. Parsa, V. Nguyen, M. Last, and K.S.J. Pister. Deep reactive ion etching for lateral field emission devices. *Electron Device Letters, IEEE*, 21(6):271–273, 2000.

[58] Gabriel L. Smith, John M. Maloney, Lawrence Fan, and Don L. DeVoe. Large-displacement microactuators in deep reactive ion-etched single-crystal silicon. In Henry Helvajian, Siegfried W. Janson, and Franz Laermer, editors, *MEMS Components and Applications for Industry, Automobiles, Aerospace, and Communication*, volume 4559, pages 138–147. SPIE, October 2001.

[59] M. Chabloz, J. Jiao, Y. Yoshida, T. Matsuura, and K. Tsutsumi. A method to evade microloading effect in deep reactive ion etching for anodically bonded glass-silicon structures. In *Micro Electro Mechanical Systems, 2000. MEMS 2000. The Thirteenth Annual International Conference on*, pages 283–287, 2000. read.

[60] Yuan Li, Zhenchuan Yang, and Guizhen Yan. An improved method to remove anti-footing Al layer after DRIE. In *4th IEEE International Conference on Nano/Micro Engineered and Molecular Systems, 2009. NEMS 2009*, pages 868–871, 2009. read.

[61] Ki Hoon Kim, Sang Cheol Kim, Kyu Yeon Park, and Sang Sik Yang. DRIE fabrication of notch-free silicon structures using a novel silicon-on-patterned metal and glass wafer. *Journal of Micromechanics and Microengineering*, 21(4):045018, April 2011. read.

[62] S.E. Alper, A. Aydemir, and T. Akin. Stepped-etching for preserving critical dimensions in through-wafer deep reactive ion etching of thick silicon. In *Solid-State Sensors, Actuators and Microsystems Conference, 2009. TRANSDUCERS 2009. International*, pages 1110–1113, 2009. read.

[63] Yong-Seok Lee, Yun-Ho Jang, Yong-Kweon Kim, and Jung-Mu Kim. Thermal de-isolation of silicon microstructures in a plasma etching environment. *Journal of Micromechanics and Microengineering*, 23(2):025026, February 2013.

[64] Y. Tang, C. Chen, A. Khaligh, I. Penskiy, and S. Bergbreiter. An Ultra-compact Dual-stage Converter for Driving Electrostatic Actuators in Mobile Microrobots. *IEEE Transactions on Power Electronics*, Early Access Online, 2013.

[65] B.R. Donald, C.G. Levey, C.D. McGray, I. Paprotny, and D. Rus. An untethered, electrostatic, globally controllable MEMS micro-robot. *Microelectromechanical Systems, Journal of*, 15(1):1 – 15, February 2006.

[66] Apex Microtechnology. Apex, PA340 - High Voltage Power Operational Amplifier, 2017.

[67] Benjamin Goldberg. *Gait Studies for a Power and Control Autonomous Legged Microrobot*. PhD Dissertation, Harvard University, Cambridge Mass., July 2017.

[68] Jingyan Dong and Placid M Ferreira. Simultaneous actuation and displacement sensing for electrostatic drives. *Journal of Micromechanics and Microengineering*, 18(3):035011, March 2008.

[69] Jian Li, Michael P. Brenner, Jeffrey H. Lang, Alexander H. Slocum, and Ralf Struempler. DRIE-fabricated curved-electrode zipping actuators with low pull-in voltage. In *TRANSDUCERS, Solid-State Sensors, Actuators and Microsystems, 12th International Conference on, 2003*, volume 1, pages 480–483. IEEE, 2003. zipping.

[70] Seth Hollar, Sarah Bergbreiter, and K. S. J. Pister. Bidirectional Inchworm Motors and TwoÂDOF Robot Leg Operation. In *Transducers*, Boston, MA, 2003.

[71] Seth Hollar, Anita M. Flynn, Colby Bellew, and K. S. J. Pister. Solar powered 10 mg silicon robot. In *IEEE Micro Electro Mechanical Systems*, pages 706–711, 2003.

[72] K.E. Petersen. Dynamic micromechanics on silicon: Techniques and devices. *IEEE Transactions on Electron Devices*, 25(10):1241–1250, October 1978.

[73] Rob Legtenberg, John Gilbert, Stephen D. Senturia, and Miko Elwenspoek. Electrostatic curved electrode actuators. *Microelectromechanical Systems, Journal of*, 6(3):257–265, 1997.

[74] Jian Li, M.P. Brenner, T. Christen, M.S. Kotilainen, J.H. Lang, and A.H. Slocum. Deep-reactive ion-etched compliant starting zone electrostatic zipping actuators. *Journal of Microelectromechanical Systems*, 14(6):1283–1297, December 2005.

[75] Stephen F. Bart, Theresa A. Lober, Roger T. Howe, Jeffrey H. Lang, and Martin F. Schlecht. Design considerations for micromachined electric actuators. *Sensors and Actuators*, 14(3):269–292, July 1988.

[76] Y. Nemirovsky and O. Bochobza-Degani. A methodology and model for the pull-in parameters of electrostatic actuators. *Journal of Microelectromechanical Systems*, 10(4):601–615, December 2001.

[77] Shi-Jin Ding, Hang Hu, Chunxiang Zhu, Sun Jung Kim, Xiongfei Yu, Ming-Fu Li, Byung Jin Cho, D.S.H. Chan, M.B. Yu, S.C. Rustagi, A. Chin, and Dim-Lee Kwong. RF, DC, and reliability characteristics of ALD HfO/sub 2/-Al/sub 2/O/sub 3/ laminate MIM capacitors for Si RF IC applications. *IEEE Transactions on Electron Devices*, 51(6):886–894, June 2004.

[78] Shi-Jin Ding, Hang Hu, H.F. Lim, S.J. Kim, X.F. Yu, Chunxiang Zhu, M.F. Li, Byung Jin Cho, D.S.H. Chan, S.C. Rustagi, M.B. Yu, A. Chin, and Dim-Lee Kwong. High-performance MIM capacitor using ALD high-k HfO $_2$ -Al $_2$ O $_3$ laminate dielectrics. *IEEE Electron Device Letters*, 24(12):730–732, December 2003.

[79] Woojin Jeon, Hoi-Sung Chung, Daekwon Joo, and Sang-Won Kang. Tio2-al2o3-tio2 nanolaminated thin films for dram capacitor deposited by plasma-enhanced atomic layer deposition. *Electrochemical and Solid-State Letters*, 11(2):H19, 2008.

[80] Yong Shin Kim and Sun Jin Yun. Nanolaminated al2o3-tio2 thin films grown by atomic layer deposition. *Journal of Crystal Growth*, 274(3-4):585–593, February 2005.

[81] Michael Karpelson, Gu-Yeon Wei, and Robert J. Wood. Driving high voltage piezoelectric actuators in microrobotic applications. *Sensors and Actuators A: Physical*, 176:78–89, April 2012.

[82] Plantraco Ltd. www.microflight.com/Online-Catalog/Bare-Cells/FR30-bare-cell, 2014.